Graphene in Organic Electronics: Synthesis, Processing, and Applications

Dissertation

zur Erlangung des grades

“Doktor der Naturwissenschaften”

am Fachbereich Chemie, Pharmazie und Geowissenschaften

der Johannes Gutenberg-Universität Mainz

vorgelegt von

Shuping Pang

geb. in Qingdao, P. R. China

Mainz, 2011

Abstract

“Graphene in Organic Electronics: Synthesis, Processing, and Applications”

Graphene, possibly the thinnest two-dimensional material possible, is considered as a realistic candidate for the fabrication of transparent electrodes due to its unique properties, such as low resistance, high optical transmittance, good chemical and thermal stability, high mechanical strength and flexibility. In this thesis, to study the suitability of graphene electrodes in organic electronics, graphene films and patterns were firstly fabricated from GO precursors. Because the requirements of the sheet resistance, transmittance, work function and compatibility with organic semiconductor are varied in different applications, three different types of organic electronics, such as solar cell, OFETs and photodetectors have been employed to evaluate the advantages graphene electrodes compared to commercial ones.

As the transparent electrode in solar cells, the bottle-neck of thermally reduced GO films for organic solar cells is their high sheet resistance. In this regard, a two-step reduction, use of large graphene oxide sheets as precursors and introducing metal grids to form graphene/metal grid hybrid electrodes have been investigated, resulting in an efficiency of 2.5 %, which is comparable to that of ITO based solar cells.

For OFETs and photodetectors, the contact property between the electrodes and semiconductors is one of the most important parameters for organic devices. In this section, several novel fabrication methods have been developed. As a result, the graphene electrodes based OFETs shown excellent performance due to their lower contact resistance to the semiconductor layers than the gold contacts. In the polymer photodetector, the as-fabricated graphene-titanium asymmetrical electrodes also exhibited promising advantages of the improved photosensitivity, high on/off ratio and low energy consumption.

Additionally, toward the application of graphene films in flexible electronics, three film fabrication methods, including Langmuir-Blodgett assembly, lay-by-lay deposition and filtering, have also been investigated. At last, to simplify the deposition process of graphene sheets or patterns on silicon substrates, an extrinsic corrugation assisted mechanical exfoliation method has been developed to directly deposit monolayer graphene from a graphite sheet.

All of the above topics have been centered on the fabrication of highly conductive graphene films or patterns and their applications in organic electronics. The findings in this thesis would contribute to a deeper insight into the graphene based devices.

Contents

Chapter 1

1.1 Introduction

Graphene, a two-dimensional atomically thick carbon atom arranged in a honeycomb lattice, was recently isolated by repeatedly peeling highly oriented pyrolytic graphite (HOPG) using sticky tape.[1] Since then, outstanding physical properties predicted and measured for graphene have been explored for practical applications such as field-effect transistors,[1-4] chemical sensors[5-7] and composite reinforcement.[8-10] Monolayer graphene possesses high crystallographic quality and ballistic electron transport on the micrometer scale with only 2.3 % of light absorption.[11, 12] Moreover, the combination of its high chemical and thermal stability,[13, 14] high stretchability,[15-17] and low contact resistance with organic materials,[13, 18, 19] offers tremendous advantages for using graphene as a promising transparent conductor in organic electronic devices, e.g. solar cells,[14, 16, 20, 21] organic light emitting diodes (OLEDs),[22-24] liquid crystal displays (LCDs),[13] touch screens,[25] field effect transistors (FETs),[18, 19, 26] photodetectors[27, 28] and spectroelectrochemistry investigation.[29]

Transparent electrodes are an essential part of optoelectronic devices. Commercially, indium tin oxide (ITO) sets the market standard for most of these applications. In the emerging area of thin film solar cells, layers of ITO are widely used as a hole-collecting electrode with transparencies > 90 % at a wavelength of 550 nm, sheet resistances R_s of 10 – 30 Ω/□ and a favorable work function (~ 4.8 eV).[21, 30, 31] However, the use of ITO as a transparent electrode has certain limitations, such as ever increasing costs due to indium scarcity, complicated processing requirements and sensitivity to acid and basic environments, and the high surface roughness. Moreover, ITO is brittle and can easily crack when used in applications where bending is involved, such as touch screens, flexible displays and solar cells.[16] Many of the alternative transparent electrodes, therefore, have been developed in order to replace ITO, such as metal grids and metallic nanowires,[32, 33] conductive polymers like poly(3,4-ethylenedioxythiophene):poly(styrenesulfonate) (PEDOT:PSS),[34-36] and carbon nanotubes (CNTs).[37-39] Among these transparent electrode materials, CNTs films exhibit significantly high transparency across the whole visible light spectrum. One of the critical requirements for CNT films is that the density of nanotubes must be above the threshold for the formation of a percolation network. Additionally, the conductivity of individual CNTs is high, but the high resistance at the nanotube-nanotube junctions limits the conductive pathway within the films.[40-42] Thus, CNTs films are currently not competitive with ITO as transparent electrodes for practical applications.[43]

In the view of the contact behavior of the electrodes and the semiconductor layer, graphene is still an ideal electrode for orgainic electonics. The two dimentional (2D) carbon nanostructure has the excellent compatibility with the organic semiconductors, resulting in a low contact resistance.[27] Especially for the flexible organic electronics, the good compatibility is also benefitial for the long-time operation.

The experimental discovery of graphene brought a new alternative to commercially available electrodes. Although research is still at its early stages, graphene already offers several potential advantages over traditional transparent electrodes.[44-46] Many groups have already demonstrated the resilience of graphene-based organic photoelectrical devices. The excellent performance of various graphene-based electronic devices gives graphene a realistic chance of being competitive in transparent and bendable technologies.

1.2 Properties of graphene

1.2.1 Transmittance of graphene

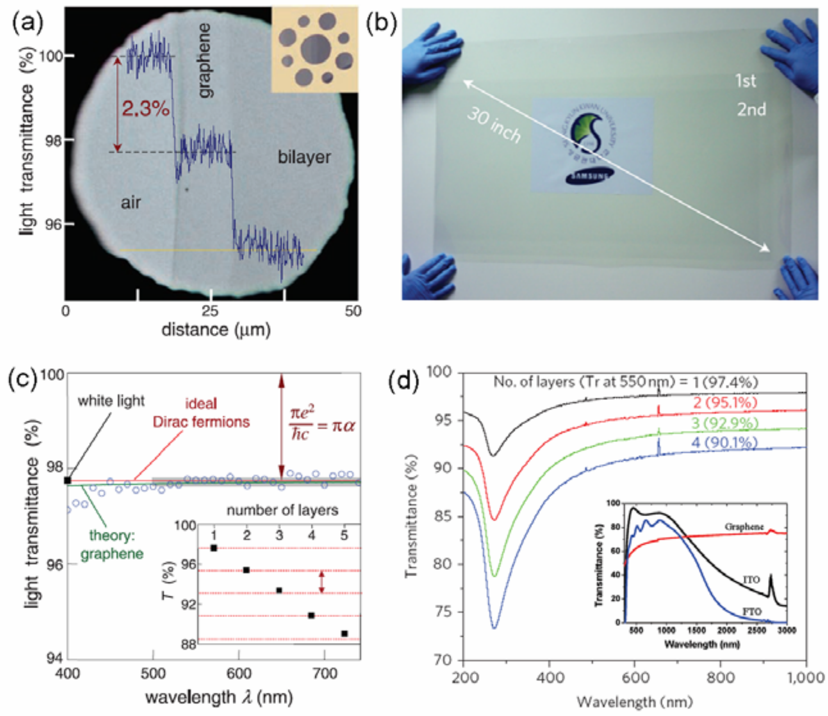

Figure 1.1 (a) Transmittance of mechanically exfoliated graphene.[11] (b) 35-inch polyethylene terephthalate (PET) sheet supported graphene film synthesized by chemical vapor deposition (CVD).[25] (c) Transmittance spectrum of mechanically exfoliated single-layer graphene. Inset in (c) Transmittance as a function of the number of graphene layers.[11] (d) Ultraviolet–visible (UV–vis) spectra of the CVD graphene films.[47] The inset in (d) is the comparison of transmittance of a 10 nm thick thermally reduced GO film, ITO and fluorine tin oxide (FTO).[14]

The theoretical transmittance (T) of a freestanding graphene can be derived by applying Fresnel equations, in the thin film limit, for a material with a fixed universal optical conductance [48] $G_0 = e^2/4\hbar \approx 6.08 \times 10^{-5}/\Omega$, to give:

$$T = (1 + 0.5\pi\alpha)^{-2} \approx 1 - \pi\alpha \approx 97.7\ \%$$

where α is the fine structure constant, $\alpha = e^2/\hbar c = 1/137$. The absorbance can be calculated as $A = 1 - T = \pi\alpha = 2.3$ %. Graphene only reflects < 0.1 % of the incident light in the visible region.[11] Thus, we can take the optical absorption of graphene layers to be linearly proportional to the number of layers, each absorbing 2.3 % over the visible spectrum (Figure 1.1a, c). In a few layer graphene (FLG) sample, each sheet can be seen as a two-dimensional electron gas, with little perturbation from the adjacent layers, making it optically equivalent to a superposition of almost non-interacting monolayer graphene (Figure 1.1d).[49] The absorption of monolayer graphene is flat over a long range,[29] as expected for 2D materials, with a peak in the UV region (~ 250 nm), attributable to inter-band electronic transition from the unoccupied π* states.[29, 50]

The optical transmittance of free standing graphene is solely determined by the value of the fine structure constant.[51] Experimentally, the transmittance of the mechanically exfoliated graphene (97.7 %) is in excellent agreement with the theoretical result as shown in Figure 1.1(a, c) for its perfect sp^2 structure. Graphene synthesized by CVD[4, 52] is of high quality and also shows the similar optical transmittance (97.4 %, Figure 1.1b, d). In both the case of the mechanically exfoliated graphene and the CVD graphene, the transmittance linearly decreases as the number of layers is increased.

1.2.2 Resistance of graphene

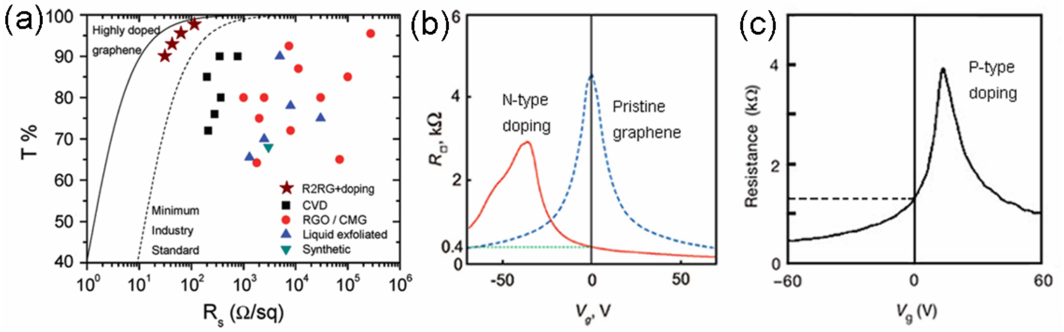

Figure 1.2 (a) Transmittance (T %) and sheet resistance (R_S) data reported in the literature.[53] (b,c) Sheet resistances of a graphene FETs as a function of gate voltage

with n-type doping[13] with polyvinyl alcohol (b) and p-type doping[4] with concentrated HNO_3 (c), respectively.

In general, R_s of graphene films fabricated by different approaches strongly depend on their surface morphology and crystal quality. One of the bottom-up methods to synthesis conductive carbon films is via the cross-linking of carbon-rich molecules on transparent substrates (e.g. quartz). This approach yields high R_s films due to its low crystal quality.[21, 54] Another approach to achieve more conductive graphene film is using liquid exfoliated graphene as the precursor, producing the graphene films with Rs ~ 5 kΩ/□ with ~ 90 % transmittance.[13] This resistance is much higher than the equivalent value calculated from the single graphene sheet due to the non-uniformity of the graphene layers and the large interlayer resistance.[13] Thermal reduction is widely used to prepare conductive graphene films from GO due to its simple solution processing and low roughness level.[14, 18, 44] Although a significant number of defects remain after thermal treatment, the resistance is still comparable to that fabricated from the liquid exfoliated graphene dispersion.[55] Nevertheless, the graphene films prepared by these methods are far below the requirement for replacing ITO (Figure 1.2a). Up to now, the most promising way to obtain large area and highly conductive graphene films is the use of CVD method.[4, 46, 52, 56, 57] The decomposition of carbonaceous sources at high temperature and subsequent growth on metallic substrates leads to high quality graphene films which are comparable to the pristine graphene exfoliated from HOPG. The recently reported growth of graphene on copper substrates by CVD with subsequent transfer onto bendable substrates enabled the production of large area graphene films (up to 30 inch) with Rs ~ 275 Ω/□ for single layer and ~ 40 Ω/□ for four-layer graphene films after p-type doping with HNO_3.[46] This is the first reported method for large-scale graphene film fabrication which surpasses the “Minimum Industry Standard” with performances superior to common transparent electrodes such as ITO and CNTs films (Figure 1.2a).

Doping has been reported to be an efficient approach to increase the overall conductivity. It has been documented that organic molecules that act as electron donors or acceptors can modify the electronic structure, which can be distinguished by FET or Raman (2D versus G frequency map) measurements.[58] Additionally, the change of the electronic structure of graphene because of the presence of organic dye molecules normally makes graphene (or GO) sheets more visible.[59] In reality, sample doping seems to be unavoidable as it could be induced either by the substrate or by adsorbed molecules from the atmosphere.[4, 13] Increasing the doping concentration reduces the R_s of graphene films.[13, 60-65] It has been shown that graphene can be chemically doped at a level of $N_i = 10^{12}$ cm^{-2} while maintaining charge carrier mobility of $\mu = 10^5$ cm^2/(V s) or higher.[66-68] Based on these values, the R_s of graphene is:

$R_s = 1/e\mu N_i N = 64.2\ \Omega/N$, where N is the number of graphene layers of the film.[24]

Simple atomic or molecular doping can directly modify the charge carrier concentration of graphene.[64, 69-71] Polyvinyl alcohol (PVA) induces n-type doping with Rs values decreasing from ~ 4 kΩ/□ to ~ 400 Ω/□ (Figure 1.2b), while the transmittance value is not affected.[13] With HNO_3 as p-type doping reagent (Figure 1.2c), [46, 72] the R_s of monolayer graphene can be decreased from 275 Ω/□ to 125 Ω/□. Four-layer doped graphene films fabricated by roll-to-roll process displayed R_s as low as 30 Ω/□.[46]

1.3 Synthesis of graphene

The first atempt to synthesize graphene can be traced back to 1975 via the thermal decomposition of carbon on single crystal Pt surface.[73] However, the process was not studied extensively due to the lack of characterization and application for such kind of graphene sheets. For a long time, physical scientists argued that a 2D lattice is instable due to the thermal fluctuation, which prevents long range crystalline order for some atomic interactions.[74] Thus, at that time there was no attempt to transfer the as-synthesized graphene film from the metal surface for in-depth investigations. It was not until 2004 that the first set of reproducible experients on graphene were reported through simple mechanical exfoliation of highly oriented pyrollitic graphite (HOPG) onto a silicon substrate.[1] Since then, many new processing routes have been proposed to synthesize graphene on a large-scale. These synthesis routes may be broadly divided into two catalogies: one is top-down and the other one is bottom-up.

The top-down routes rely on natural graphite flakes or HOPG as the precursor, being therefore cost-efficient. Graphite consists of stacked layers of many graphene sheets, held together by weak van der Waals forces. In principle, it is possible to produce graphene from a high purity graphite flake, if the weak interactions can be broken. The previously mentioned mechanical exfoliation is achieved by using a simple scotch-tape and is one of the top-down routes. Subsequentely, sonication-driven exfoliation of graphite flakes or potassium intercalated exfoliation was developed as a route to obtain large quantities of dispersed graphene.[75, 76] Another promising chemical approach to the isolation of large quantities of graphene is the oxidation and subsequent reduction of the natural graphite flakes, which is also the method of choice, because of the high yield and easy processing.[45, 77, 78]

The bottom-up approaches toward graphene production are based on using small molecular precursors, such as methane, ethanlol, acetylene and other carbon-riched molecules. Up to now, the chemical vapor deposition (CVD) method is the widest employed bottom-up technology to synthesize high quality graphene on nickel or coppler foils, followed by a transfer process through etching of the metal substrates.[16, 52, 57, 79] In the gas phase, graphene can also be prepared by substrate-free microwave plasma reactors with ethanol as the carbon source, but with lots of defects in the graphene sheets.[80] In our group, the coupling of oligophenylene precursors and followed by intramolecular cyclodehydrogenation on the gold surface at an elevated temperature has been established as avenues for the synthesis of graphene ribbon-like materials.[21, 81]

In the following sections, the liquid phase exfoliation, oxidation and reduction of nature graphite, pyrolysis of carbon-rich molecules and CVD routes aiming at the manufacture of graphene electrodes for organic electronics will be summarized.

1.3.1 Graphitic precursors to graphene

The sonication-driven exfoliation of graphite to produce graphene in organic solvents has been shown to be an efficient and low-cost method to produce oxide-free graphene in solution. A number of organic solvents have been identified to exfoliate graphite to produce graphene at quantifiable yields.[13, 82, 83] The exfoliation process occurs because of the strong interaction between the solvent and the composing layers of graphite (Figure 1.3a). The main drawback is the low yield and the high boiling temperature of the organic solvents used for exfoliation, which makes processing complicated.

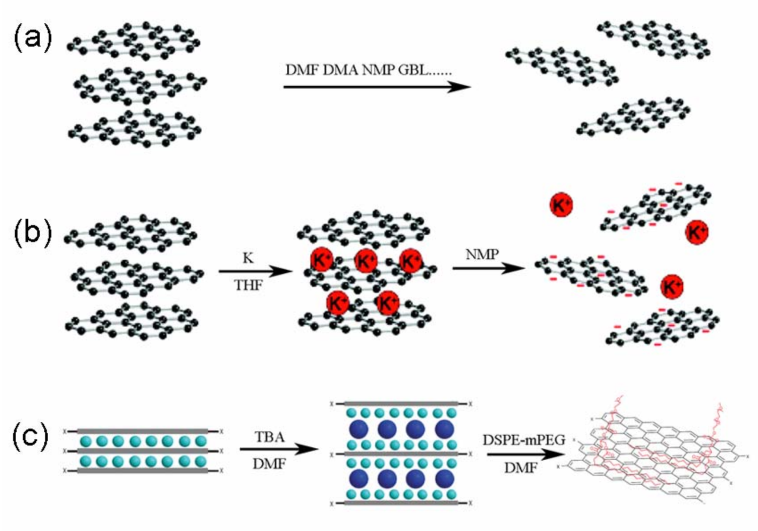

Figure 1.3 (a) Sonication- driven exfoliation of graphite flakes in organic solvents such as dimethylformamide (DMF), N,N-dimethylacetamide (DMA) and N-methylpyrrolidone (NMP). (b) Negatively charged graphene layers from graphite intercalated compound (GIC) spontaneously dissolved in NMP.[76] (c) Intercalation of

graphite with oleum (H_2SO_4) (teal spheres) and tetrabutylammonium hydroxide (TBA, blue spheres) in order and then dispersed in the DMF solution with 1,2-distearoyl-sn-glycero-3-phosphoethanolamine-N-[methoxy(polyethyleneglycol)-5000] (DSPE-mPEG) molecules as the surfactant.[84]

Another approach is to expand interlayer spacing of graphite through intercalation with highly volatile agents and then simultaneously exfoliate in organic solvents. Because of its layered structure, graphite can readily be intercalated using alkali metals.[76, 85] The GICs, such as KC8 and K(THF)xC24, are easy to exfoliate when exposed to organic solvents due to the gas evolution between the graphite layers as indicated in Figure 1.3(b). The K ions can be easily removed from the dispersion by filtration or centrifugation. However, graphene exfoliated from the GIC is not very stable due to the strong π-π stacking of the relatively large sheets produced. Long time sonication of these exfoliated sheets can make the graphene scroll to form tubular structures.[85] In order to stabilize the graphene sheets in the organic solvents, surfactants are introduced.[84, 86] For example, expanded graphite was firstly synthesized by thermally annealing the expendable graphite at high temperatures and then sonicating in dichloroethane solution with PmPV as the surfactant to produce a 0.1 mg/mL graphene dispersion. Since expanded graphite has much larger interlayer spacing compared to natural graphite, solvent molecules can easily interpenetrate within the graphitic layers during sonication. To further improve this exfoliation process, the expansion of graphite can be carried out by employing oleum as the re-intercalation agent and tetrabutylammonium hydroxide as the expanding agent. The final suspension of graphene sheets, coated with DSPE-mPEG, can be produced by sonication in DMF, with 90 % of the sheets reported as individual graphene sheets (Figure 1.3c).[84]

Two factors need to be taken into account when graphene is dispersed in organic solvents and/or surfactant solutions: polydispersity and flake size. The first one is related to the nature of the objects present in the solution, i. e. monolayers, bilayers, multilayers, which ideally would need to be separated before film formation. Because of the different buoyant densities of the multilayered graphene compared to mono or bilayer graphene, density gradient ultracentrifugation (DGU) is a valuable method to purify the graphene dispersions by removing the thick flakes. The narrower the dispersivity of the graphene dispersions, the more homogeneous the films obtained, which means significant improvement in transmittance and R_S.[87] The flake size is also an important parameter on the film formation. In general, the small sized graphene sheets are more stable than the large ones in the solution. Thus, in the view of the stability, long-time sonication is normally used to cut the large graphene sheet to small pieces.[88]

1.3.2 Graphene oxide to graphene

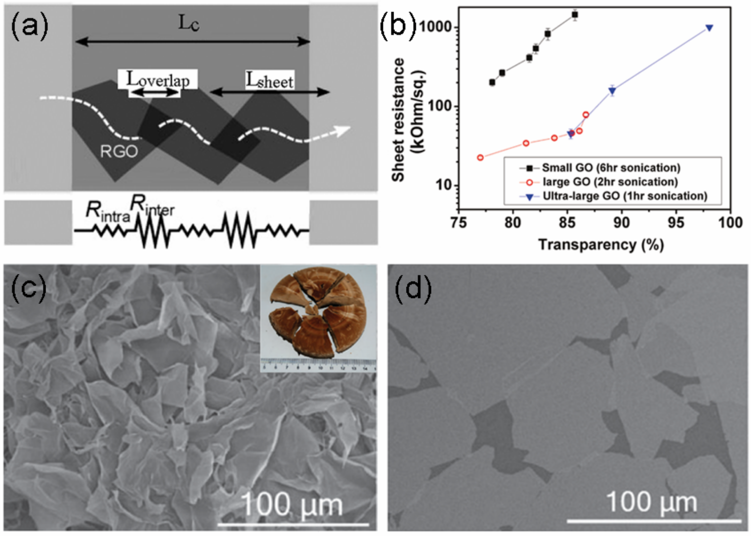

Figure 1.4 (a) Schematic of the resistance of RGO nanosheets between two electrodes and the corresponding resistor network model (bottom).[89] (b) Comparison of the sheet resistance as function of transmittance (T % at 550 nm) for the electrodes prepared from GO sheets with differently sized after 800 °C thermal reduction.[90] (c) SEM images of the freeze-dried GO solid foam (inset: digital photographs). (d) SEM images of GO sheets on a Si substrate.[91]

The low cost method of producing graphene on a large scale is to reduce graphene oxide (GO) to graphene. GO is made by oxidizing graphite with strong acids followed by intercalation and exfoliation in water.[92, 93] The downside of this approach is that, after reduction, some places in the sp^2 carbon network can be irreversibly destroyed leaving sp^3 carbons and vacancies which behave as electron traps.[3, 94, 95] However, due to its low cost and easy solution processing, a great number of attempts have been made to improve the electronic properties of the reduced graphene oxide (RGO), such as the preparation of large-sized GO sheets,[2, 90, 91, 96] chemical doping,[97] and defect repairing.[98, 99]

The in-plane conductivity in RGO film is much higher than that in the vertical direction as shown in Figure 1.4(a).[89] The preparation of ultra-large GO sheets is interesting because of the feasible processing and favorability towards reducing the inter-junction resistance (Figure 1.4a and b). The Hummers method is modified by replacing the sonication process with shaking. The ultra-large monolayer graphene sheets can be delaminated via centrifugation of the GO dispersion at different centrifugation speeds.[90, 91] Freeze-drying has proven to be a very efficient technique to dry the GO colloid, thus facilitating the re-dispersion process.[91] Due to the incorporation of a significant number of water molecules between the GO sheets, freeze-drying of the GO colloid can keep the GO sheets separated from each other, leading to a porous morphology (Figure 1.4c). The absence of post sonication treatment of the dried GO powder is undoubtedly favorable to maintain the size of the initially produced sheets (Figure 1.4d).

1.3.3 Conductive carbon film from aromatic precursors

Carbon films from organic aromatic molecules fabricated by pyrolysis at high temperatures normally show low graphitic crystallization compared with thermally reduced GO films.[21, 54, 100] The selection of the precursor, the film fabrication and the high temperature treatment are three important steps. For instance, ultrathin (~ 1 nm) conducting carbon films can be prepared through self-assembly of 1,1'-biphenyl-4-thiol (BPT) on a surface, electron beam irradiation and pyrolysis (Figure 1.5a).[54] During the thermal treatment, cross-linked aromatic monolayers undergo a transition to a mechanically stable graphitic phase (Figure 1.5b to c). The line profiles across the regions in Figure 1.5(c) give a periodicity of ~ 0.35 nm, which is close to the interplanar spacing of the close-packed planes in graphite (0.342 nm). The Rs measured after annealing at 927 °C is ~ 100 kΩ/□ (conductivity is ~ 20 S/cm, Figure 1.5d). This resistance value is much higher than that of the defect-free graphene monolayer and thermally reduced GO.[13, 54]

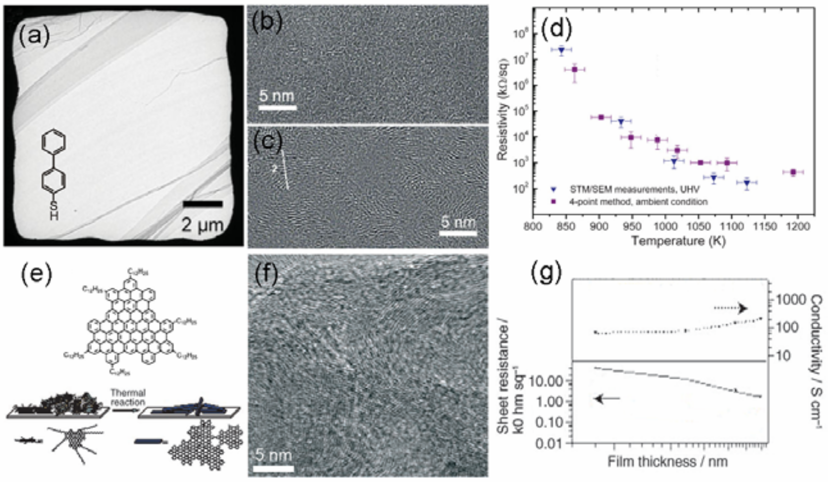

Figure 1.5 (a) Transmission electron microscopy (TEM) image of a carbon nanosheet obtained by cross-linking 1,1'-biphenyl-4-thiol (BPT, inset) and then pyrolyzing at 927 °C. (b, c) High resolution transmission electron microscopy (HRTEM) images of non-annealed (b) and annealed (c) biphenyl nanosheets (927 °C), respectively. (d) Summary of sheet resistance as a function of the annealing temperature.[54] (e) Polycyclic aromatic hydrocarbon and the mechanism of the intermolecular condensation into graphitic networks. (f) A representative HRTEM image of the scratched sample from graphene film. (g) Sheet resistance and corresponding average conductivity of the graphene film on quartz as a function of the film thickness.[21]

In order to improve the graphitic crystallization, large polycyclic aromatic hydrocarbons (PAHs) were employed as precursors for the fabrication of conductive films (Figure 1.5e). Typically, PAHs can be spin coated on a quartz substrate from organic solution and then annealed at 1100 °C, yielding a Rs of ~ 1.6 kΩ/□ (corresponding conductivity is ~ 206 S/cm) for the as-prepared 30-nm thick films. The high conductivity with respect to the pyrolyzed BPT film can be attributed to the improved graphitic crystal structure as validated in Figure 1.5(f).[21]

1.3.4 Chemical vapor deposition

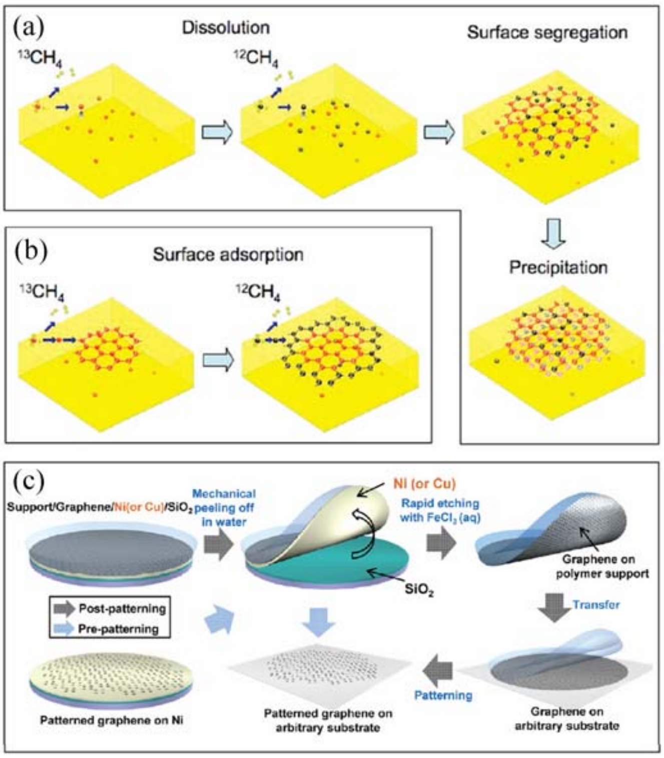

Figure 1.6 Schematic diagrams of the possible distribution of C isotopes in graphene films based on different growth mechanisms for sequential input of $^{13}CH_4$ and $^{12}CH_4$. (a) Graphene with randomly mixed isotopes might occur from surface segregation and/or precipitation. (b) Graphene with separated isotopes might occur by surface adsorption.[101] (c) Schematic illustration for the synthesis and transfer of large-area graphene or patterned graphene films on an arbitrary substrate.[102]

For graphene growth, in particular, Ni[4, 57, 103] and Cu[25, 104, 105] are mostly used as catalysts with furnace temperatures ranging from 500 to 1000 ºC. The CVD growth of graphene on Ni occurs by carbon segregation and/or precipitation processes whereas graphene on copper grows by a surface adsorption process. The film formation mechanisms have been extensively studied using carbon isotope labeling in conjunction with Raman spectroscopic mapping to track carbon during the growth process (Figure 1.6a, b).[101] The difference in the growth mechanisms of graphene on Ni and Cu foils lies in the significant difference of the solubility of carbon in these two metals. Since only a small amount of carbon can be dissolved in Cu, once the surface is fully covered with graphene the growth terminates. In contrast, Ni can dissolve more carbon atoms on its surface and hence it is difficult to achieve uniform graphene films due to precipitation of extra carbon during the cooling-down process. Therefore, metals with low C solubility such as Cu offer an advantage over Ni in the large scale growth of monolayer graphene.[101]

The application of graphene transparent electrodes in organic electronics requires an indispensable step involving the transfer of produced graphene films onto transparent substrates, like glass, quartz and PET. Transfer processes are common in the semiconductor industry. Poly(methyl methacrylate) (PMMA)[106, 107], polydimethylsiloxane (PDMS)[4, 102] and thermal release tapes (Jinsung Chemical Co. and Nitto Denko Co)[46] are mostly used to transfer graphene films onto arbitrary substrates. PMMA can be dissolved with acetone after the PMMA/graphene membrane has been placed over the target substrate. PDMS and thermally released tapes are normally employed in the dry transfer methods for the deposition of graphene on PET substrates as shown in Figure 1.6(c).[46, 102, 108]

1.4 Graphene film preparation

The transparent electrode is the one of the essential constituents of solar cells, OLEDs, LCDs and touch screens. In order to replace commercial transparent electrodes, low roughness and high conductive graphene films are required. Thus, the fabrication of high quality graphene film is a key parameter in order to bring the fundamental science to application. The film fabrication of graphene produced by the bottom-up approach (pyrolysis of the carbon-rich molecules and CVD method) is simple and has been thoroughly discussed in the above synthetic section. The following part will summarize the preparation of the graphene films from the top-down routes, e.g. graphene oxide dispersion. It is proposed that the graphene films fabricated from natural graphite flakes are specially promising due to their cost-efficiency.

1.4.1 Graphene film from graphene dispersion

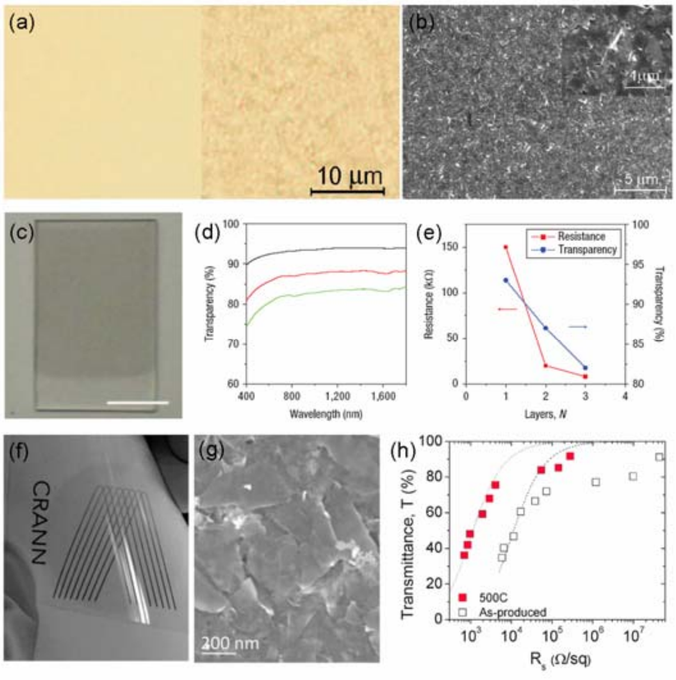

Figure 1.7 (a) Light transmittance through an original glass slide, the right side covered with graphene film. (b) Scanning electron micrograph (SEM) of a thin graphene film obtained by spray-coating from a liquid phase exfoliated graphene dispersion.[13] (c) Photograph of a two-layer graphene film fabricated by the Langmuir-Blodgett (LB) technique from the surfactant stabilized graphene dispersion (scale bar is 10 mm). (d) Transmittances of one-, two-, and three-layer graphene films.

(e) Resistance and transparencies of one-, two- and three-layer LB graphene films.[84] (f) Photograph of 6 nm thick graphene film on PET substrate prepared by filtration and transfer process from the surfactant stabilized graphene water dispersion. (g) SEM image of the surface of graphene film. (h) Transmittance plotted as a function of R_s for both as-produced and annealed films.[55]

Due to the nature of the liquid phase exfoliated graphene dispersions, spray coating, LB and vacuum filtration are suitable methods of fabricating thin graphene films. Spray-coated films from pure graphene dispersion in DMF display transparencies of ~ 90 % and R_s ~ 5 kΩ/□ (Figure 1.7a, b).[13] For surfactant stabilized graphene dispersions, both LB and vacuum filtration techniques can be used.[55, 84] Small graphene sheets stabilized by a surfactant such as DSPE-mPEG can assemble to form a monolayer graphene film at the water/air interface.[84] Therefore, the fabrication of one-, two- or three layer graphene films can be deposited by repeating the LB cycles (Figure 1.7c). The decoration of the surface of graphene with DSPE-mPEG is very important for its stabilization on the water surface with minimal aggregation during film formation. The accurate control of the film thickness makes LB a promising approach for the fabrication of low-cost, large-scale graphene films (Figure 1.7d,e). The higher resistance of these films compared to spray-coated films could be attributed to the small size of the graphene sheets and the presence of surfactant molecules between the graphene layers.[84] Vacuum filtration, which allows effective removal of most of the excess surfactant molecules on the filtrated film, has been widely employed to produce homogenous CNTs films from the surfactant stabilized CNT dispersions.[87] The process allows reasonably good nanoscale control over the thin film thickness by simply varying either the concentration or the filtrated volume of graphene dispersion.[45, 55] Homogenous films can be obtained by vacuum filtration on porous cellulose filter membranes and subsequent transfer onto glass/or PET substrates (Figure 1.7f, g). In this way, the fabricated graphene films display R_s ~ 4 kΩ/□ and ~ 80 % transmittance after 500 ºC thermal annealing (Figure 1.7h).[55] However, the resistance of graphene films prepared by solution-exfoliated graphene is still quite high because of the large contact-resistance between the adjacent graphene sheets and the presence of adsorbed solvent molecules and surfactants.[13, 75]

1.4.2 Graphene film from GO sheets

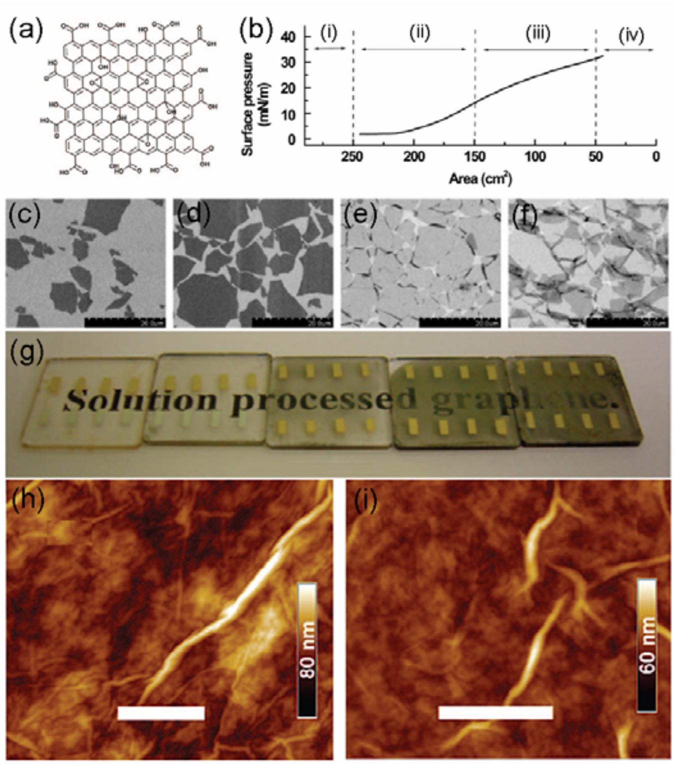

Figure 1.8 (a) Structural model of a GO showing carboxylic acid groups at the edge and epoxy and hydroxy groups mainly on the basal plane. (b) Isothermal surface pressure/area plot showing the corresponding regions i-iv at which the monolayers were collected. (c-f) SEM images showing the collected GO monolayers on a silicon wafer at different regions of the isotherm. The packing density can be continuously tuned. Scale bars in (c)-(f) represent 20 µm.[109] (g) Photograph of an unreduced (leftmost) and a series of high-temperature reduced GO films prepared by spin coating with increasing thickness. (h) and (i) are AFM images of GO film before and after 1100 °C thermal reduction. White bar in g and h is 1 µm.[44]

Individual sheets of GO can be viewed as graphene decorated with oxygen-containing groups on both sides of the plane and around the edges. The negatively charged sheets allow the formation of stable colloidal suspensions by electrostatic interactions in water.[45] GO films can be easily fabricated by spray-coating,[110] dip-coating,[14] spin-coating,[44] vacuum filtering[45] and LB[109] techniques.

Similar to graphene dispersions exfoliated by solution sonication, thin GO films can also be prepared by vacuum filtration and LB techniques.[45, 109, 111] The oxygen-containing groups partially decorate the large hexagonal carbon network and as a consequence it features the GO sheets with hydrophobic and hydrophilic components (Figure 1.8a).[112, 113] Therefore, the negatively charged sheets form a stable dispersion against flocculation or coagulation when they are confined at the 2D air-water interface.[109, 112, 114] The edge-to-edge repulsion between the single layers prevents them from overlapping.And the LB method enables the deposition of GO films on any arbitrary substrate and the size of the film is only limited by the size of the LB vessel. A gradual increase in surface pressure is recorded when the barrier is closed, as shown in the isothermal surface pressure-area plot in Figure 1.8(b). The corresponding LB- assembled GO films with different densities can be obtained by dipping the film at different surface pressures (Figure 1.8c-f). It is noteworthy that there are no wrinkled structures in the first layer GO sheets due to the hydrophilic nature of the silicon substrate. In theory, thick GO films can be obtained by sequential dip-coating, but the newly deposited top layers tend to be wrinkled.[109] For the application as the transparent electrodes in solar cells, about ten layers of graphene are needed to provide the low resistance and high transmittance. In this case, spin-coating is more convenient as the thickness of the graphene films can be easily adjusted by the spin-coating speed and/or the concentration of the GO dispersion.[18] The conventional concentration of GO in water is lower than 0.5 mg/mL, and it is generally difficult to achieve a concentrated GO dispersion without the sonication process. As mentioned above, the sonication treatment is prone to cut the large graphene sheets into small pieces. However, this process is detrimental to the electronic conductivity of graphene after reduction.[18] Ultracentrifugation can yield a desired concentration from a diluted GO dispersion. A 10000 rpm centrifuging speed can yield up to ~ 8 mg/mL of GO dispersion, which is high enough to prepare a ~ 100 nm thick GO film. Figure 1.8(g) displays a series of GO films deposited on quartz substrates, where the leftmost sample is GO and the rest are high-temperature treated GO films with thickness increasing from left to right. Large GO sheets are beneficial for decreasing the resistance but are unfavorable for fabricating large area homogenous films, which are always associated with wrinkled structures as indicated in the atomic force microscope (AFM) images (Figure 1.8h and 1.8i).[44]

The oxygen content in insulating GO is as high as ~ 40 wt% which badly destroys the sp^2 structure.[115] In order to restore the conductivity, the sp^2 structure must be extensively repaired. Although a number of methods have been established to eliminate the oxygen-containing moieties and recover the electronic properties. Thermal reduction (or combined with pre-chemical reduction with N_2H_4) is currently the most efficient approach to achieve highly conductive RGO films.[45] Chemical reduction via N_2H_4 alone provides a conductivity of < *50* S/cm which is significantly lower than that of thermally reduced GO films (~ 1000 S/cm).[44, 45, 116] The most conductive graphene film, from GO, (~ 1800 S/cm) was reported by vacuum annealing at 1100 ºC for three hours. The film shows the Rs of ~ 800 Ω/□ and transmittance of 82 % at 550 nm.[24] Based on the thermally reduced GO film, repairing the defects is more efficient to further improve the conductivity and the mobility.[98, 117]

1.5 Graphene patterns

In addition to extended graphene films with high transparency, another important aspect in organic electronics is to use graphene with patterned structures. For instance, patterned graphene electrodes can be used in OFETs and photodetector devices, in which the organic active layer is in direct contact with the graphene electrodes. Therefore, the contact property of the graphene electrode and the semiconductor material is essential for the relevant applications.

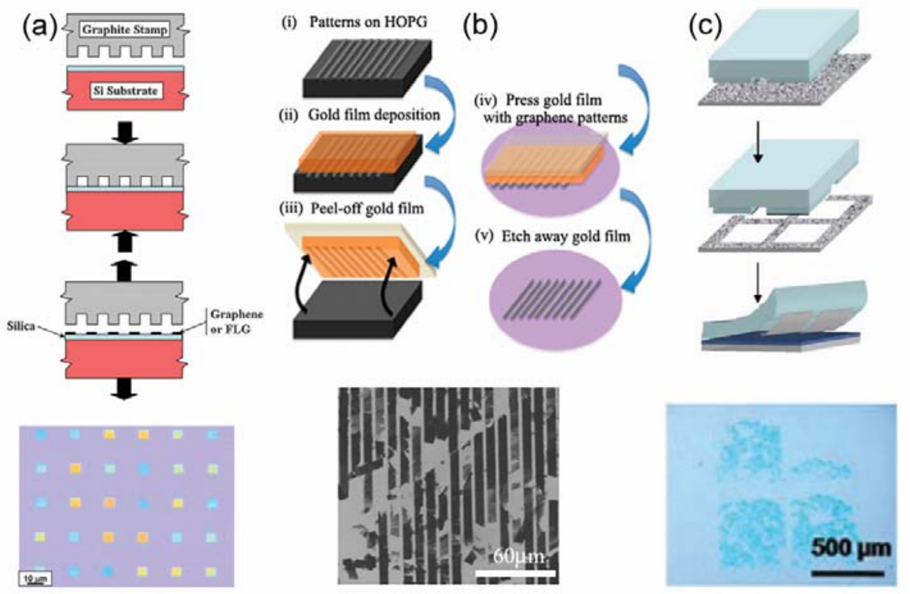

Figure 1.9 (a) Schematic illustration of the stamping process (above) and the optical microscopy image of the stamped graphite squares (below).[118] (b) Schematic diagram depicting transfer-printed graphene patterns by gold-film-assisted exfoliation (above). The SEM image of transferred graphene strips is also shown (below). The process includes (i) fabrication of the graphene patterns on HOPG by photolithography and O_2 plasma etching, (ii) depositing a gold film on the patterns, (iii) peeling off the gold film (iv) transfer-printing graphene patterns onto a substrate, and (v) etching away the gold film.[119] (c) Diagram of the PDMS transfer process (above) and the optical microscopy image of the transferred graphene patterns (below). The process begins by depositing graphene materials on a glass substrate and carefully "inking" the pre-patterned PDMS stamp. Subsequently, the pattern is transferred on a pre-heated Si/SiO_2 substrate.[120]

One of the simplest methods to pattern graphene or graphite on silicon substrates is to use a pre-patterned HOPG stamp as shown in Figure 1.9(a).[118] To transfer the pattern on the silicon substrate, high pressure is required on the HOPG stamp. This results in large-area transfer of complex patterns of graphene or few layer graphene after lifting-off the stamp. Although this method allows site-specific patterning, the thickness of the transferred graphene material varies, from several nanometers to tens of nanometers. The subsequent development in controlling the thickness of the transferred graphene patterns is achieved through the use of a gold film as the transfer stamp as illustrated in Figure 1.9(b).[119] Firstly, a thick graphite layer is peeled off from a pre-patterned HOPG substrate. Because of the strong adhesion between graphene and gold, a reverse exfoliation is used to exfoliate the mutilayer graphite to monolayer graphene. After transferring on the desired substrate followed by ething away the gold film, graphene strips with a thickness of several nanometers can be obtained.

For graphene oxide and the chemically converted graphene dispersion, soft transfer using PDMS as the stamp is also studied (Figure 1.9c).[120] As the binding energy between PDMS and graphene is weaker than that between silicon substrate and graphene, graphene is readily transferred from the PDMS to Si/SiO_2 substrates. The stamp is finally peeled from the substrate, leaving behind graphene patterns. The disadvantage of this stamping method is the high roughness of the edges of the graphene patterns due to the large size of the graphene sheets.

1.6 Applications in organic electronics

There are a vast number of studies in organic devices using graphene as the main electrode material. In general, the applications can be summarized within two categories: The first group is the use of graphene films for the devices in sandwich structures, such as solar cells, OLEDs, LCDs and touch screens. The second one is applying graphene patterns for the electronics in plannar structure, such as OFETs and photodetectors. The following section will mainly show solar cells, OFETs and photodetectoes as prototypical examples to present the state of art of graphene electrode properties.

1.6.1 Solar cells

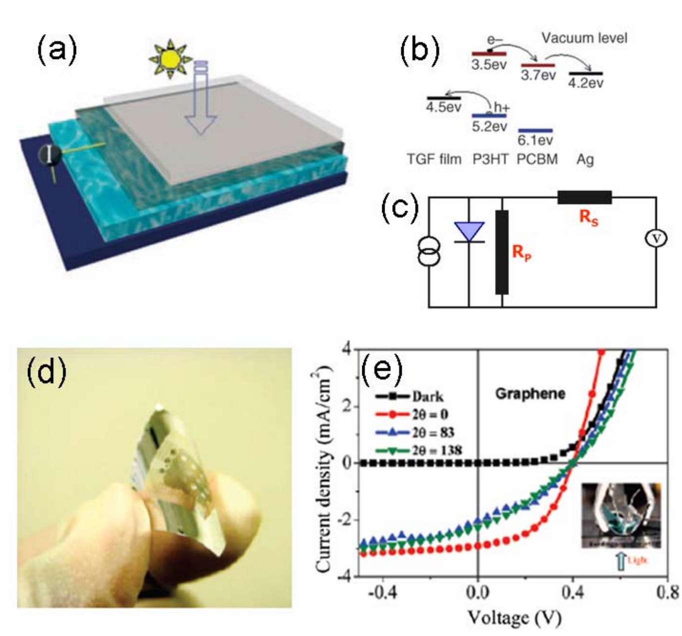

Figure 1.10 (a) Illustration of a solar cell configuration; the four layers from bottom to top are cathode (Ag or Al), P3HT/PCBM, graphene, and quartz substrate, respectively. (b) A schematic representation of charge transfer and transport as an energy level diagram.[21] (c) Equivalent circuit for standard solar cell under illumination. (d) Photograph of flexible of CVD graphene on a PET substrate. (f) I–V characteristics of CVD graphene photovoltaic cells with different bending angles. Insets show the experimental setup to bend the flexible solar cells. (e) Fill factor (FF) dependence of the bending angles for CVD graphene and ITO devices.[16]

To demonstrate how transparent graphene films performed as electrodes in organic solar cells, the simplest bulk-heterojunction solar cells consisting of graphene/(poly[3-hexylthiophene]:[6,6]-phenyl C61 butyric acid methyl ester) (P3HT:PCBM)/Ag without any buffer layers were studied (Figure 1.10a).[14] The favorable work function of graphene makes it suitable as the hole- collecting electrode (Figure 1.10b), yielding an overall power efficiency of 0.29 %. Comparing the fill factor (FF) and the short circuit current (Isc) with those of the ITO based solar cells leads to the conclusion that the low efficiency of the graphene based device is due to the high Rs of the graphene electrode fabricated from PAHs via the thermally-mediated cross-linking process (~ 18 kΩ/□ and a transmittance of 85 %).[14]

In general, there are two approaches to improve the efficiency of graphene-based organic solar cells. One is to decrease the resistance of the graphene electrodes, and the other is to introduce buffer layers (hole- and electron- transporting layers) to increase the shunt resistance of the solar cell (Figure 1.10c).[121-124] The parallel resistance (sometimes referred to as shunt resistance, Rsh) Rp arises from the current leakage through the cell (e.g. recombination of the charge carriers), and the series resistance (R_S) arises from the resistance of the cell materials to the current flow (e.g. resistance of the electrodes). Normally, the series resistance R_s is at least one order of magnitude lower than Rp.[123] Thus, both reducing Rs and increasing Rp enhance the efficiency of the solar cells.[124] It was recently demonstrated that, the more conductive CVD graphene film with a R_s of 230 Ω/□ and a transparency of 72 % (550 nm) showed performance comparable with the ITO- based device.[16] Additionally, CVD graphene based solar cells revealed an outstanding ability to operate under bending conditions of up to 138°, whereas the ITO-based devices displayed cracks and irreversible failure under bending of 60°. This indicates the great potential of graphene films for flexible photovoltaic applications.[16]

Besides serving as transparent electrodes, there are still other applications of graphene in organic heterojunction solar cells. For instance, functionalized graphene can be used as an electron acceptor to replace PCBM in organic heterojunction solar cells with poly(3-hexylthiophene) and poly(3-octylthiophene) as donors, producing a power efficiency of 1.1 % and 1.4 %, respectively. [125, 126] Moreover, a thin reduced GO layer (2 nm) can be applied to replace PEDOT:PSS as hole transport and electron blocking layer in the organic heterojunction solar cells.[127]

1.6.2 Organic field effect transistors and photodetectors

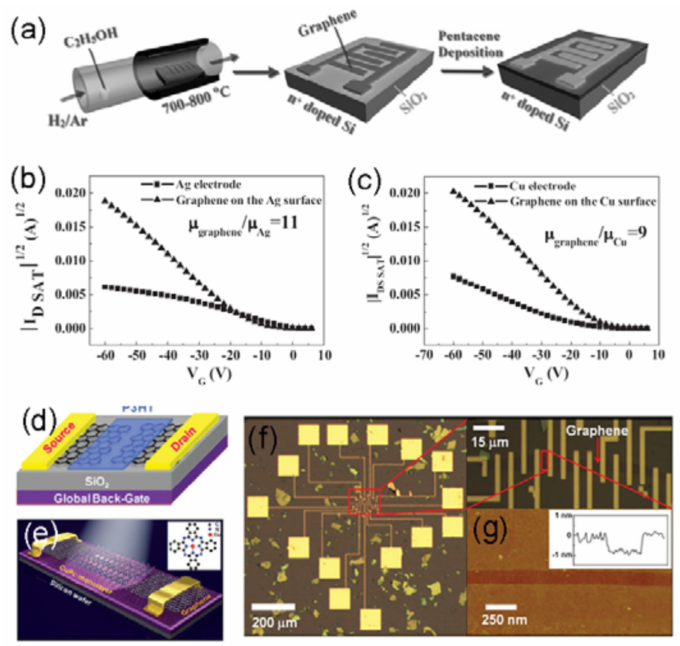

Figure 1.11 (a) Schematic illustration of the fabrication of graphene modified Ag or Cu patterned electrodes. (b) Transfer characteristics of pentacene FETs with Ag/graphene and Ag electrodes. (c) Transfer characteristics of pentacene FETs with Cu/graphene and Cu electrodes.[19] (d, e) A schematic of how monolayer graphene sheets function as 2D electrodes to measure the electrical properties of organic semiconductors. (f, g) OM and AFM image of a representative device. The gap size between the graphene ends is ~100 nm. Inset is the height profile across the nanogap.[28]

For p-type organic semiconductors, gold is normally used as the source and drain (S/D) electrodes due to its favorable work function. Recently, it was reported that the work functions of Cu and Ag electrodes can be tuned by depositing thin graphene films on their surface. The modification of the electrodes can be easily carried out via heating the patterned Cu and Ag electrodes in an ethanol/H_2/Ar gas at 700–800 ºC (Figure 1.11a).[19] The mobilities of pentacene FETs with the Cu (or

Ag)/graphene as the S/D electrodes were reported to be 10 times higher than that with pure Cu or Ag contacts (Figure 1.11b, c). The reason for this improved performance could be attributed to the decreased work function of the S/D electrodes and the reduced contact resistance between the electrodes and the organic semiconductors after deposition of a thin layer of graphene.[19] Furthermore, monolayer graphene can also act as the S/D electrodes in transparent OFETs.[13, 26] For instance, monolayer graphene electrodes can be directly prepared by the oxidative cutting of an individual 2D planar graphene sheet involving electron beam lithography and oxygen plasma etching (Figure 1.11d-g). The mobility of the P3HT transistor is around 0.0014 cm^2/Vs.[28] For the graphene based CuPc FETs, the output currents are about three orders of magnitude greater than that for similar gold-contacted devices, thus proving that OFETs based on graphene electrodes exhibited reduced injection barriers and overall better effective mobilities.[27]

Another application of patterned graphene electrode is as electrode material in the organic photodetectors. The photosensitivity of P3HT (Figure 1.11d) and copper phthalocyanine (CuPc, Figure 1.11e) photodetectors based on planar single-layer graphene contacts has been investigated.[27] It is generally considered that graphene sheets form a smooth interface for contacting molecules and may exhibit barrier-free-like injection, favorable for charge transport from the semiconductor to the electrodes. In spite of this, both P3HT and CuPc -based photodetectors show no significant improvement when using graphene to replace the traditional electrode. Particularly, the response time is low and the on/off ratios are less than 2 possibly due to the low dissociation efficiency of the excitons into free electrons and holes.[27, 28, 128-131] Therefore, more attention should be given to this field toward high sensitive photodetectors.

1.7 Motivation

As we discussed above, graphene is mechanically stable, optically transparent, chemically inert, and an excellent electrical and thermal conductor. These intriguing properties make graphene a promising candidate for applications in various orgainic electronics. Novel graphene-based transparent electrodes on flexible substrates for organic electronics show excellent operational flexibility, which is not accessible with current transparent ITO electrodes. The industry requirements of sheet resistance and electrode transparency strongly depend on the application purpose, which means that graphenes with different values of resistances/transmittances can be employed in different kinds of electronic devices. Among graphene electrodes based organic electronic devices, organic solar cells require highly conductive electrodes in order to efficiently transport carriers with low energy loss. For this purpose, the bottleneck of graphene films is the low conductivity. Therefore, based on GO precursors, much attention should be directed to the improvement of conductivity of RGO films. In regard to the application of graphene in OFETs and photodetectors, the requirement of the conductivity is low and the current conductivity of RGO is high enough. The final performance of the patterned graphene electrodes based devices is mainly affected by the contact resistance between the graphene electrodes and the semiconductor layers. Therefore, in this thesis, we will focus on the following directions to address the utilization of graphene electrodes in organic solar cells, OFETs and organic photodetectors.

a). In general, the requirement of sheet resistance and transmittance of transparent electrodes for the solar cells is much higher than that for OLEDs and LCDs. Traditionally, transparent ITO electrode is widely used, featuring a conductivity of ~ 3000 S/cm. The sheet resistance of a 130 nm thick ITO film is 15 Ohm/square, with a transmittance of 80 %. However, the conductivity of the RGO film is ranging from several to several hundreds S/cm depending on the quality of the GO precursor, the reduction condition and the film uniformity. Additionally, the absorption of one layer pristine graphene is 2.3 %, which means the graphene film should be less than 9 layers to give a transmittance of 80 %. We can not prepare the RGO film as thick as the commercial ITO electrode (130 nm). Therefore, as the fist step, we will improve the conductivity of RGO films by optimizing the GO precursors and the film reduction process. As a result, RGO films with a conductivity of 1300 S/cm were obtained.

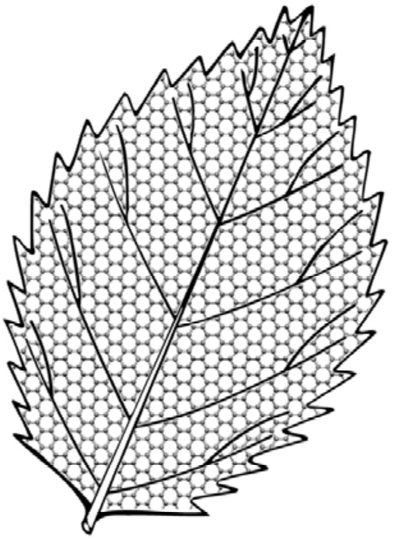

Figure 1.12 The concept of the graphene-metal wire hybrid electrodes

Neverthelss, such conductivity is still far below that of commercial ITO electrodes. It is the fact that decreasing the transport distance of carriers in the RGO film can also be an efficient strategy to reduce the energy loss when it is used as the transparent electrode in solar cells. Therefore, we propose the fabrication of graphene/metal grid hybrid electrodes. In this strategy, the graphene film can only serve as the short-range conductor and the metal grid acts as the long-range conductor, which is proposed to be a more efficient in collecting and transporting the carriers to the external circuits (Figure 1.12). As a result, the sheet resistance of this hybrid film is below 200 Ohm/square while keeping the transmittance higher than 80 %. The P3HT/PCBM heterojunction solar cells based on such hybrid electrodes provide a power conversion efficiency up to 2.5 %, which is comparable to that fabricated with commercial ITO electrodes.

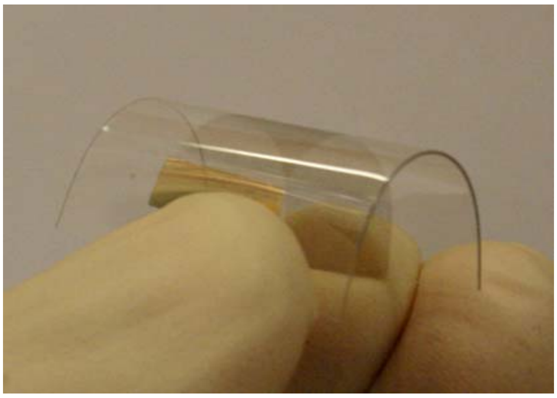

Figure 1.13 flexible graphene/metal grid hybrid electrodes.

Following the above concept, we will attempt to fabricate flexible graphene/metal grid hybrid electrodes, which can be very promisng for low cost flexible organic solar cells or other organic electronics. Towards this end, the first challenge is to fabricate homogenous high-conductive graphene films on flexible subatrates. In this part, we will apply high-quality electrochemically exfoliated graphene precursors to replace GO in view of the low temperature processing requirement. Based on such graphene dispersions, highly conductive and flexible graphene/metal grid hybrid electrodes have been successfully produced via filtering/transfer graphene films directly on a pre-patterned PET substrate (Figure 1.13).

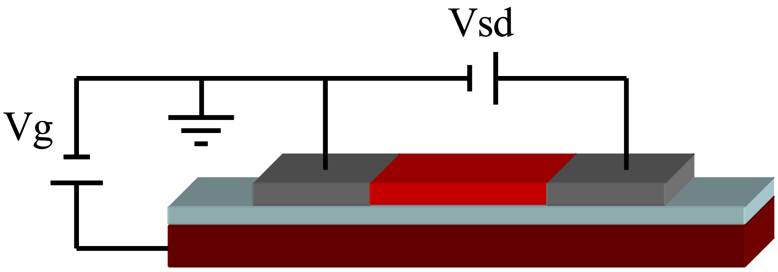

Figure 1.14 OFETs with graphene as the source and drain electrodes

b). It has been reported that carbon nanotubes as the source and drain electrodes in OFETs are superior to traditional metal contacts due to the low contact resistance between carbon nanotubes and organic materials. We conceive that the same feature should also be hold in the graphene electrode based OFETs (Figure 1.14). More importantly, the two-dimential structure of graphene can make graphene electrodes more interesting than carbon nanotubes for the electrode material due to the thin film with smooth surface. Motivated by this concept, graphene based source and drain electrodes will be patterned on Si/SiO_2 and PET substrates for subsequent device fabrication and characterization. As a result, the mobility of p-type P3HT based on graphene contacts is once higher than that with gold electrodes, while the threshold voltages in both the p-type pentacene and n-type N,N’-dioctyl-1,7-dibromo-perylene diimide ($C_{40}H_{40}Br_2N_2O_4$) semiconductors are extremely reduced with respect to the gold contacts.

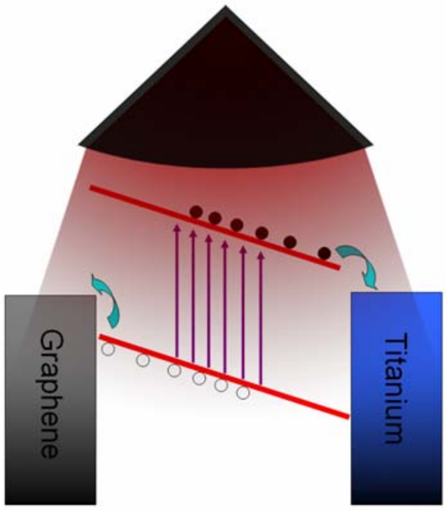

Figure 1.15 The concept of the graphene-titanium asymmetrical electrodes

c). It has been proved in the above OFETs study that graphene electrode possesses a high carrier injection efficiency in P3HT layer in comparison with the gold electrode. Therefore, graphene should also be an interesting electrode material in organic photodetectors. Traditionally, there are two different types of polymer photodetectors, namely photoconductors and photodiodes. In order to avoid the weakness of each type of photodetectors and fulfill the requirements of easy processing, low light consumption and high photosensitivity, coplanar asymmetrical electrodes will be designed and fabricated with graphene as the hole injecting electrode and titanium as the electron injecting electrode. As a result, a 'build-in' potential is generated between the two different electrodes, which can fastly dissociate the excitions to holes and electrons and then repell them to the opposite electrodes (Figure 1.15). The on/off ratio of the P3HT photodetector based on the as-prepared graphene-titanium electrodes is several hundred times higher than the P3HT device constructed on symmetrical gold electrodes.

Figure 1.16 The concept of directly stampling graphene patterns from HOPG stamp on silicon substrate.

d). The above graphene patterns are based on the reduction of solution processed GO films. The fabrication process typically involves several steps, such as spin-coating the GO film, thermal reduction, evaporating of a sacrificial aluminum layer, oxygen plasma etching and removal of aluminum layer. Therefore, a simplified strategy to derectly deposite graphene patterns on the silicon substrate should be more interesting for the future graphene based electronic devices. In this work, we will present a facial method to directly transfer the graphene layers on silicon substrates from a patterned HOPG stamp with an assistance of heating treatment (Figure 1.16). This transfer strategy is environment friendly and is feasible for the large scale fabrication of graphene patterns on silicon substrates, which will be promising for the construction of integrated circuit.

References

[1] K. S. Novoselov, A. K. Geim, S. V. Morozov, D. Jiang, Y. Zhang, S. V. Dubonos, I. V. Grigorieva, A. A. Firsov, *Science* **2004**, *306*, 666.

[2] V. C. Tung, M. J. Allen, Y. Yang, R. B. Kaner, *Nat. Nanotechnol.* **2009**, *4*, 25.

[3] C. Gomez-Navarro, R. T. Weitz, A. M. Bittner, M. Scolari, A. Mews, M. Burghard, K. Kern, *Nano Lett.* **2007**, *7*, 3499.

[4] K. S. Kim, Y. Zhao, H. Jang, S. Y. Lee, J. M. Kim, K. S. Kim, J. H. Ahn, P. Kim, J. Y. Choi, B. H. Hong, *Nature* **2009**, *457*, 706.

[5] T. O. Wehling, K. S. Novoselov, S. V. Morozov, E. E. Vdovin, M. I. Katsnelson, A. K. Geim, A. I. Lichtenstein, *Nano Lett.* **2008**, *8*, 173.

[6] P. K. Ang, W. Chen, A. T. S. Wee, K. P. Loh, *J. Am. Chem. Soc.* **2008**, *130*, 14392.

[7] R. Bogue, *Sensor Review* **2008**, *28*, 344.

[8] S. Stankovich, D. A. Dikin, G. H. B. Dommett, K. M. Kohlhaas, E. J. Zimney, E. A. Stach, R. D. Piner, S. T. Nguyen, R. S. Ruoff, *Nature* **2006**, *442*, 282.

[9] Y. X. Xu, W. J. Hong, H. Bai, C. Li, G. Q. Shi, *Carbon* **2009**, *47*, 3538.

[10] A. K. Geim, *Science* **2009**, *324*, 1530.

[11] R. R. Nair, P. Blake, A. N. Grigorenko, K. S. Novoselov, T. J. Booth, T. Stauber, N. M. R. Peres, A. K. Geim, *Science* **2008**, *320*, 1308.

[12] A. W. W. Ludwig, M. P. A. Fisher, R. Shankar, G. Grinstein, *Phys. Rev. B* **1994**, *50*, 7526.

[13] P. Blake, P. D. Brimicombe, R. R. Nair, T. J. Booth, D. Jiang, F. Schedin, L. A. Ponomarenko, S. V. Morozov, H. F. Gleeson, E. W. Hill, A. K. Geim, K. S. Novoselov, *Nano Lett.* **2008**, *8*, 1704.

[14] X. Wang, L. J. Zhi, K. Mullen, *Nano Lett.* **2008**, *8*, 323.

[15] D. I. Son, T. W. Kim, J. H. Shim, J. H. Jung, D. U. Lee, J. M. Lee, W. Il Park, W. K. Choi, *Nano Lett.* **2010**, *10*, 2441.

[16] L. G. De Arco, Y. Zhang, C. W. Schlenker, K. Ryu, M. E. Thompson, C. W. Zhou, *ACS Nano* **2010**, *4*, 2865.

[17] F. Gunes, G. H. Han, K. K. Kim, E. S. Kim, S. J. Chae, M. H. Park, H. K. Jeong, S. C. Lim, Y. H. Lee, *Nano* **2009**, *4*, 83.

[18] S. P. Pang, H. N. Tsao, X. L. Feng, K. Mullen, *Adv. Mater.* **2009**, *21*, 3488.

[19] C. A. Di, D. C. Wei, G. Yu, Y. Q. Liu, Y. L. Guo, D. B. Zhu, *Adv. Mater.* **2008**, *20*, 3289.

[20] Q. Su, S. P. Pang, V. Alijani, C. Li, X. L. Feng, K. Mullen, *Adv. Mater.* **2009**, *21*, 3191.

[21] X. Wang, L. J. Zhi, N. Tsao, Z. Tomovic, J. L. Li, K. Mullen, *Angew. Chem. Int. Ed.* **2008**, *47*, 2990.

[22] P. Matyba, H. Yamaguchi, G. Eda, M. Chhowalla, L. Edman, N. D. Robinson, *ACS Nano* **2010**, *4*, 637.

[23] G. Jo, M. Choe, C. Y. Cho, J. H. Kim, W. Park, S. Lee, W. K. Hong, T. W. Kim, S. J. Park, B. H. Hong, Y. H. Kahng, T. Lee, *Nanotechnology* **2010**, *21*.

[24] J. B. Wu, M. Agrawal, H. A. Becerril, Z. N. Bao, Z. F. Liu, Y. S. Chen, P. Peumans, *ACS Nano* **2010**, *4*, 43.

[25] S. Bae, H. Kim, Y. Lee, X. F. Xu, J. S. Park, Y. Zheng, J. Balakrishnan, T. Lei, H. R. Kim, Y. I. Song, Y. J. Kim, K. S. Kim, B. Ozyilmaz, J. H. Ahn, B. H. Hong, S. Iijima, *Nat. Nanotechnol.* **2010**, *5*, 574.

[26] W. Liu, B. L. Jackson, J. Zhu, C. Q. Miao, C. H. Chung, Y. J. Park, K. Sun, J. Woo, Y. H. Xie, *ACS Nano* **2010**, *4*, 3927.

[27] Y. Cao, Z. M. Wei, S. Liu, L. Gan, X. F. Guo, W. Xu, M. L. Steigerwald, Z. F. Liu, D. B. Zhu, *Angew. Chem. Int. Ed.* **2010**, *49*, 6319.

[28] Y. Cao, S. Liu, Q. Shen, K. Yan, P. J. Li, J. Xu, D. P. Yu, M. L. Steigerwald, C. Nuckolls, Z. F. Liu, X. F. Guo, *Adv. Funct. Mater.* **2009**, *19*, 2743.

[29] C. M. Weber, D. M. Eisele, J. P. Rabe, Y. Liang, X. Feng, L. Zhi, K. Muellen, J. L. Lyon, R. Williams, D. A. V. Bout, K. J. Stevenson, *Small* **2010**, *6*, 184.

[30] J. K. Wassei, R. B. Kaner, *Mater. Today* **2010**, *13*, 52.

[31] J. Y. Kim, K. Lee, N. E. Coates, D. Moses, T. Q. Nguyen, M. Dante, A. J. Heeger,

Science **2007**, *317*, 222.

[32] J. Y. Lee, S. T. Connor, Y. Cui, P. Peumans, *Nano Lett.* **2008**, *8*, 689.

[33] S. De, T. M. Higgins, P. E. Lyons, E. M. Doherty, P. N. Nirmalraj, W. J. Blau, J. J. Boland, J. N. Coleman, *ACS Nano* **2009**, *3*, 1767.

[34] C. Y. Zhang, X. J. Zhang, X. H. Zhang, X. Fan, J. S. Jie, J. C. Chang, C. S. Lee, W. J. Zhang, S. T. Lee, *Adv. Mater.* **2008**, *20*, 1716.

[35] S. I. Na, S. S. Kim, J. Jo, D. Y. Kim, *Adv. Mater.* **2008**, *20*, 4061.

[36] J. Ouyang, Q. F. Xu, C. W. Chu, Y. Yang, G. Li, J. Shinar, *Polymer* **2004**, *45*, 8443.

[37] Z. C. Wu, Z. H. Chen, X. Du, J. M. Logan, J. Sippel, M. Nikolou, K. Kamaras, J. R. Reynolds, D. B. Tanner, A. F. Hebard, A. G. Rinzler, *Science* **2004**, *305*, 1273.

[38] M. W. Rowell, M. A. Topinka, M. D. McGehee, H. J. Prall, G. Dennler, N. S. Sariciftci, L. B. Hu, G. Gruner, *Appl. Phys. Lett.* **2006**, *88*, 233506.

[39] T. M. Barnes, J. D. Bergeson, R. C. Tenent, B. A. Larsen, G. Teeter, K. M. Jones, J. L. Blackburn, J. van de Lagemaat, *Appl. Phys. Lett.* **2010**, *96*, 243309.

[40] P. W. Chiu, G. T. Kim, G. Gu, G. Philipp, S. Roth, *AIP Conf. Proc.* **2001**, *591*, 368.

[41] G. W. Ho, A. T. S. Wee, J. Lin, *Appl. Phys. Lett.* **2001**, *79*, 260.

[42] L. Tapaszto, P. Nemes-Incze, Z. Osvath, A. Darabont, P. Lambin, L. P. Biro, *Phys. Rev. B* **2006**, *74*, 235422.

[43] B. Dan, G. C. Irvin, M. Pasquali, *ACS Nano* **2009**, *3*, 835.

[44] H. A. Becerril, J. Mao, Z. Liu, R. M. Stoltenberg, Z. Bao, Y. Chen, *ACS Nano* **2008**, *2*, 463.

[45] G. Eda, G. Fanchini, M. Chhowalla, *Nat. Nanotechnol.* **2008**, *3*, 270.

[46] S. Bae, H. Kim, Y. Lee, X. F. Xu, J. S. Park, Y. Zheng, J. Balakrishnan, T. Lei, H. R. Kim, Y. I. Song, Y. J. Kim, K. S. Kim, B. Ozyilmaz, J. H. Ahn, B. H. Hong, S. Iijima, *Nat. Nanotechnol.* **2010**, *5*, 574.

[47] S. Bae, H. Kim, Y. Lee, X. Xu, J.-S. Park, Y. Zheng, J. Balakrishnan, T. Lei, H. Ri Kim, Y. I. Song, Y.-J. Kim, K. S. Kim, B. Ozyilmaz, J.-H. Ahn, B. H. Hong, S. Iijima, *Nat Nano* **2010**, *5,* 574.

[48] A. B. Kuzmenko, E. van Heumen, F. Carbone, D. van der Marel, *Phys. Rev. Lett.*

2008, *100*, 117401.

[49]C. Casiraghi, A. Hartschuh, E. Lidorikis, H. Qian, H. Harutyunyan, T. Gokus, K. S. Novoselov, A. C. Ferrari, *Nano Lett.* **2007**, *7*, 2711.

[50]G. Eda, M. Chhowalla, *Nano Lett.* **2009**, *9*, 814.

[51]C. Jang, S. Adam, J. H. Chen, D. Williams, S. Das Sarma, M. S. Fuhrer, *Phys. Rev. Lett.* **2008**, *101*, 146805.

[52]X. S. Li, W. W. Cai, J. H. An, S. Kim, J. Nah, D. X. Yang, R. Piner, A. Velamakanni, I. Jung, E. Tutuc, S. K. Banerjee, L. Colombo, R. S. Ruoff, *Science* **2009**, *324*, 1312.

[53]S. De, J. N. Coleman, *ACS Nano* **2010**, *4*, 2713.

[54]A. Turchanin, A. Beyer, C. T. Nottbohm, X. H. Zhang, R. Stosch, A. Sologubenko, J. Mayer, P. Hinze, T. Weimann, A. Golzhauser, *Adv. Mater.* **2009**, *21*, 1233.

[55]S. De, P. J. King, M. Lotya, A. O'Neill, E. M. Doherty, Y. Hernandez, G. S. Duesberg, J. N. Coleman, *Small* **2010**, *6*, 458.

[56]A. N. Obraztsov, E. A. Obraztsova, A. V. Tyurnina, A. A. Zolotukhin, *Carbon* **2007**, *45*, 2017.

[57]A. Reina, X. T. Jia, J. Ho, D. Nezich, H. B. Son, V. Bulovic, M. S. Dresselhaus, J. Kong, *Nano Lett.* **2009**, *9*, 30.

[58]X. C. Dong, D. L. Fu, W. J. Fang, Y. M. Shi, P. Chen, L. J. Li, *Small* **2009**, *5*, 1422.

[59]E. Treossi, M. Melucci, A. Liscio, M. Gazzano, P. Samori, V. Palermo, *J. Am. Chem. Soc.* **2009**, *131*, 15576.

[60]J. Choi, H. Lee, K. J. Kim, B. Kim, S. Kim, *J. Phys. Chem. Lett.* **2010**, *1*, 505.

[61]A. Kasry, M. A. Kuroda, G. J. Martyna, G. S. Tulevski, A. A. Bol, *ACS Nano* **2010**, *4*, 3839.

[62]Y. C. Lin, C. Y. Lin, P. W. Chiu, *Appl. Phys. Lett.* **2010**, *96*, 133110.

[63]H. Pinto, R. Jones, J. P. Goss, P. R. Briddon, *J. Phys.: Condens Matter* **2009**, *21*, 402001.

[64]I. Gierz, C. Riedl, U. Starke, C. R. Ast, K. Kern, *Nano Lett.* **2008**, *8*, 4603.

[65]W. Chen, S. Chen, D. C. Qi, X. Y. Gao, A. T. S. Wee, *J. Am. Chem. Soc.* **2007**,

129, 10418.

[66] A. K. Geim, K. S. Novoselov, *Nat. Mater.* **2007**, *6*, 183.

[67] F. Schedin, A. K. Geim, S. V. Morozov, E. W. Hill, P. Blake, M. I. Katsnelson, K. S. Novoselov, *Nat. Mater.* **2007**, *6*, 652.

[68] J. H. Chen, C. Jang, S. D. Xiao, M. Ishigami, M. S. Fuhrer, *Nat. Nanotechnol.* **2008**, *3*, 206.

[69] T. Ohta, A. Bostwick, T. Seyller, K. Horn, E. Rotenberg, *Science* **2006**, *313*, 951.

[70] E. Bekyarova, M. E. Itkis, P. Ramesh, C. Berger, M. Sprinkle, W. A. de Heer, R. C. Haddon, *J. Am. Chem. Soc.* **2009**, *131*, 1336.

[71] S. Y. Zhou, D. A. Siegel, A. V. Fedorov, A. Lanzara, *Phys. Rev. Lett.* **2008**, *101*.

[72] J. H. Lee, D. W. Shin, V. G. Makotchenko, A. S. Nazarov, V. E. Fedorov, Y. H. Kim, J. Y. Choi, J. M. Kim, J. B. Yoo, *Adv. Mater.* **2009**, *21*, 4383.

[73] B. Lamg, *Surface Sci.* **1975**, *53*, 317.

[74] R. E. Peirls, *Helv. Phys. Acta* **1934**, *7*, 81.

[75] Y. Hernandez, V. Nicolosi, M. Lotya, F. M. Blighe, Z. Y. Sun, S. De, I. T. McGovern, B. Holland, M. Byrne, Y. K. Gun'ko, J. J. Boland, P. Niraj, G. Duesberg, S. Krishnamurthy, R. Goodhue, J. Hutchison, V. Scardaci, A. C. Ferrari, J. N. Coleman, *Nat. Nanotechnol.* **2008**, *3*, 563.

[76] C. Valles, C. Drummond, H. Saadaoui, C. A. Furtado, M. He, O. Roubeau, L. Ortolani, M. Monthioux, A. Penicaud, *J. Am. Chem. Soc.* **2008**, *130*, 15802.

[77] D. Li, M. B. Muller, S. Gilje, R. B. Kaner, G. G. Wallace, *Nat. Nanotechnol.* **2008**, *3*, 101.

[78] S. Park, R. S. Ruoff, *Nat. Nanotechnol.* **2009**, *4*, 217.

[79] W. Liu, C. H. Chung, C. Q. Miao, Y. J. Wang, B. Y. Li, L. Y. Ruan, K. Patel, Y. J. Park, J. Woo, Y. H. Xie, *Thin Solid Films* **2010**, *518*, S128.

[80] A. Dato, V. Radmilovic, Z. Lee, J. Phillips, M. Frenklach, *Nano Lett.* **2008**, *8*, 2012.

[81] J. M. Cai, P. Ruffieux, R. Jaafar, M. Bieri, T. Braun, S. Blankenburg, M. Muoth, A. P. Seitsonen, M. Saleh, X. L. Feng, K. Mullen, R. Fasel, *Nature* **2010**, *466*, 470.

[82] Y. Hernandez, V. Nicolosi, M. Lotya, F. M. Blighe, Z. Sun, S. De, I. T. McGovern,

B. Holland, M. Byrne, Y. K. Gun'Ko, J. J. Boland, P. Niraj, G. Duesberg, S. Krishnamurthy, R. Goodhue, J. Hutchison, V. Scardaci, A. C. Ferrari, J. N. Coleman, *Nature Nanotech.* **2008**, *3*, 563.

[83]Y. Hernandez, M. Lotya, D. Rickard, S. D. Bergin, J. N. Coleman, *Langmuir* **2009**, *26*, 3208.

[84]X. L. Li, G. Y. Zhang, X. D. Bai, X. M. Sun, X. R. Wang, E. Wang, H. J. Dai, *Nat. Nanotechnol.* **2008**, *3*, 538.

[85]L. M. Viculis, J. J. Mack, R. B. Kaner, *Science* **2003**, *299*, 1361.

[86]X. L. Li, X. R. Wang, L. Zhang, S. W. Lee, H. J. Dai, *Science* **2008**, *319*, 1229.

[87]A. A. Green, M. C. Hersam, *Nano Lett.* **2009**, *9*, 4031.

[88]Z. S. Wu, W. C. Ren, L. B. Gao, B. L. Liu, J. P. Zhao, H. M. Cheng, *Nano Research* **2010**, *3*, 16.

[89]T. Kobayashi, N. Kimura, J. B. Chi, S. Hirata, D. Hobara, *Small* **2010**, *6*, 1210.

[90]C. Y. Su, Y. P. Xu, W. J. Zhang, J. W. Zhao, X. H. Tang, C. H. Tsai, L. J. Li, *Chem. Mater.* **2009**, *21*, 5674.

[91]X. F. Zhou, Z. P. Liu, *Chem. Commun.* **2010**, *46*, 2611.

[92]W. S. Hummers, O. R. E., *J. Am. Chem. Soc.* **1958**, *80*, 1339.

[93]T. Nakajima, Y. Matsuo, *Carbon* **1994**, *32*, 469.

[94]C. Gomez-Navarro, J. C. Meyer, R. S. Sundaram, A. Chuvilin, S. Kurasch, M. Burghard, K. Kern, U. Kaiser, *Nano Lett.* **2010**, *10*, 1144.

[95]K. Erickson, R. Erni, Z. Lee, N. Alem, W. Gannett, A. Zettl, *Adv. Mater.* **2010**, *22*, 4467.

[96]Z. T. Luo, Y. Lu, L. A. Somers, A. T. C. Johnson, *J. Am. Chem. Soc.* **2009**, *131*, 898.

[97]X. L. Li, H. L. Wang, J. T. Robinson, H. Sanchez, G. Diankov, H. J. Dai, *J. Am. Chem. Soc.* **2009**, *131*, 15939.

[98]Y. Y. Liang, J. Frisch, L. J. Zhi, H. Norouzi-Arasi, X. L. Feng, J. P. Rabe, N. Koch, K. Mullen, *Nanotechnology* **2009**, *20*.

[99]V. Lopez, R. S. Sundaram, C. Gomez-Navarro, D. Olea, M. Burghard, J. Gomez-Herrero, F. Zamora, K. Kern, *Adv. Mater.* **2009**, *21*, 4683.

[100] M. Choucair, P. Thordarson, J. A. Stride, *Nat. Nanotechnol.* **2009**, *4*, 30.

[101] X. S. Li, W. W. Cai, L. Colombo, R. S. Ruoff, *Nano Lett.* **2009**, *9*, 4268.

[102] Y. Lee, S. Bae, H. Jang, S. Jang, S. E. Zhu, S. H. Sim, Y. I. Song, B. H. Hong, J. H. Ahn, *Nano Lett.* **2010**, *10*, 490.

[103] S. Kumar, N. McEvoy, T. Lutz, G. P. Keeley, V. Nicolosi, C. P. Murray, W. J. Blau, G. S. Duesberg, *Chem. Commun.* **2010**, *46*, 1422.

[104] D. Wei, Y. Liu, Y. Wang, H. Zhang, L. Huang, G. Yu, *Nano Lett.* **2009**, *9*, 1752.

[105] W. W. Cai, Y. W. Zhu, X. S. Li, R. D. Piner, R. S. Ruoff, *Appl. Phys. Lett.* **2009**, *95*.

[106] A. Reina, H. B. Son, L. Y. Jiao, B. Fan, M. S. Dresselhaus, Z. F. Liu, J. Kong, *J. Phys. Chem. C* **2008**, *112*, 17741.

[107] M. P. Levendorf, C. S. Ruiz-Vargas, S. Garg, J. Park, *Nano Lett.* **2009**, *9*, 4479.

[108] J. D. Caldwell, T. J. Anderson, J. C. Culbertson, G. G. Jernigan, K. D. Hobart, F. J. Kub, M. J. Tadjer, J. L. Tedesco, J. K. Hite, M. A. Mastro, R. L. Myers-Ward, C. R. Eddy, P. M. Campbell, D. K. Gaskill, *ACS Nano* **2010**, *4*, 1108.

[109] L. J. Cote, F. Kim, J. X. Huang, *J. Am. Chem. Soc.* **2009**, *131*, 1043.

[110] S. Gilje, S. Han, M. Wang, K. L. Wang, R. B. Kaner, *Nano Lett.* **2007**, *7*, 3394.

[111] G. Eda, Y. Y. Lin, S. Miller, C. W. Chen, W. F. Su, M. Chhowalla, *Appl. Phys. Lett.* **2008**, *92*.

[112] F. Kim, L. J. Cote, J. X. Huang, *Adv. Mater.* **2010**, *22*, 1954.

[113] A. Lerf, H. Y. He, M. Forster, J. Klinowski, *J. Phys. Chem. B* **1998**, *102*, 4477.

[114] J. Kim, L. J. Cote, F. Kim, W. Yuan, K. R. Shull, J. X. Huang, *J. Am. Chem. Soc.* **2010**, *132*, 8180.

[115] D. R. Dreyer, S. Park, C. W. Bielawski, R. S. Ruoff, *Chem. Soc. Rev.* **2010**, *39*, 228.

[116] O. C. Compton, D. A. Dikin, K. W. Putz, L. C. Brinson, S. T. Nguyen, *Adv.*

Mater. **2010**, *22*, 892.

[117] C. Y. Su, Y. P. Xu, W. J. Zhang, J. W. Zhao, A. P. Liu, X. H. Tang, C. H. Tsai, Y. Z. Huang, L. J. Li, *ACS Nano* **2010**, *4*, 5285.

[118] D. S. Li, W. Windl, N. P. Padture, *Adv. Mater.* **2009**, *21*, 1243.

[119] L. Song, L. J. Ci, W. Gao, P. M. Ajayan, *ACS Nano* **2009**, *3*, 1353.

[120] M. J. Allen, V. C. Tung, L. Gomez, Z. Xu, L. M. Chen, K. S. Nelson, C. W. Zhou, R. B. Kaner, Y. Yang, *Adv. Mater.* **2009**, *21*, 2098.

[121] M. Chegaar, N. Nehaoua, A. Bouhemadou, *Energy Convers. Manage.* **2008**, *49*, 1376.

[122] K. Bouzidi, M. Chegaar, A. Bouhemadou, *Sol. Energy Mater.* **2007**, *91*, 1647.

[123] J. D. Servaites, S. Yeganeh, T. J. Marks, M. A. Ratner, *Adv. Funct. Mater.* **2010**, *20*, 97.

[124] J. B. Wu, H. A. Becerril, Z. N. Bao, Z. F. Liu, Y. S. Chen, P. Peumans, *Appl. Phys. Lett.* **2008**, *92*, 263302.

[125] Q. Liu, Z. F. Liu, X. Y. Zhong, L. Y. Yang, N. Zhang, G. L. Pan, S. G. Yin, Y. Chen, J. Wei, *Adv. Funct. Mater.* **2009**, *19*, 894.

[126] Z. F. Liu, Q. Liu, Y. Huang, Y. F. Ma, S. G. Yin, X. Y. Zhang, W. Sun, Y. S. Chen, *Adv. Mater.* **2008**, *20*, 3924.

[127] S. S. Li, K. H. Tu, C. C. Lin, C. W. Chen, M. Chhowalla, *ACS Nano* **2010**, *4*, 3169.

[128] H. F. Zhu, T. Li, Y. J. Zhang, H. L. Dong, J. S. D. Song, H. P. Zhao, Z. M. Wei, W. Xu, W. P. Hu, Z. S. Bo, *Adv. Mater.* **2010**, *22*, 1645.

[129] I. W. Hwang, D. Moses, A. J. Heeger, *J. Phys. Chem. C* **2008**, *112*, 4350.

[130] M. S. Arnold, J. D. Zimmerman, C. K. Renshaw, X. Xu, R. R. Lunt, C. M. Austin, S. R. Forrest, *Nano Lett.* **2009**, *9*, 3354.

[131] G. Yu, J. Wang, J. McElvain, A. J. Heeger, *Adv. Mater.* **1998**, *10*, 1431.

Chapter 2

Thermally Reduced Graphene Oxide Electrodes for Organic Solar Cells

It is the fact that the bottle-neck of thermally reduced GO films for organic solar cells is their high sheet resistance. In this chapter, several strategies have been applied to improve the conductivity of RGO films, which finally aim to achieve a high efficiency in P3HT:PCBM heterojuction solar cells. Firstly, the conductivity of RGO films was improved from 550 S/cm to 1300 S/cm by modifying the GO precursor and the reduction process. An efficiency of ~1.0 % was achieved based on 7-10 nm thick RGO film, with a sheet resistance of 0.8-1.1 kOhm/square. However, this value is still much lower than that of ITO based devices. Afterwards, a combination of graphene film and metal grids as hybrid electrodes was proposed. In these hybrid electrodes, graphene film only serves as the short-range conductor and metal grids act as the long-range conductor. As a result, the sheet resistance of the hybrid film was below 200 Ohm/square while keeping the transmittance higher than 80 %. The P3HT/PCBM solar cells based on such hybrid electrodes provided a power conversion efficiency of 2.5 %, which is comparable to that fabricated with commercial ITO electrodes.

2.1 Introduction

The study of graphene films as transparent electrodes to replace the commercial ITO in our group was started in 2006. An initial efficiency of 0.3 % has been achieved.[1, 2] The low efficiency is attributed to the high sheet resistance of the RGO film and the un-optimized solar cell construction. In principle, the conductivity of the pristine graphene is high enough to serve as the transparent electrode for the application in solar cells.[3-6] The low conductivity is due to the presence of large amounts of defects in the RGO films after thermal reduction. Based on GO precursors, to repair the defects during the reduction is thus one of the most efficient approaches to get a high conductivity. Some carbon-rich gases, such as ethanol and acetylene, have been used as external carbon sources to repair the defects in GO films at elevated temperature.[7, 8] Unfortunately, the repair efficiency is low, especially for the thick graphene film (> ~ 10 nm) because carbon atoms are difficult to diffuse into the interlayer spacing of graphene.

Due to the decoration of large amounts of oxygen containing groups (such as carboxyl, hydroxyl, and epoxide groups) on graphene plane and edges, GO sheets are thermally unstable and mainly decomposed at around 200 ^{o}C because of the pyrolysis of the labile oxygen-containing functional groups, yielding CO, CO_2, and steam.[9, 10] It can be concluded that defects in thermally reduced GO films are produced not only in the oxidation process, but also in the course of reduction. Thus, to optimize the reduction process may provide possible means to reduce the defect content in RGO films. Additionally, the size of GO sheets also plays a big role on the conductivity. The utilization of large-sized GO sheets is beneficial for the decrease of edge content in the RGO films.

Besides increasing the conductivity, decreasing the transport distance of carriers in the RGO film is also an efficient strategy to reduce the energy loss when they are used as transparent electrodes in solar cells. A combination of high conductive metal grids to form graphene/metal grid hybrid electrodes will be investigated in this chapter. Remarkably, the sheet resistance of the hybrid graphene electrodes is below 200 Ohm/square while keeping the transmittance higher than 80 %, showing a promising potential in the field of transparent electrode for the organic solar cells.

2.2 Synthesis of graphene oxide

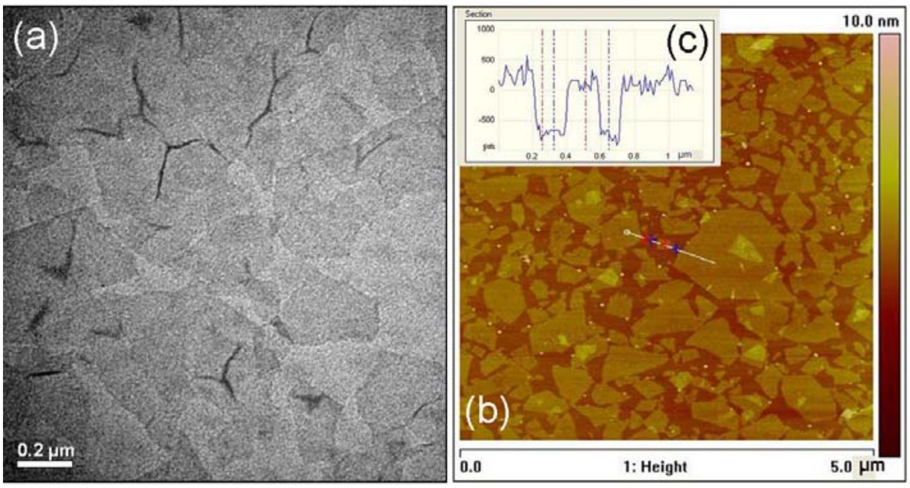

Figure 2.1 (a) TEM image of GO sheets. (b) AFM image of GO sheets on mica, showing the thickness is ~ 1 nm (c).

Currently, Hummers' method is the most common method used for preparing GO.[11] It was found in our experiments that a low temperature oxidation (decreased from 35°C to 22 °C) is beneficial to decrease the ratio of oxygen to carbon in the final GO sheets (as shown in the following IR and XPS characterizations in Figure 2.4 and 2.5, respectively). Thus the modification of the synthesis process will be helpful to improve the conductivity of RGO films prepared from such a precursor. For a typical procedure, natural graphite flakes (10 g, Aldrich) and $NaNO_3$ (7.5 g) were put into a solution of concentrated H_2SO_4 (300 mL) under stirring. After 5 min, $KMnO_4$ (40 g) was slowly added to the reaction mixture over 1 hour. The mixture was stirred at 22 °C for 3 days. Afterwards, 1 L of H_2O_2 solution (1 % in water) was added to the dark brown paste. Then, the mixture was filtered and washed with deionized water. The resulting black cake was re-suspended in deionized water to give a dark brown dispersion, which was subjected to dialysis for 2 weeks to remove residual salts and acids. The brown suspension was dried under vacuum. Exfoliation was carried out by sonicating the as-prepared black solid under ambient condition. The resulting homogeneous brown dispersion was stable for several months and was used for film fabrication, followed by reduction and device fabrications.

After 3 h sonication under a power of 200 W, the lateral size of the GO sheets is less than 1 μm as shown in the transmission electron microscopy (TEM) and atomic force microscopy (AFM) images (Figure 2.1). The dark lines in Figure 2.1(a) are attributed to wrinkle structures of GO sheets, which are formed due to the hydrophobic properties of the underlayer carbon film on the TEM copper grids. These wrinkled structures disappeared when the GO sheets were deposited on the hydrophilic mica substrate (Figure 2.1b). The height profile (Figure 2.1c) shows that the thickness of GO sheets is about 1 nm, which is in good agreement with the value of monolayer GO sheet from literatures.*[12, 13]*

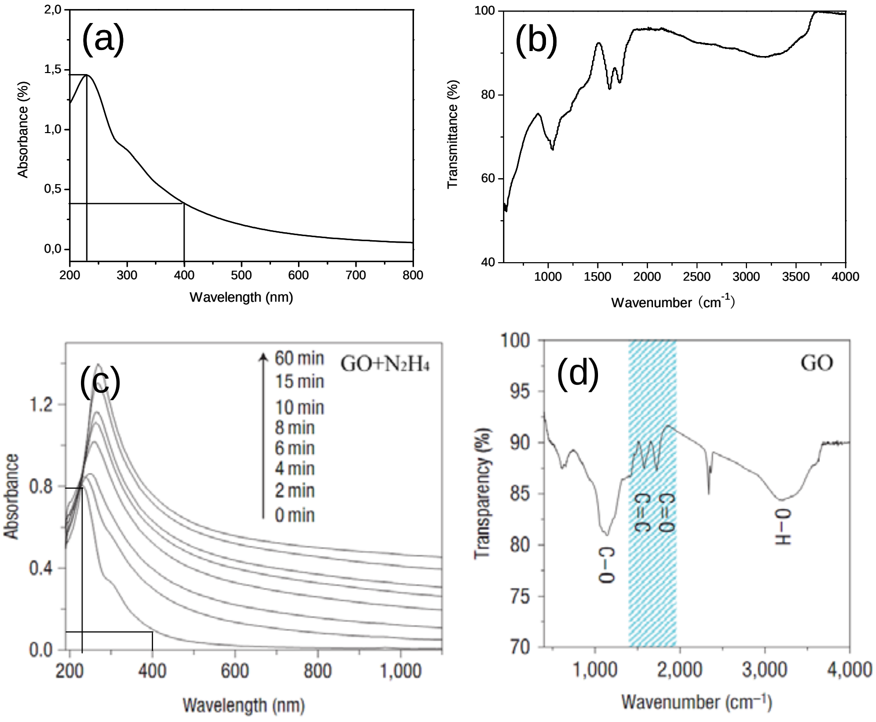

Figure 2.2 UV-vis (a, c) and FT-IR (b, d) spectra of the as low temperature synthesized GO and the reference GO prepared by the traditional Hummers' method,

respectively. (c) and (d) are cited from the literatures.[14, 15]

The low oxygen content of the as-synthesized GO was firstly proved by the UV-vis and FT-IR spectra as shown in Figure 2.2. Figure 2.2(a) presents the UV–vis spectroscopy of the as-synthesized GO dispersion. It can be inferred that the optical absorption of GO is characterized by the $\pi-\pi^*$ plasmon peak near 230 nm and a shoulder peak around 300 nm is attributed to the $\pi-\pi^*$ transitions of C=O.[16] We found that the relative intensity of the peak around 230 nm could be used to evaluate the oxidation degree of GO samples. In the CVD graphene, the ratio of the absorbance at 230 nm to that at 400 nm is ~ 2.0 (Figure 1.1d), while in the reference GO sample prepared by the traditional Hummers' method, the ratio is ~ 8.0 (Figure 2.2c). However, this value is only ~ 4.3 in our as-synthesized GO sheets, indicating of the low content of the oxygen containing groups. The same result was also found from the FT-IR spectrum as shown in Figure 2.2(b). The FT-IR spectrum exhibits more characteristic features, such as intense band at 3430 cm^{-1} (O-H stretching vibrations), 1726 cm^{-1} (C=O stretching vibrations from carbonyl and carboxylic groups), 1588 cm^{-1} (skeletal vibrations from unoxidized graphitic domains), 1226 cm^{-1} (C-OH stretching vibrations), and 1103 cm^{-1} (C-O stretching vibrations).[15, 17, 18] It is worthwhile to note that the intensities of all of the above mentioned peaks are lower than that of the reference GO sample (Figure 2.2b, d).

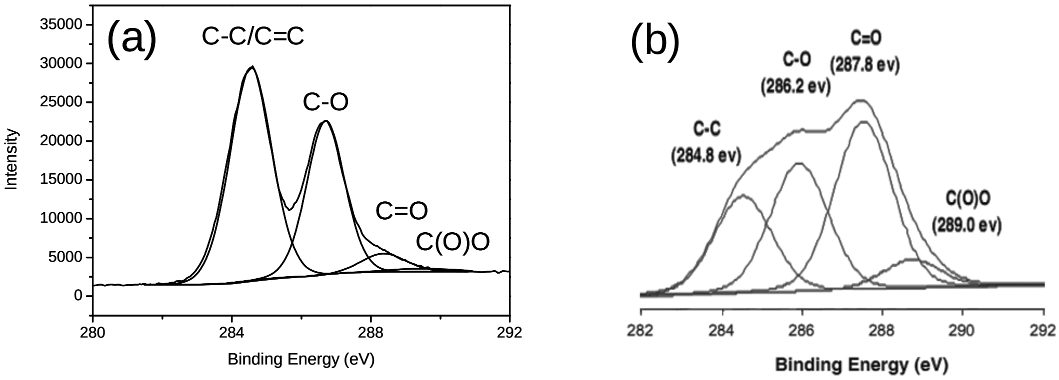

Figure 2.3 C-1s X-ray photoelectron (XPS) spectra of the GO synthesized at low

temperature and the reference GO prepared by the traditional Hummers' method, respectively. (b) is cited from the literature.[10]

The detailed information of the oxygen containing groups was subsequently characterized in the XPS spectrum. Figure 2.3(a) shows the C 1s XPS spectrum of the as-synthesized GO film on silicon substrate, four types of carbon with different chemical states are observed, which appear at 284.5 eV (graphite, C–C/C=C), 286.6 eV (C–O), 287.8 eV (C=O), and 289.0 eV (O–C=O), respectively. Apparently, the intensities of the C–O, C=O and O–C=O peaks are also relatively lower than those reported in the literature for the reference GO samples (Figure 2.3b).[10]

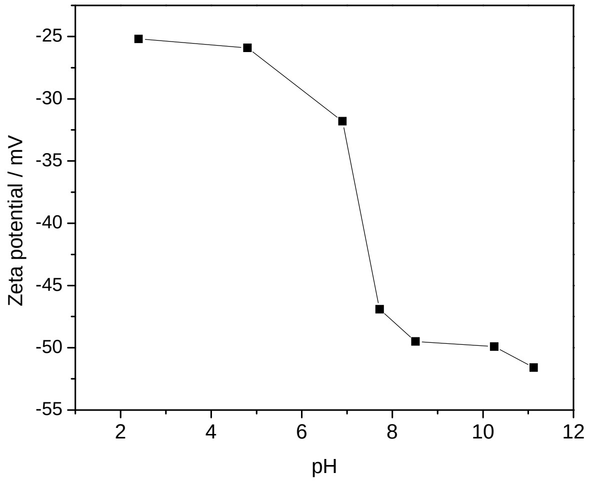

Figure 2.4 Zeta potential of GO in water solution, showing its negative charged property.

Although the content of the oxygen containing groups of the as-synthesized GO is lower than the reference samples, the GO dispersion is still stable enough and suitable for the subsequent film fabrication. The Zeta potential of a 0.05 mg/mL GO in water is shown in Figure 2.4, showing a negatively charged property. It can be concluded that the content of oxygen containing groups in the as-synthesized GO sheets is high enough to keep the GO dispersible and stable for several months. In GO dispersions, ionized carboxyl groups can form electrostatic force to repel each other to prevent aggregation of GO sheets in aqueous solution.

2.3 Fabrication of GO film

There are many methods have been already explored to prepare homogeneous GO films on quartz substrates, such as spray coating, dip coating and spin coating. Each method has its own advantages depending on the application purpose. Spray coating consists in the use of a spray-gun (air brush) to atomize the desire liquid sample into tiny droplets on a substrate. GO sheets in the sprayed droplets tend to aggregate and fold because of the fast evaporation speed of the solvent, resulting in a large roughness. Dip coating is another popular way to prepare thin GO films for research purpose. This process can be divided in five stages: immersion, start-up, deposition, evaporation and drainage. In order to obtain a uniform coating, the substrate is slowly dipped into and withdrawn from a tank containing the GO dispersion at a uniform velocity. For a thick GO film, dip coating should be done repeatedly. Unfortunately, the roughness of GO films will increase with the increase of the dip-coating cycles.

Spin coating is one of the most suitable methods to fabricate homogenous GO films within the thickness ranging from several nanometers to tens of nanometers. For the spin coating, an excess amount of a GO solution is firstly dropped on a substrate, which is then rotated at high speed in order to spread the fluid by centrifugal force. Normally, the thickness of the GO film can be controlled via tuning the concentration of the GO dispersion and the rotary speed of the substrate. It is the fact that tuning the concentration is more efficient than changing the rotary speed on the thickness control.

To spin coat homogenous GO films on quartz substrate for subsequently thermal reduction to form transparent graphene electrodes, 2-6 mg/mL GO dispersion is needed to prepare the film with the thickness ranging from nanometers to tens of nanometers. However, the conventional concentration of GO dispersion is only about 0.5 mg/mL,[14] and it is difficult to directly prepare a higher concentrated GO dispersion by dissolving GO powder in a water solution. In our experiments, the centrifuge technology was used to concentrate the dilute GO dispersion. It was found that a 10000 rpm centrifugation can generate a ~ 6 mg/mL GO colloid at the bottom of the centrifuge tubes. And other concentrated GO dispersion can thus be easily prepared by diluting the above dispersion.

Before film fabrication, the surfaces of substrates should be treated to form a hydrophilic surface to decrease the contact angle of GO dispersion. For glass, quartz, and Si/SiO_2 substrates, piranha solution (concentrated 98 wt.% H_2SO_4 : 30 wt.% H_2O_2 = 3:1 in volume ratio) or oxygen plasma treatments can be applied. For polymer substrates, such as PET, a short-time oxygen plasma treatment (10-30 s) is required.

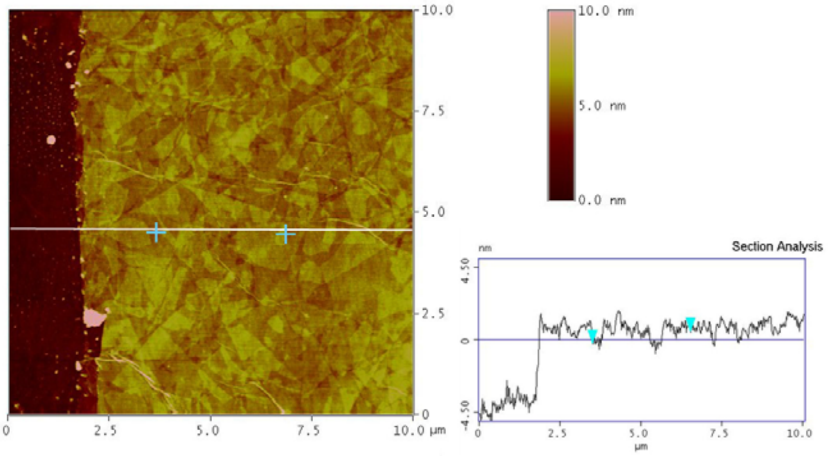

Figure 2.5 AFM images and section analysis of graphene film on quartz substrate prepared by spin coating from GO dispersion.

Figure 2.5 features the AFM image and the section analysis of a GO film prepared by spin coating. The sheet structure of GO remains after spin coating, and all of the sheets are overlapped to form a homogenous GO film. The thickness of the film can be measured by AFM at the edge, which can be produced by a scratch with a knife. After scratching, all the GO sheets can be removed. For GO films with the thickness of tens of nanometers, multi-times spin coating is required. It was found that an annealing treatment of the GO film is necessary to stabilize the formed GO layer on the substrate. Otherwise, the subsequent spin-coating will destroy the formerly deposited GO layer. Although a higher temperature annealing is beneficial to improve its stability, the increased hydrophobic property is unfavorable for subsequent spin-coating in view of uniformity. In our experiments, the pre-coated GO film was annealed at 60 °C for 10 min before performing the subsequent spin-coating.

2.4 Reduction of GO film

GO is an electrically insulating material due to its disrupted sp^2 network. The electrical conductivity can be partially recovered by removing the oxygen containing groups. A variety of low temperature reduction methods have been applied to reduce GO, such as chemical reduction by hydrazine monohydrate or sodium borohydride,[10, 19-21] photoreduction and electrochemical reduction.[22-24] However, the conductivity achieved by these methods can not compete with that of thermally reduced GO films. Another disadvantage of using the above mentioned chemical methods is the introduction of heteroatomic impurities. Taking hydrazine as an example, after reduction, nitrogen component tends to remain on the RGO film surface by covalent bonding.[10] Thus, up to now, thermal reduction is still the most efficient approach to prepare highly conductive RGO films. In our experiments, GO films were firstly prepared by spin coating and then a thermal reduction was carried out in a tube oven at 1100 °C for 30 min under argon atmosphere. The heating rate from 150 °C to 250 °C is 1 °C/min and for the rest ranges is 5 °C/min.

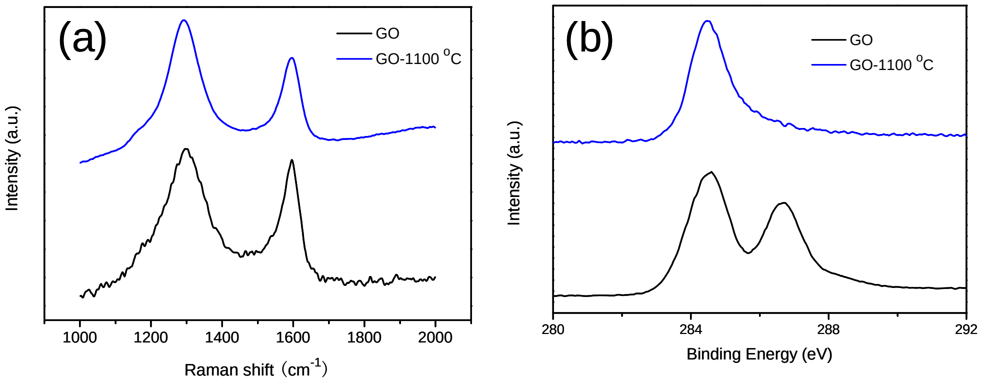

Figure 2.6 Raman (a) and XPS (b) spectroscopies of GO and thermally reduced GO films.

Raman spectroscopy is a widely used tool for the characterization of carbon products, especially considering the fact that conjugated and double carbon-carbon bonds lead to high Raman intensities. The Raman spectrum of the natural graphite only displays a prominent G peak as the only feature at 1581 cm^{-1}, corresponding to the first-order scattering of the E_{2g} mode.*[10]* However, the Raman spectrum of the GO (Figure 2.6a, black) features G (1363 cm^{-1}) and D (1594 cm^{-1}) bands. In GO, the G band broadens significantly and displays a shift to higher frequencies (blue-shift), and the D band grows in intensity. The D band at 1363 cm^{-1}, corresponding to the in-plane A_{1g} zone-edge mode from the in-planer defects and the edges, becomes prominent. The increase of the intensity of D band indicates the reduction in size of the in-plane sp^2 domains, which is because of the introduction of abundant oxygen-containing groups. After thermal reduction, the D band is still very strong as presented in the Raman spectrum (Figure 2.6a, black). The ratio of D/G intensity of RGO even increases compared to that in GO, which indicates the decrease of the average size of the sp^2 domains upon reduction.*[25]* Thus, the thermal reduction can not be simply considered as the removal of the oxygen from the GO planes. Although the conductivity of the thermally reduced GO films is much higher than that prepared by other reduction methods, large amounts of defects still remain in the RGO films, and therefore the graphene structure after reduction can not perfectly restored.

Additionally, the removal of oxygen from the GO sheets via the thermal reduction was also verified by the XPS spectroscopy. In brief, the C1s XPS spectrum of GO (Figure 2.6b, top) indicates a considerable degree of oxidation with four components that correspond to carbon atoms in different functional groups, such as C–C/C=C, C–O, C=O and O–C=O. After thermal reduction at 1100 °C for 30 min, the peak at 284.5 eV is the graphitic structure (C–C/C=C), which is almost unchanged, while the peaks ranging from ~ 286 to ~ 290 eV (C–O, C=O and O–C=O groups) are heavily decreased. The asymmetric peak shape of the RGO film indicates that there are still some oxygen components remaining in the graphene film after the thermal reduction.

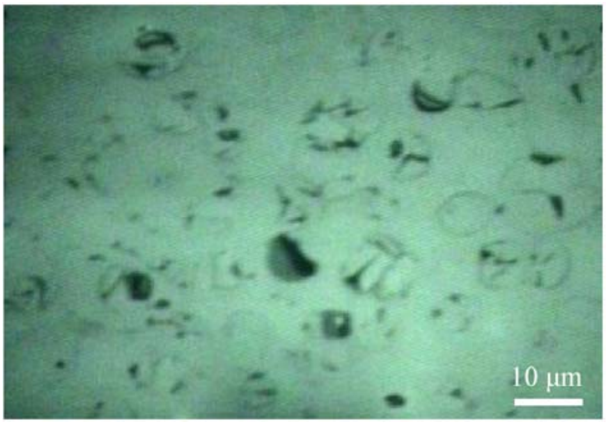

Figure 2.7 Optical microscopy image of 40 nm thick grapnene film prepared by thermal reduction.

During the thermal reduction, large amounts of gas could be generated due to the pyrolysis of the oxygen containing groups. Thus, the thermal reduction for thick films is not as efficient as for thinner ones because thick films can be easily peeled off the substrates after the thermal reduction. Figure 2.7 is a typical optical microscopy (OM) image of a 40 nm thick thermally reduced GO film. It looks like thousands of “bubbles” decorated on the film surface. The size of bubble-like structures is ~ 5-10 μm. It is estimated that a pressure of 40 MPa can be generated at 300 °C, while as high as 130 MPa can be produced at 1000 °C. Thus, those pressures are large enough to separate two stacked GO platelets if the gas can not release from the graphene film immediately.[26] Thus, the thinner the film is, the easier the gas can release from the film. Additionally, the size of GO sheets also exerts a big role on the release efficiency of the as-produced gas. For the GO films prepared from small sized GO sheets, the produced gas can easily release along the spacing (or pathway) formed along the GO edges because of the high edge density, while for GO films prepared from large sized GO sheets, the density of the gas pathway decreases and thus the gas is more difficult to release. In our optimized experiment, a low heating rate of 1 °C/min (from 150 °C to 250 °C) was applied to slow down the gas evolution speed for the reduction of the GO films prepared from large-sized GO sheets.

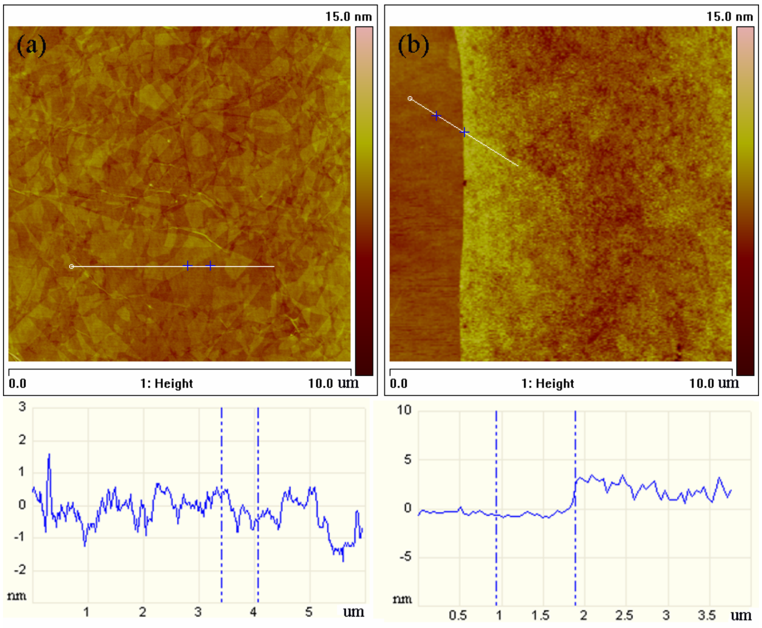

Figure 2.8 AFM and section analysis of GO (a) and 1100 °C thermally reduced GO films (b).

Figure 2.8(a) is the AFM image of a spin-coated GO film and it seems that all of GO sheets arranged parallel to the substrate. The edges of the GO sheets can be distinguished on the height profile. After thermal reduction at 1100 °C for 30 min under the protection of argon, the sheet-like structures disappear as shown in Figure 2.8(b). The evolution of the morphology of the RGO film is due to the removal of carbon and oxygen atoms and possible cross-linking reactions between graphene sheets at elevated temperature. For the RGO film less than ~ 10 nm in thickness, no spontaneous exfoliation (Figure 2.7) has been found after the thermal reduction. Additionally, the adhesion between the graphene and the substrate can be extremely enhanced by the heating treatment. The as-prepared RGO film can survive in the sonication treatment in acetone for 30 min. Compared to the GO film before reduction, the surface roughness R_a (arithmetic mean value) is improved significantly in the RGO film. The average R_a of the as-prepared RGO film over a 10×10 μm^2 area is ~ 0.78 nm, which is smooth enough for optoelectronic devices.[2]

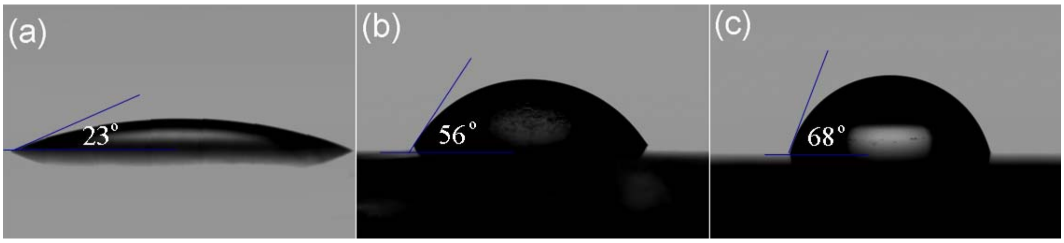

Figure 2.9 The contact angles of the GO, 250 °C annealed GO, and 1100 °C thermally reduced GO films, respectively.

The surface property of RGO films is very important for the device fabrication and has been studied by a contact angle measurement as shown in Figure 2.9. The spin-coated GO film is hydrophilic and the contact angle is ~ 23° without any thermal annealing (Figure 2.9a). After annealing at 250 °C for 30 min, the contact angle increases quickly to ~ 56° (Figure 2.9b). The big improvement of the hydrophobic property is attributed to the removal of the most of the hydrophilic oxygen containing groups. The subsequently thermal reduction at 1100 °C can further increase the contact angle to 68° (Figure 2.9c). It is noteworthy that this value is lower than that of the freshly cleaved HOPG surface (81 °C) possibly because of the presence of defects in RGO films.

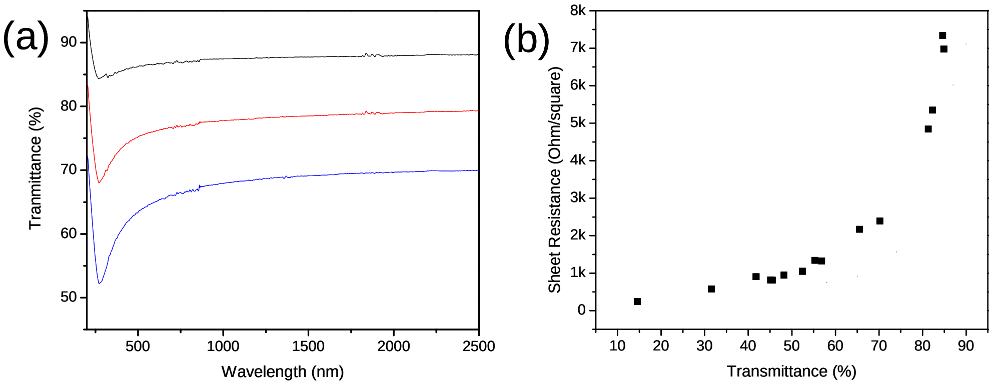

Figure 2.10 (a) Transmittance of the RGO films with different thickness. (b) Sheet resistances of RGO films on quartz substrates as function of light transmittances at 500 nm.

Figure 2.10(a) is the transmittance of the RGO films with different thickness in the ultraviolet-visible and near-infrared ranges (UV/Vis–NIR). The only absorption peak appears at ~ 270 nm, reflecting π-electron concentration and structural ordering, which is consistent with the restoration of sp^2 carbon and possible rearrangement of atoms.*[27]* Most interestingly, in contrast to Fluorin Tin Oxide (FTO) and ITO, which show strong light absorption in the region of near and short wave infrared, the graphene film is transparent within a broad range. This unique optical property makes graphene films outstanding as window electrodes for optoelectronics applicable to a wide range of wavelengths.

Figure 2.10(b) summarizes the sheet resistance of as-prepared RGO films as function of the transmittance (500 nm) on quartz substrates after 1100 ^{o}C thermal reduction. As an ideal transparent electrode, graphene films should be highly transparent to decrease the light reflection and absorption. For this purpose, the graphene films should be as thin as possible. However, thinner film can produce a large resistance, which is extremely hazardous for carrier collection and transport. Thus, there is a tradeoff of the transmittance and the resistance for the application of transparent electrode in solar cells (Figure 2.15). The RGO films with different sheet resistance/transmittance were prepared by controlling the film thickness. The concentration of the GO precursor is ranging from 2 mg/mL to 6 mg/mL, and the spin speed is from 1000 rpm to 3000 rpm. In order to keep the light absorption less than 20 % (500 nm), the sheet resistance of RGO film should be higher than 5k Ohm/square.

2.5 Optimization of solar cell construction

As discussed in the introduction in this chapter, the current research efforts for improving the efficiency of graphene electrode based organic solar cells are centered on two directions: optimizing the solar cell device construction and improving the conductivity of the RGO film. The working principle of the organic solar cells is depicted in Figure 2.11.

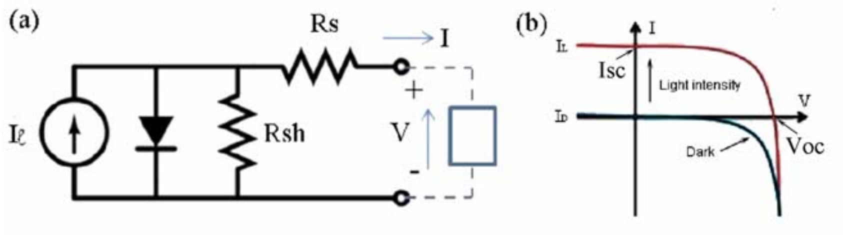

Figure 2.11 (a) Simplified equivalent circuit model for a solar cell. (b) Illuminated current-voltage (I-V) sweep curve under dark and light, respectively.

Simply, a solar cell is a photovoltaic device and can be modeled as a current source in parallel with a diode as shown in Figure 2.11(a). R_s is the series resistance and R_{sh} is the shunt resistance or parallel resistance. When there is no light present to generate any current, the solar cell behaves like a diode. When exposed to the light, current can be generated by the solar cell as shown as the red curve in Figure 2.11(b). Many performance parameters of the solar cell can be determined from this I-V curve.

The short circuit current (I_{sc}) corresponds to the short circuit condition when the impedance is low and is calculated when the voltage equals 0. The open circuit voltage (V_{oc}) occurs when there is no current passing through the cell (I = 0). The fill factor (FF) is essentially a measure of the quality of the solar cell. Efficiency (η) is the ratio of the electrical power output compared to the solar power input into the solar cell.

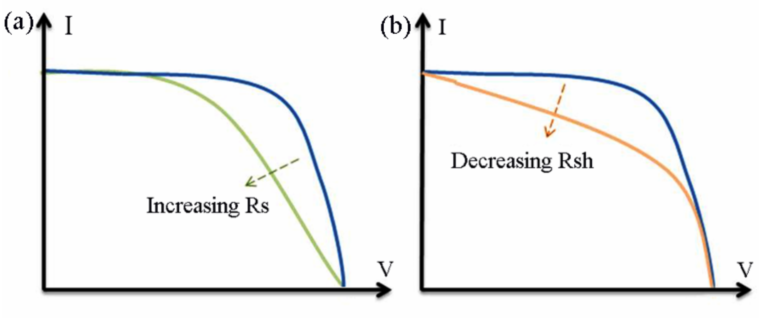

Figure 2.12 Effect of increasing R_s (a) and decreasing R_{sh} (b) on the I-V curves.

During operation, the efficiency of solar cells can be reduced by the dissipation of power across internal resistances. For an ideal cell, R_{sh} would be infinite and would not provide an alternate path for current to flow, while R_s would be zero, resulting in no further voltage drop before the load. Thereby, both increasing R_{sh} and decreasing R_s would be beneficial for the improvement of the power efficiency. On the contrary, if R_{sh} is decreased too much, V_{oc} will drop, while high R_s will cause a low I_{sc} (Figure 2.12a, b). In our experiments, hole and electron transfer buffer layers were introduced to increase R_{sh}. Afterwards, the thickness-dependent performance of graphene films from 2 to 40 nm was studied in P3HT:PCBM solar cells. Subsequently, the efficiency of the graphene based solar cells was further improved by decreasing R_s.

2.5.1 Buffer layer

In the graphene/P3HT:PCBM/Al solar cell, although graphene and aluminium electrodes can offer an internal potential to sweep the holes and electrons to the opposite electrodes, the recombination of holes and electrons always occurs at the interface of the electrodes/active materials, resulting in a low power efficiency. PEDOT:PSS, MoO_3, V_2O_5 have been widely used in photovoltaic devices due to their hole transport/electron blocking characteristics.*[28-30]* For the electron transport/hole blocking layer, LiF, TiO_2 and ZnO already show excellent performance.*[31-33]* In our experiments, PEDOT:PSS and ZnO buffer layers were introduced to the graphene based P3HT:PCBM heterojunction solar cell to increase the R_{sh}.

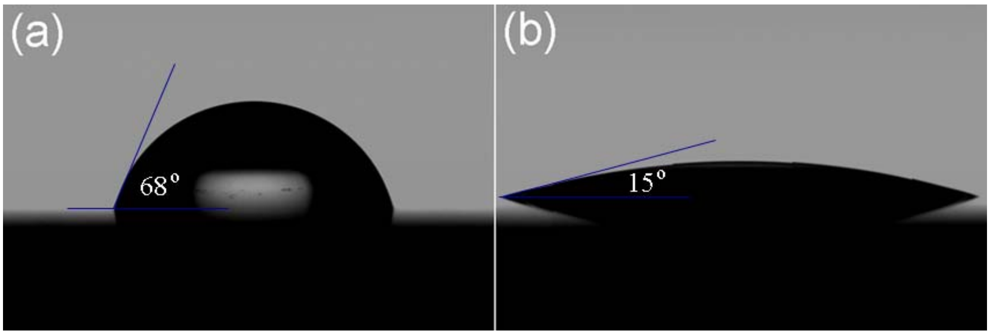

Figure 2.13 The contact angles of the thermally reduced GO film (a) and

PEDOT:PSS modified RGO film (b).

PEDOT:PSS is widely used hole transport/electron blocking buffer layer for organic solar cells due to its ease of processing. However, PEDOT:PSS is based on a water solution, and it is difficult to directly fabricate a homogenous thin film on the hydrophobic RGO films. Figure 2.13(a) demonstrates the hydrophobic RGO film with a contact angle of 68^o. Therefore, a pre-treatment of the RGO film is required to improve its hydrophilicity. However, the traditional oxygen plasma and piranha solution treatments are not feasible because they will destroy the RGO film. In this regard, PEDOT:PSS is used to modify the RGO film to a hydrophilic surface. Firstly, a thick PEDOT:PSS layer was firstly drop-casted on the RGO film and annealed at 150 ^oC for 30 min and then washed away with water. It was found that the surface can be successfully modified by the PEDOT:PSS, resulting in the enhancement of the hydrophilicity. As a result, the contact angle of the pre-treated graphene film was decreased from 68^o to 15^o, which is even lower than that of GO film (23^o, Figure 2.11a) and is ready for the following device fabrication.

On the other hand, ZnO is used as electron transport/hole blocking buffer layer for its high transparency, low-cost fabrication from a sol-gel process and good electron transport property. The synthesis of ZnO nanoparticles proceeds as follows:[34] Zinc acetate dihydrate (98 %, 2.95 g, 13.4 mmol) was dissolved in methanol (125 mL) at 60 °C, a solution of KOH (87 %, 1.48 g, 23 mmol) in methanol (65 mL) was added in 10 min to the zinc acetate dihydrate solution under vigorous stirring. Zinc hydroxide precipitated but dissolved again. After 1.5 h, the nanoparticles started to precipitate and the solution became turbid. After 2 h and 15 min, the heater and stirrer were removed and the nanoparticles were allowed to precipitate. The precipitate was firstly washed 5 times with methanol and then dissolved in n-butanol to form a slightly translucent, almost transparent ZnO dispersion, which was stable for more than two months.

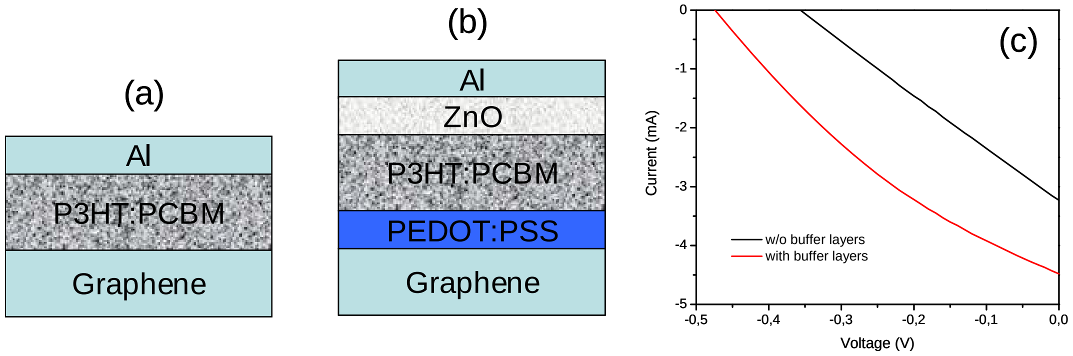

Figure 2.14 Illustration of the solar cell (a) without buffer layers; (b) with ZnO and PEDOT:PSS as the buffer layers; (c) Current-Voltage (I-V) curves of the solar cells in the structure (a) and (b).

Based on the modified RGO electrodes, the fabrication procedure for the P3HT/PCBM heterojunction solar cells is similar to that for the traditional ITO based devices. In a typical experiment, a thin conducting PEDOT:PSS layer was firstly spin-coated on the pre-modified RGO film and then dried at 150 °C for 15 min in air. The following device fabrication and measurement were carried out in a nitrogen filled glove-box. A dichlorobenzene solution comprising P3HT (10 mg/mL) and PCBM (8 mg/mL) was spin-coated at 700 rpm for 40 s on the top of the PEDOT:PSS layer. After a slow drying process of the active P3HT:PCBM layer, a ~ 10 nm thick ZnO film was spin-coated on the active materials from the n-butanol solution after through a 200 nm hydrophilic filter. Finally, a 100 nm thick aluminum layer was evaporated through a mask onto ZnO layer to form the cathode (6 mm^2 active area). Post annealing was carried out at 140 °C for 10 min in the glove-box. I-V curves were recorded with a Keithley 236 Source Measuring Unit. The solar light was obtained from the solar simulator (Lichttechnik, Germany) using a 575 W metal halide lamp, in combination with an ODF filter, to produce a spectral distribution close to the global radiation AM1.5 G. The light intensity was adjusted to 1000 W/m^2 using a commercial silicon reference cell. The structures of the solar cells without and with the PEDOT:PSS and ZnO layers are illustrated in Figure 2.14(a, b). The performances of RGO film (~ 10 nm thick) based solar cells with and without buffer layers are compared in Figure 2.14(c). The power efficiency of the solar cell with buffer layers (red, 0.70) is more than once higher than the device without any buffer layer (black, 0.31 %). This improvement is attributed to the increase of the R_{sh} via introducing the PEDOT:PSS and ZnO buffer layers, resulting in an increased short circuit current (from 3.2 to 4.5 mA) and open circuit voltage (from 0.36 to 0.48 V). In this case, although the resistance of the transparent graphene electrode is unchanged, the ratio of the R_s/R_{sh} is decreased by increasing the R_{sh}, also resulting in the increase of the FF value from 0.25 to 0.31 (Figure 2.14c). We need to mention that all the following solar cell devices were fabricated with PEDOT:PSS and ZnO as buffer layers (Figure 2.14b).

2.5.2 Thickness-dependent performance

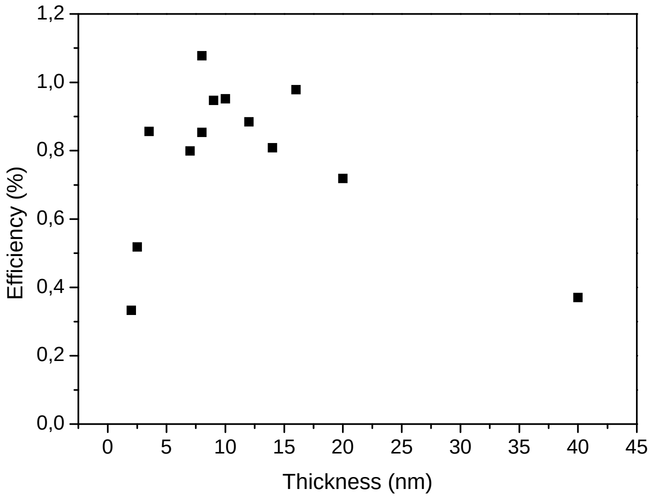

Figure 2.15 Thickness-dependent performance for graphene based P3HT:PCBM solar cells with PEDOT:PSS and ZnO as the buffer layers.

There is a tradeoff of the transmittance and the resistance of RGO films when they are used as transparent electrodes in the P3HT:PCBM solar cells. In order to study the thickness-dependent performance, a series of solar cells were fabricated and their corresponding power efficiencies were summarized in Figure 2.15. Resistance and transmittance are the two basic factors that determine the final power efficiency of the graphene based solar cells. Although high transmittance allows more light to pass through the RGO film to reach the active polymer, a significant amount of energy would be wasted on the resistance of the RGO film in the form of heat. Although the thick film can decrease the energy loss at the graphene electrodes, a low transmittance will reduce the total sunlight reaching the active area which can also diminishes the efficiency. In the present case, the RGO films with thickness of 7-10 nm exhibited relatively high efficiency as shown in Figure 2.15. For this particular film, the transmittance is about 55 % (500 nm) and the sheet resistance is ~ 1.0-1.5 kOhm/square.

2.6 Improvement of conductivity

As discussed in the section 2.5 on the solar cell working principle, the series resistance in an ideal solar cell should be zero. Although graphene is considered as a promising candidate to replace ITO due to its excellent chemical stability and flexibility, the low conductivity highly limits its development. It has been reported that a structurally perfect multilayer graphene films are conductive enough to replace ITO as the transparent electrodes.[3, 4, 35] The low conductivity of RGO films is attributed to the presence of large amounts of defects.[8, 36] During the thermal reduction process, the gas are produced in the form of CO, CO_2 etc.[10] Therefore, the defects in the RGO film are generated not only in the oxidation process, but also in the course of reduction. We propose that the defect can be decreased via optimizing the reduction process. On the other hand, besides the defects from the in-planar sites of holes or some functional groups, defect arising from inter-sheet junctions can also play a big role on the conductivity. For instance, the inter-sheets junction density can decrease by 50 % when one compares GO films prepared from 2 μm sized GO sheets to 1 μm sized GO sheets. And for 5 μm sized GO sheets as precursors, the edge density can even decrease by 80 %. Therefore, the use of large-sized GO precursors will also be beneficial to improve the conductivity.

2.6.1 Two-step reduction

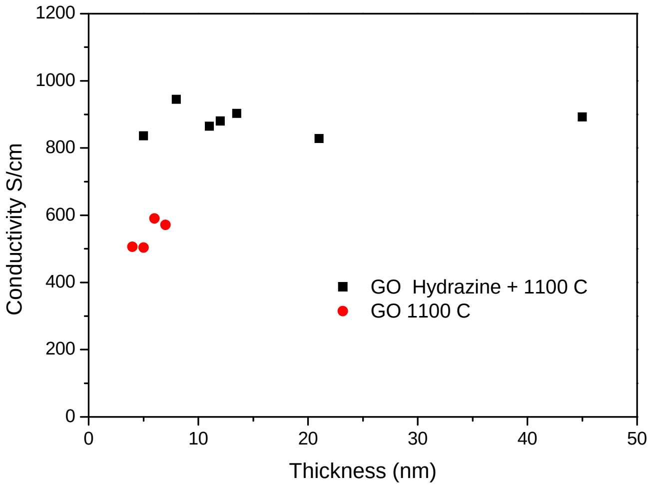

Figure 2.16 Comparison of the conductivities of RGO film prepared by thermal reduction (a) and a combination of N_2H_4 reduction and thermal reduction (b).

For the first step, a chemical reduction was carried out by exposing the GO film to N_2H_4 vapor at room temperature overnight (or at 80 °C for 1 hour). During this process, the color the GO film changed from yellow to grey, indicating the restoration of the sp^2 domains. Afterwards, the chemically reduced GO films were transferred to a horizontal tube oven to heat to 1100 °C for 30 min using the same procedure as mentioned above (the heating rate from 150 °C to 250 °C is 1 °C/min and for the rest ranges is 5 °C/min.).The two-step reduction with a combination of chemical and thermal reductions can additionally improve the conductivity of RGO films (Figure 2.16). For instance, the conductivity of a ~ 5 nm thick RGO film was increased from ~ 550 S/cm to ~ 900 S/cm due to the low defect content because less carbon was lost in the two-step reduction process.

TGA results can explain the improvement of the conductivity by the two-step reduction, which is attributed to less carbon atoms removal from the film, resulting in relatively lower defects content (Figure 2.17). GO powder starts to obviously lose mass at ~ 200 °C due to the pyrolysis of the labile oxygen-containing functional groups.[9, 10, 37] It is interesting that the N_2H_4 reduced GO seems more stable than GO, and exhibits low weight loss during the subsequently thermal reduction. The weight loss of a N_2H_4 reduced GO from 100 °C to 500 °C is only ~ 30 %, which is much lower than that of GO (~ 42 %).

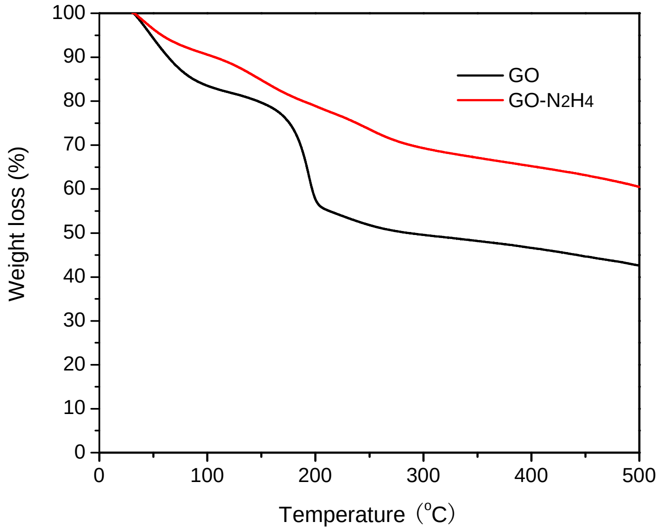

Figure 2.17 Thermogravimetry analysis (TGA) of GO and the N_2H_4 reduced GO powder.

2.6.2 Graphene film from large-sized GO

Since the in-plane conductivity on RGO films is higher than that in the vertical direction, using large GO sheets as the precursor is proposed to be another efficient approach to seek the high conductivity because edges density can be efficiently decreased. To synthesize large GO sheet precursors, the oxidation procedure was kept the same as in the modified Hummers' method, the difference occurred only in the exfoliation process. The sonication treatment of the GO dispersion was replaced by a gentle shaking. It is the fact that the GO sheets can also be spontaneously exfoliated without sonicating treatment when the pH value of the GO dispersion increases to neutral. In this way, large GO sheets can be easily synthesized. Subsequently, the ultra-large monolayer GO sheets were further delaminated via centrifugation of the

GO dispersion at different centrifugation speeds.

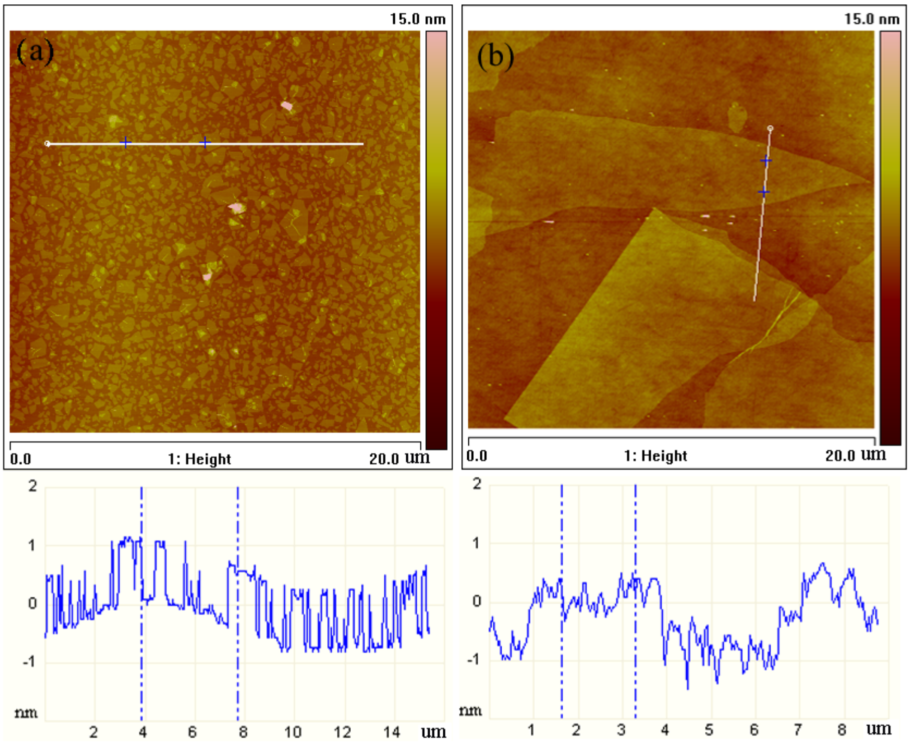

Figure 2.18 AFM images of ultra-large GO sheets obtained by shacking (a) and small ones obtained after sonication (b).

Figure 2.18(a) shows the AFM image of GO sheets prepared by the normal sonication-assisted exfoliation process (200 W, 3 h, 0 ^{o}C). The lateral size of the GO sheets ranges from ~ 200 nm to 1 um as illustrated in Figure 2.18(a). After replacing the sonication treatment by a gentle shaking in a very dilute H_2O solution, the lateral size of the GO sheets can be kept at a very large size of 10-20 um (Figure 2.18b). The large GO sheets are brittle and are easily cut to small pieces by the sonication treatment. Together with the density gradient ultracentrifugation, GO dispersions with different sizes can be easily prepared. The edge density in the GO films prepared from the small sized GO precursors (Figure 2.18a) is more than 10 times higher than those prepared from larger ones (Figure 2.18b). It is therefore proposed that the conductivity of GO films prepared from large-sized GO sheets can be improved.

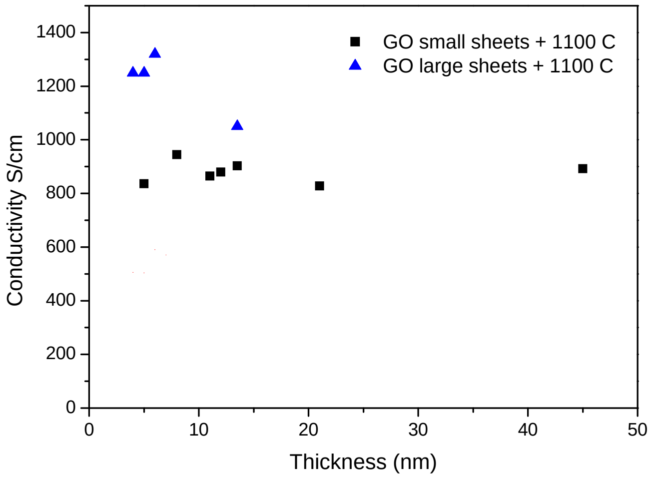

Figure 2.19 Conductivities for GO films obtained from differently sized GO sheets after a two-step reduction process.

As expected, the conductivity of a ~ 5 nm thick RGO films prepared from the large GO sheets is nearly 1300 S/cm as shown in Figure 2.19, which is one of the highest values reported for RGO films.[8, 38] However, for a ~ 15 nm thick film, the conductivity is lower (~ 1000 S/cm), which is possibly due to the poor morphology of the RGO film after thermal reduction. It was found that, for thick films (> 10 nm), the graphene sheets are easily exfoliated from the substrate because the generated gas is difficult to be released during the thermal reduction. In this way, the roughness of the thick RGO films is larger than that for the thinner ones. Despite the high electrical conductivity for the graphene electrodes up to 1300 S/cm, it is still too low to be used as the transparent electrode in solar cells.

2.7 Graphene/metal grid hybrid electrodes for solar cells

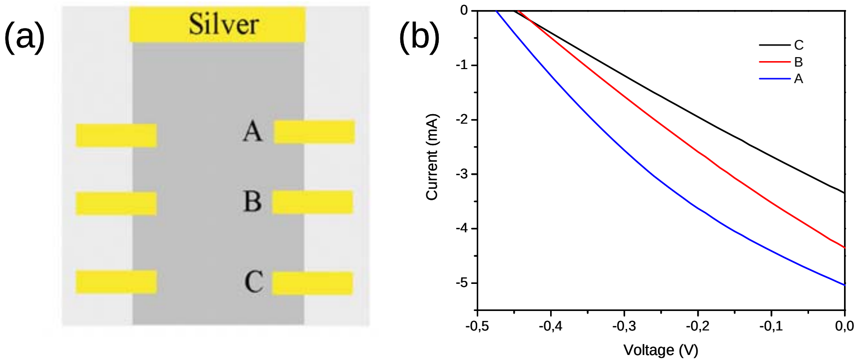

Figure 2.20 The efficiencies of the cell A, B, C are 0.81 % 0.53 % and 0.40 %, respectively.

Due to the large sheet resistance of the graphene electrodes, the efficiency of the solar cells highly depends on the position of the solar cell on the RGO film as illustrated in Figure 2.20(a). Comparing the I-V curves of the cells A, B and C (Figure 2.20b), it can be found that the short circuit current I_{sc} is increasing along with the decrease of the distance between the cells and the silver paste, while their open circuit voltages V_{oc} of the three cells are similar. The power efficiencies of the cell A, B and C are 0.81 %, 0.53 %, and 0.40 %, respectively. According to the aforementioned working principle (Figure 2.11, 2.12), the difference of efficiency lies in the different series resistance R_s of these three solar cells. The large distance from the cell to the silver paste can add a big series resistance to the P3HT:PCBM solar cell, resulting in a low FF value and a low I_{sc}. The resistance of the RGO film from the silver paste to the cell C is nearly twice higher than that of cell A, which can produce a large discrepancy in the device efficiencies.

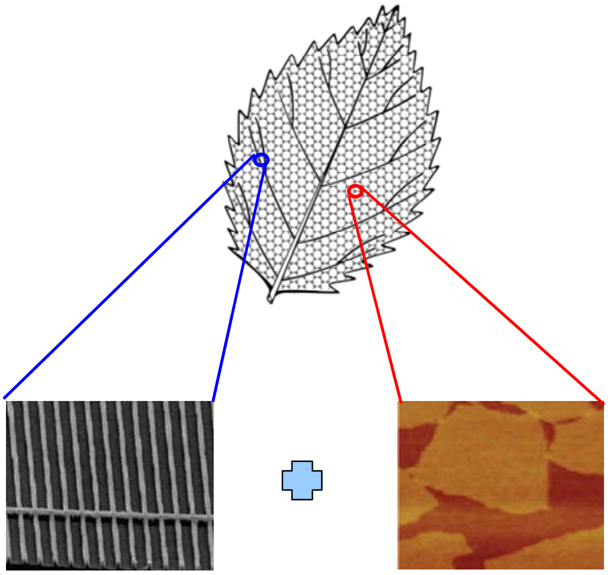

Figure 2.21 The concept of graphene/metal grid hybrid electrodes for solar cells.

Motivated by the above results, metal grids are proposed for introduction into the graphene film to form graphene/metal grid hybrid electrodes, which therefore can lead to a significant reduction of the series resistance of the solar cells. In such electrode structures, the graphene film only serves as the short-range conductor and the metal grids act as the long-range conductor as illustrated in Figure 2.21. These hybrid electrodes have been successfully fabricated by patterning a metal web on top of a thermally reduced GO film. We argue that the combination of graphene film and metal grids is an ideal concept toward highly conductive and cost effective transparent electrodes.

There have been many candidates for replacing doped metal oxide films as transparent electrodes in solar cells, like metal grids, metal wires, carbon nanotubes, doped PEDOT:PSS and graphene films. These materials can be divided into two categories: one is a web structure and the other is a homogenous film. Taking web-like metal grids as an example, the conducting path way is only along the metal grids and light can go through the space between the metal grids. One of the requirements of such a kind of transparent electrodes is that the coverage of the metal grids should be low enough to provide a high transmittance. Another requirement is that the distance between the metal grids can not be so large because there is a limitation of the diffusion length (mean free path) of the carriers in organic semiconductors. Generally, the distance of the adjacent metal grid should be less than 1 μm to efficiently collect the carriers.[39] In this case, the width of the grid should be less than 100 nm to provide > 90 % transmittance. However, photolithography or printing technologies can not define such narrow structures. The second category is the film electrodes, where the transmittance can be tuned by controlling the thickness. In this regard, the resistance is the main factor that limits their application. A combination of these two kinds of electrodes (graphene and metal grids) together can therefore avoid their disadvantages. We can expect that the metal grids in the hybrid electrodes do not need short grid-grid distance because the carriers can be firstly collected by the graphene film and then transferred to the adjacent metal grid. The graphene film also does not need to be very thick because it only serves as a short-range conductor to transfer the carriers to the nearest metal grid.

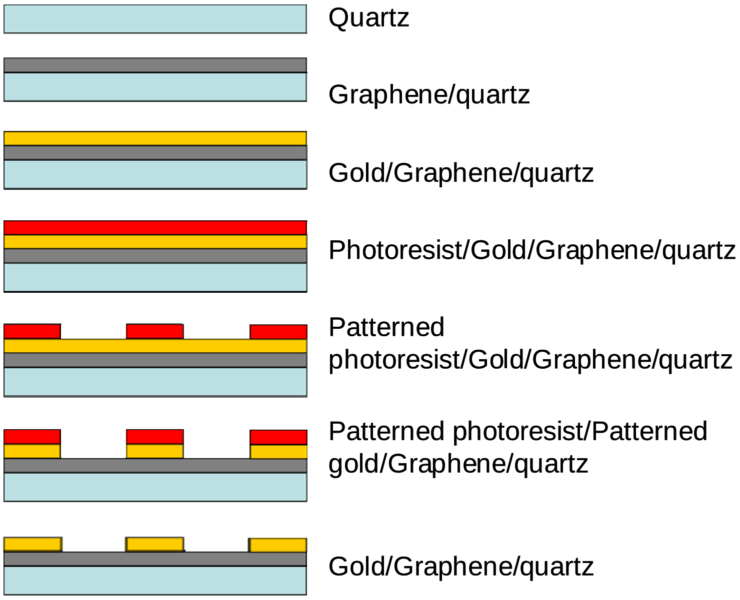

Scheme 2.1 Illumination of the fabrication process of the graphene/metal grid bybrid electrode.

In this work, metal grids were patterned on a RGO film by photolithography as shown in Scheme 2.1. The lithographic process was performed in a clean room in order to avoid contamination of the samples by dust particles. Firstly, a ~ 3 nm thick RGO film was fabricated via thermally reducing the spin coated GO film on a quartz substrate. And then 30 nm thick gold film was evaporated on top of the RGO film. Subsequently, the positive photoresist PR-AZ 5214E was spin coated on the gold film at 4000 rpm for 40 seconds and then annealed at 90 ^{o}C for 30 min to remove residual solvents in the photoresist film. Afterwards, these samples were pressed against a mask containing the desired electrode structure. The mask consists of quartz on which the structures that are made out of a thin chrome layer. Then the substrate (covered by the mask) was exposed to a UV light for 25 seconds. In this process, only the parts of the photoresist that were exposed to UV light becomes soluble to a mixture of AZ 351B and water (1:4 in volume, 14 s). After rinsing with water, the patterned photoresist was formed on the gold surface. The etching of the gold film to the gold grids was carried out in gold etchant (KI:I_2:H_2O = 4:1:40) for 60 seconds. The gold protected by the photoresist remained on the substrate, forming web-like metal grids structures. Finally, after washing away all the photoresist (on the gold surface) with acetone, the graphene/metal grid hybrid electrodes were established.

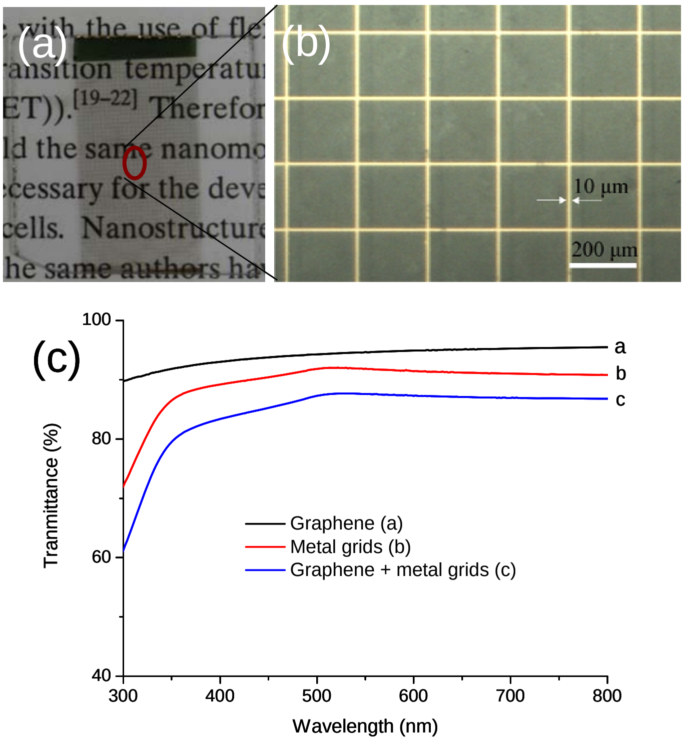

Figure 2.22 (a) Photography of graphene/metal grid hybrid electrodes on quartz substrate. (b) OM image of the graphene/metal grid hybrid electrodes. (c) Transmittance of the metal grids, 3 nm thick graphene film and the graphene/metal grid hybrid electrodes.

Figure 2.22(a) shows an image of the 12 mm × 24 mm graphene/metal grid hybrid electrodes on a 24 mm × 24 mm quartz substrate. The distance of metal grids is 200 µm and the width of the grid is 10 µm (Figure 2.22b). Thus, the transmittance of the metal grids is higher than 90 %. Graphene films with different transmittances can be fabricated by controlling the thickness. The combination of the graphene film with 94 % transmittance and the metal grids with 91 % transmittance produced the hybrid graphene/metal grid electrodes with a transmittance of 86 % as shown in

Figure 2.22(c). It is worthy to note that both the thickness of the graphene film and the size of the metal grids can be tuned according to the requirement of the transmittance and the resistance for different applications.

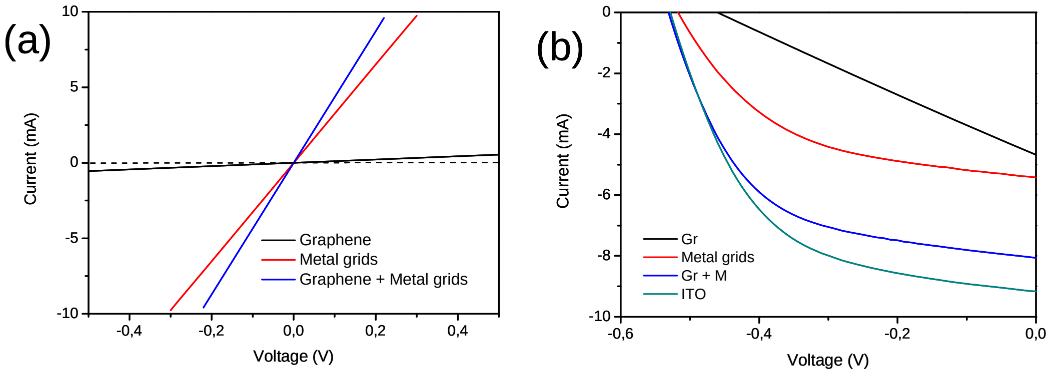

Figure 2.23 (a) I-V curves of the 3 nm thick graphene film, metal grids, and graphene/metal grid hybrid electrodes, respectively. (b) The I-V curves of the graphene, metal grids, graphene/metal grid hybrid, and ITO based P3HT:PCBM solar cells.

In the hybrid electrodes, the distance between gold grids is 200 μm, thus the carriers only need to travel ≤ 100 μm to the nearest metal grid. Although the sheet resistance of the graphene film (transmittance of 94 %) used is ~ 20 kOhm/square, the resistance from the center of the graphene film to the metal grid is less than 400 Ohm, corresponding to a sheet resistance of 150 Ohm/square (Figure 2.23a). With these results in our hand, a P3HT:PCBM solar cell based on the graphene/metal grid hybrid electrodes has been fabricated, which affords a power efficiency of up to 2.5 %. This value is about 4 times higher than that of cell with pure graphene film as the transparent electrode (0.7 %). Comparing the I-V curves in Figure 2.23(b), both I_{sc} and FF value are improved by adding the metal grids as the long-range conductor. The efficiency achieved based on the hybrid electrodes is close to that of ITO based solar cells as shown in Figure 2.23(b). The slightly lower efficiency is proposed due to the lower transmittance of this film than ITO. Nevertheless, we believe that the present strategy of using graphene as the short-range conductor may open up a new pathway to explore cost efficient method to prepare transparent graphene electrodes.

2.8 Conclusion

Transparent, conductive, and ultrathin graphene films, as an alternative to the ubiquitously employed metal oxides window electrodes for solar cells, are demonstrated. By modifying the GO precursor and the reduction process, the conductivity of RGO film bas been improved from ~ 550 S/cm to ~ 1300 S/cm. Taking a 10 nm thick RGO film as an example, the sheet resistance is ~ 800 Ohm/square. However, such resistance is still too high to serve as the transparent electrode in solar cells. A combination of graphene film and metal grids as hybrid electrodes has been proposed to further decrease the resistance. In these hybrid electrodes, graphene film serves as the short-range conductor and metal grids act as the long-range conductor. The sheet resistance of these hybrid electrodes has been efficiently reduced to < 200 Ohm/square, which provides an efficiency of ~ 2.5 % for the P3HT:PCBM solar cell, which is comparable to that of a ITO based device. We believe that the combination of 2D graphene films and 1D metal grids (or wires) will be beneficial for low cost requirement of the transparent graphene electrodes.

References

[1] X. Wang, L. J. Zhi, N. Tsao, Z. Tomovic, J. L. Li, K. Mullen, *Angew. Chem. Int. Ed.* **2008**, *47*, 2990.

[2] X. Wang, L. J. Zhi, K. Mullen, *Nano Lett.* **2008**, *8*, 323.

[3] S. De, J. N. Coleman, *ACS Nano* **2010**, *4*, 2713.

[4] S. Bae, H. Kim, Y. Lee, X. F. Xu, J. S. Park, Y. Zheng, J. Balakrishnan, T. Lei, H. R. Kim, Y. I. Song, Y. J. Kim, K. S. Kim, B. Ozyilmaz, J. H. Ahn, B. H. Hong, S. Iijima, *Nat. Nanotechnol.* **2010**, *5*, 574.

[5] X. F. Gao, L. L. Liu, S. Irle, S. Nagase, *Angew. Chem. Int. Ed.* **2010**, *49*, 3200.

[6] A. Zettl, K. Erickson, R. Erni, Z. Lee, N. Alem, W. Gannett, *Adv. Mater.* **2010**, *22*, 4467.

[7] C. Y. Su, Y. P. Xu, W. J. Zhang, J. W. Zhao, A. P. Liu, X. H. Tang, C. H. Tsai, Y. Z. Huang, L. J. Li, *ACS Nano* **2010**, *4*, 5285.

[8] Y. Y. Liang, J. Frisch, L. J. Zhi, H. Norouzi-Arasi, X. L. Feng, J. P. Rabe, N. Koch, K. Mullen, *Nanotechnology* **2009**, *20*.

[9] A. Lerf, H. Y. He, M. Forster, J. Klinowski, *J. Phys. Chem. B* **1998**, *102*, 4477.

[10] S. Stankovich, D. A. Dikin, R. D. Piner, K. A. Kohlhaas, A. Kleinhammes, Y. Jia, Y. Wu, S. T. Nguyen, R. S. Ruoff, *Carbon* **2007**, *45*, 1558.

[11] W. S. Hummers, O. R. E., *J. Am. Chem. Soc.* **1958**, *80*, 1339.

[12] C. Gomez-Navarro, J. C. Meyer, R. S. Sundaram, A. Chuvilin, S. Kurasch, M. Burghard, K. Kern, U. Kaiser, *Nano Lett.* **2010**, *10*, 1144.

[13] G. Eda, G. Fanchini, M. Chhowalla, *Nat. Nanotechnol.* **2008**, *3*, 270.

[14] D. Li, M. B. Muller, S. Gilje, R. B. Kaner, G. G. Wallace, *Nat. Nanotechnol.* **2008**, *3*, 101.

[15] X. L. Li, G. Y. Zhang, X. D. Bai, X. M. Sun, X. R. Wang, E. Wang, H. J. Dai, *Nat. Nanotechnol.* **2008**, *3*, 538.

[16] J. I. Paredes, S. Villar-Rodil, P. Solis-Fernandez, A. Martinez-Alonso, J. M. D.

Tascon, *Langmuir* **2009**, *25*, 5957.

[17]C. Y. Su, A. Y. Lu, Y. P. Xu, F. R. Chen, A. N. Khlobystov, L. J. Li, *ACS Nano* **2011**, *5*, 2332.

[18]A. B. Bourlinos, D. Gournis, D. Petridis, T. Szabo, A. Szeri, I. Dekany, *Langmuir* **2003**, *19*, 6050.

[19]G. Eda, Y. Y. Lin, C. Mattevi, H. Yamaguchi, H. A. Chen, I. S. Chen, C. W. Chen, M. Chhowalla, *Adv. Mater.* **2010**, *22*, 505.

[20]C. Gomez-Navarro, R. T. Weitz, A. M. Bittner, M. Scolari, A. Mews, M. Burghard, K. Kern, *Nano Lett.* **2007**, *7*, 3499.

[21]H. J. Shin, K. K. Kim, A. Benayad, S. M. Yoon, H. K. Park, I. S. Jung, M. H. Jin, H. K. Jeong, J. M. Kim, J. Y. Choi, Y. H. Lee, *Adv. Funct. Mater.* **2009**, *19*, 1987.

[22]G. Williams, B. Seger, P. V. Kamat, *ACS Nano* **2008**, *2*, 1487.

[23]H. Li, S. Pang, X. Feng, K. Mullen, C. Bubeck, *Chem. Commun.* **2010**, *46*, 6243.

[24]M. Zhou, Y. L. Wang, Y. M. Zhai, J. F. Zhai, W. Ren, F. A. Wang, S. J. Dong, *Chemistry-a European Journal* **2009**, *15*, 6116.

[25]K. N. Kudin, B. Ozbas, H. C. Schniepp, R. K. Prud'homme, I. A. Aksay, R. Car, *Nano Lett.* **2008**, *8*, 36.

[26]M. J. McAllister, J. L. Li, D. H. Adamson, H. C. Schniepp, A. A. Abdala, J. Liu, M. Herrera-Alonso, D. L. Milius, R. Car, R. K. Prud'homme, I. A. Aksay, *Chem. Mater.* **2007**, *19*, 4396.

[27]J. Robertson, *Materials Science & Engineering R-Reports* **2002**, *37*, 129.

[28]A. M. Nardes, M. Kemerink, M. M. de Kok, E. Vinken, K. Maturova, R. A. J. Janssen, *Org. Electron.* **2008**, *9*, 727.

[29]T. Hori, T. Shibata, V. Kittichungchit, H. Moritou, J. Sakai, H. Kubo, A. Fujii, M. Ozaki, *Thin Solid Films* **2009**, *518*, 522.

[30]L. Shen, X. D. Zhang, W. B. Guo, C. X. Liu, W. Dong, S. P. Ruan, *Optoelectronic Materials, Pts 1and 2* **2010**, *663-665*, 865.

[31]J. Xiao, Z. B. Deng, C. J. Liang, D. H. Xu, Y. Xu, D. Guo, *Physica E-Low-Dimensional Systems & Nanostructures* **2005**, *28*, 323.

[32]J. C. Wang, W. T. Weng, M. Y. Tsai, M. K. Lee, S. F. Horng, T. P. Perng, C. C. Kei,

C. C. Yu, H. F. Meng, *J. Mater. Chem.* **2010**, *20*, 862.

[33]J. H. Huang, H. Y. Wei, K. C. Huang, C. L. Chen, R. R. Wang, F. C. Chen, K. C. Ho, C. W. Chu, *Energy & Environmental Science* **2010**, *3*, 654.

[34]W. J. E. Beek, M. M. Wienk, M. Kemerink, X. N. Yang, R. A. J. Janssen, *J. Phys. Chem. B* **2005**, *109*, 9505.

[35]A. Kasry, M. A. Kuroda, G. J. Martyna, G. S. Tulevski, A. A. Bol, *ACS Nano* **2010**, *4*, 3839.

[36]K. Erickson, R. Erni, Z. Lee, N. Alem, W. Gannett, A. Zettl, *Adv. Mater.* **2010**, *22*, 4467.

[37]G. C. Wang, Z. Y. Yang, X. W. Li, C. Z. Li, *Carbon* **2005**, *43*, 2564.

[38]H. A. Becerril, J. Mao, Z. Liu, R. M. Stoltenberg, Z. Bao, Y. Chen, *ACS Nano* **2008**, *2*, 463.

[39]J. Y. Zou, H. L. Yip, S. K. Hau, A. K. Y. Jen, *Appl. Phys. Lett.* **2010**, *96*.

Chapter 3

Langmuir-Blodgett, Layer-by-layer and Filtration Methods for the Preparation of Thin Graphene Films

Up to now, most effort has been focused on the RGO films on quartz and glass substrates. To fabricate homogenous, flexible graphene films is still a challenge due to the large roughness of the polymer substrates. In this chapter, three methods will be used to deposit thin graphene films with high uniformity. The first one is the Langmuir-Blodgett (LB) assembly. By controlling the amount of the GO precursor dropped on the water surface, both monolayer and multilayer GO films can be deposited on silicon and poly(ethylene terephthalate) (PET) substrates. The second method involves the layer-by-layer (LBL) assembly followed by an in-situ photoreduction process with the assist of the photocatalytic $H_3PW_{12}O_{40}$. As an advantage of the photoreduction process, the GO film was further patterned by defining the reduction position just by using a photo mask. The third method is filtering and transfer technology towards highly conductive flexible graphene films. In this regard, an electrochemical exfoliation method was developed to synthesize high quality graphene dispersions. The as-fabricated graphene film shows a sheet resistance of 2.5 kOhm/square with a transmittance of 78 % (at 500 nm), which is comparable with that of the thermally reduced GO films. Because of the feasibility of low temperature processing, flexible graphene/metal grid hybrid electrodes were further fabricated.

3.1 Introduction

Electronic devices constructed from a monolayer graphene have been widely studied and now more attention has been directed to the development of transfer printing and solution-based methods in order to achieve large-area graphene electronic applications.[1-3] As the electronic properties highly depend on the number of graphene layers,[4-8] solution-processable methods that allow uniform and controllable deposition of thin graphene films ranging from monolayer to several layers over large areas are essential. Based on solution-processed graphene films, the electronic properties can be controlled over several orders of magnitude with low cost, making them potentially useful for flexible and transparent semiconductors or semi-metals. Up to now, solution processing of GO sheets, followed by chemical or thermal reduction is still widely used to fabricate graphene films. Although there are some traditional methods to prepare thin graphene films, such as drop casting,[9] dip coating,[10] and spin coating,[11] they are not effective for controlling the number of deposited GO layers. In this chapter, LB assembly, layer-by-layer deposition will be conducted to prepare thin GO and RGO films on various substrates such as quartz, silicon wafers and PET. The FET devices based on the as-fabricated RGO films exhibit reproducible performance due to their highly uniform morphologies. Finally, in view of conductivity, high quality graphene dispersions prepared by an electrochemical exfoliation method were used to replace GO to directly deposit conductive graphene films on PET substrates. Because of the low content of oxygen containing groups, the electrochemically exfoliated graphene (ECEG) is conductive and also dispersible very well in DMF solution. Based on such graphene dispersions, highly conductive graphene films were prepared on PET substrates by a vacuum filtering/transfer process, with the conductivity already comparable to that of the thermally reduced GO films. To further reduce the resistance, metal grids were introduced to form flexible graphene/metal grid hybrid electrodes, resulting in a sheet resistance of < 200 Ohm/square with a transmittance of ~ 70 %.

3.2 Langmuir-Blodgett assembly

It has been proved that LB assembly is an efficient approach to assemble monolayer organic molecules on water surfaces followed by dip-coating to transfer the monolayers on arbitrary substrates.[12-17] In general, the organic molecules should be water insoluble.[18-22] However, in GO sheets, the oxygen-containing groups are decorated on the hexagonal carbon network and as a consequence it features macromolecular surfactant properties with hydrophobic and hydrophilic components. Although GO sheets are water soluble, once the GO sheets float on the water surface, they will be more stable. Additionally, the edge-to-edge repulsion between each GO sheet caused by electrostatic forces prevents them from aggregation during the compressing of the barriers.[23]

The selection of the solvents is the most essential issue for the assembly of GO sheets on a water surface. The widely used water-immiscible solvents, such as chloroform and toluene, are impossible because of the poor solubility of GO sheets in them. It is well known that GO sheets are only soluble in highly polar solvents like H_2O, DMF, NMP and ethylene glycol, which are also unfeasible to act as the spreading (assembly) solvent because of their low spreading ability on water surface. It is interesting that low surface tension solvents, such as ethanol, methanol and acetone, can spread very quickly after dropping on a water surface. Thus, in our experiments, a mixture of methanol/H_2O (5/1) was applied as the solvent of GO sheets for the LB assembly. It was found that the GO sheets (0.01-0.1 mg/mL) in the methanol/H_2O solution can be stable for several months.

In a typical experiment, the GO sheets were with narrow size distribution were obtained by a density gradient ultracentrifugation. Firstly, the GO dispersion was centrifuged at 8000 rpm for 10 min to collect the solid by removing the top layer solution. Subsequently, the solid was re-dispersed and then centrifuged at 4000 rpm for 10 min to remove the large-sized, unexfoliated and aggregated ones, forming the dispersion with the GO size of ~ 1-2 μm (Figure 3.2). The purified GO sheets were dissolved in a mixture of methanol/H_2O (5/1) to form a stable dispersion with a concentration of 0.01 mg/mL. It is noteworthy that such a GO dispersion is stable for several months. Afterwards, the GO dispersion was slowly dropped on the water surface. Usually a faint brown color could be observed. The GO layer was then stabilized for about 15 min and then the LB assembled GO film was transferred on the target substrates.

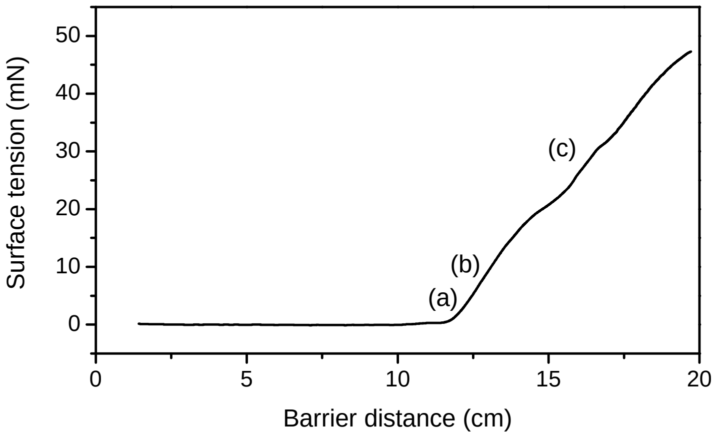

Figure 3.1 Recording surface tension along with the barriers moving.

During the compression of the barriers, the surface tension was monitored by a tension meter attached to the LB machine. A gradual increase of the surface tension was recorded as shown in the isothermal surface tension area plot in Figure 3.1. As the GO film was compressed, slight darkening of the film color was observed, which is consistent with increased material density on the water surface. In our experiment, there was no change of the surface tension until the barrier reaches the position of 12 cm. After that, the surface tension suddenly increases. The corresponding AFM images of the LB assembled GO films at the surface tension of 3 mN, 10 mN, and 30 mN are displayed in Figure 3.2. Thus the increase of the surface tension is due to the contact and repulsion of GO sheets. The morphology of the LB assembled GO film formed at a surface tension of 3 mN is displaced in Figure 3.2(a) with a calculated coverage density of GO sheets of 72 %. The presence of the large blank areas is attributed to the fact that the morphology of GO sheets is not regular and the movement of the GO sheets is not fast enough. To further compress the barriers to a surface tension of 10 mN, the coverage density of the GO film increases to 94 % and the large blank areas disappears. Additionally, there are some wrinkled structures on the overlapped GO sheets (Figure 3.2b). At a surface tension of 30 mN, the coverage density of GO film increases to 98 %, with obvious overlapping at the GO edges and a large amount of wrinkled structures (Figure 3.2c). It is interesting that, even under a very high pressure, the center areas of GO sheets still remain flat.

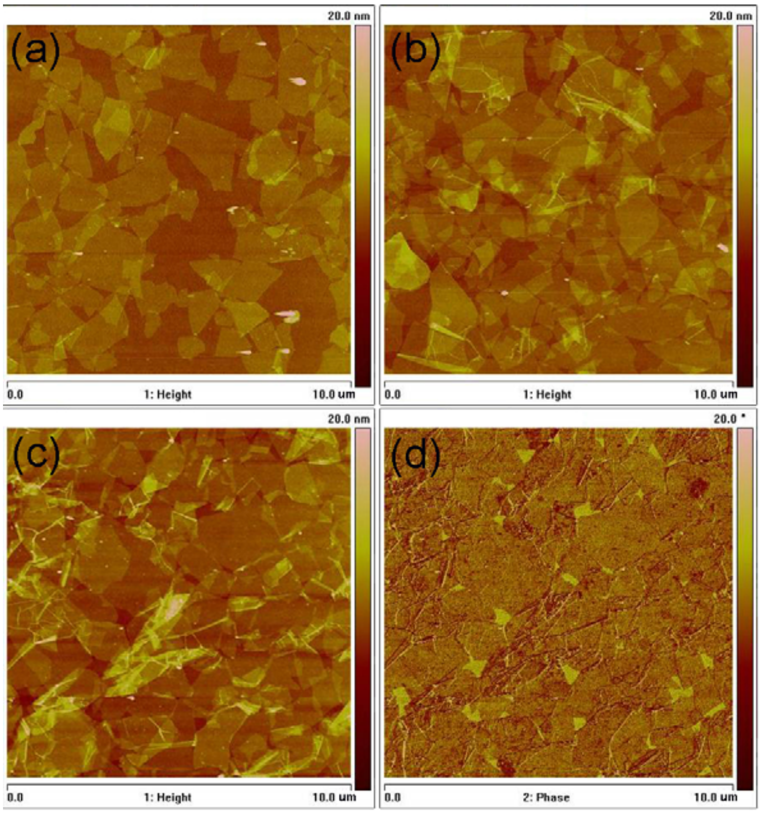

Figure 3.2 (a,b,c) AFM images of the LB assembled GO single layers dip coated at different regions of the isotherm in Figure 3.1. (a) 3 mN, (b) 10 mN, (c) 30 mN, (d) Phase image of the (c), indicates that ~ 98 % of the surface is covered by GO sheets.

The trough surface area is 864 cm^2 (57.6 cm × 15 cm), and the effective water surface area is about 720 cm^2. To assemble a monolayer GO film in such a large area, 12 mL GO dispersion with the concentration of 0.01 mg/mL is required. It was found that the concentration of GO dispersion should be less than 0.02 mg/mL for the assembly of monolayer GO film. Higher concentrated GO dispersion would yield double or multilayer GO sheets films because the low spreading efficiency of the methanol/H_2O (which will be discussed in Scheme 3.1).

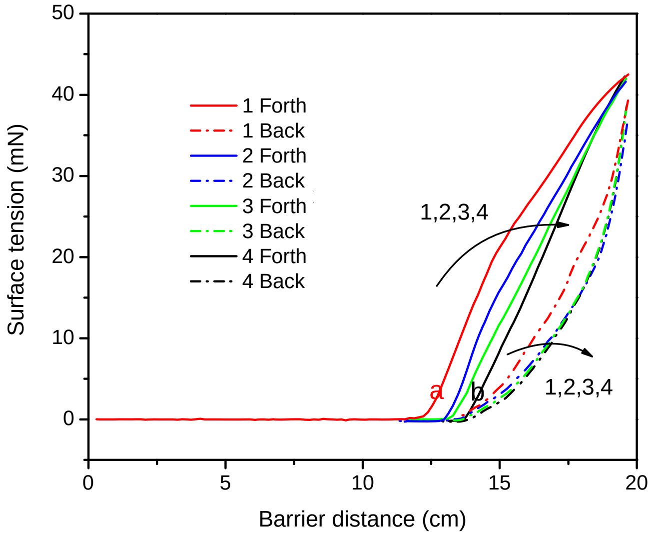

Figure 3.3 Isotherm plots of four sequential compression-expansion cycles, showing GO sheets monolayer is reversible and stable against compression.

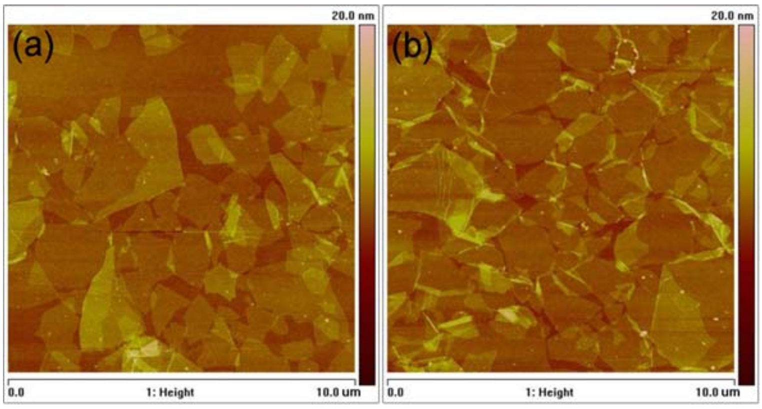

Figure 3.4 AFM images of the LB assembled GO single layers dip coated at 3 mN in the first (a) and fourth (b) forward cycle, respectively.

To study the assembly behavior of GO sheets on a water surface, the surface tension was recorded during repeating the compression-expansion cycle for 4 times as shown in Figure 3.3. The surface tension increased slowly during the comparison of the barriers, while the surface tension decreased fast when the barriers are expanding (Figure 3.3). The hysteresis of the back curves is attributed to the slow diffusion speed of GO sheets on water surface for its large size. Additionally, it is also possible that some folded and overlapped structures can not be re-separated again after the barriers are expanded. In the forth curves (1,2,3,4, real line), the surface tensions at the barrier distance of ~ 20 cm are almost the same, indicating that there are no GO sheets dissolving into the water solution during compressing and expanding the barriers. In the first cycle, the surface tension starts to increase at the barrier position of 12 cm, while in the forth cycle, this position shifts to 14 cm. Figure 3.4(a) and (b) are the AFM images of the GO films dip-coated at the same surface tension of 3 mN in the first and fourth cycles, respectively. Although the GO films were dip coated at the same surface tension, the density of the GO sheets was very different. In the first cycle, the GO film (Figure 3.4a) exhibits low coverage density (~ 70 %) with large blank area, while in the fourth cycle, the coverage density of GO sheets reaches ~ 96 % (Figure 3.4b). It therefore can be concluded that the shift of position form 12 cm to 14 cm is because of the rearrangement of the GO sheets.

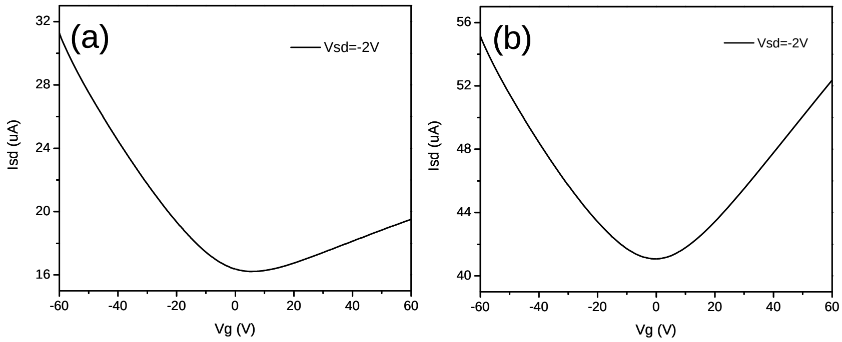

Figure 3.5 $I_{sd} - V_g$ curves of the FET devices fabricated on a thermally reduced LB assembled GO film. (a) before annealing, (b) after thermal annealing at 300 ^{o}C for 30 min to remove the extra molecules absorbed on its surface. The measurements were carried out in a nitrogen filled glove box.

In order to evaluate the electronic properties of the LB assembled graphene film, the monolayer GO film was firstly dip-coated on a pre-cleaned silicon substrate with a 300 nm thick SiO_2 layer followed by a thermal reduction at 800 ^oC for 30 min under an argon flow. Then 60 nm thick Au electrodes with a channel length of 25 μm and a channel width of 290 μm were thermally evaporated on the RGO films as source and drain electrodes through 300 mesh copper grids. The FET measurements were carried out in a nitrogen filled glove box with a Keithley SCS 4200 semiconductor characterization system. Figure 3.5 (a) presents the transfer characteristic of the RGO film at a source-drain bias of V_{sd} = -2 V. The I_{sd}-V_g curve exhibits ambipolar field effect with the on/off ratio of ~ 2, which is similar to the previous studies.[9, 24] Electron and hole mobilities were extracted from the linear regime of the transfer characteristics, using the equation $\mu = [(\Delta I_{sd}/\Delta V_g)/(L/W)]/C_{ox}V_{sd}$,[7] where L and W are the channel length and width, C_{ox} is the capacitance of silicon oxide dielectric layer (which is 1.27×10^{-8} F/cm^2 for 300 nm thick silicon oxide), V_{sd} is the source-drain voltage, which is -2 V in the present work, I_{sd} is the source-drain current, and V_g is the gate voltage. $\Delta I_{sd}/\Delta V_g$ is the transconductance or the slope of the transfer curve in the linear regime. From the I_{sd}-V_g curves measured in the glove-box before thermal annealing as shown in Figure 3.5(a), with the calculated hole mobility of about 1.15 cm^{2}V^{-1}S^{-1}, while the electron mobility of 0.23 cm^{2}V^{-1}S^{-1}. Subsequently, the electron mobility was enhanced to 0.82 cm^{2}V^{-1}S^{-1} via annealing the sample at 300 ^oC for 30 min the glove box, while the hole mobility was almost unchanged (Figure 3.5b). It can be concluded that the relatively low electron mobility before annealing is due to the presence of the electron trapping molecules on the RGO surface, such as H_2O and O_2. It was the fact that, after putting the sample into air for 1 h again, the electron mobility was decreased to ~ 0.23 cm^{2}V^{-1}S^{-1}, which means that the adsorption/desorption of small molecules is reversible. More than 20 devices were tested and all the FETs shown similar transfer curves, which strongly indicates the advantages of the LB technology in the fabrication of the thin GO film with high uniformity.

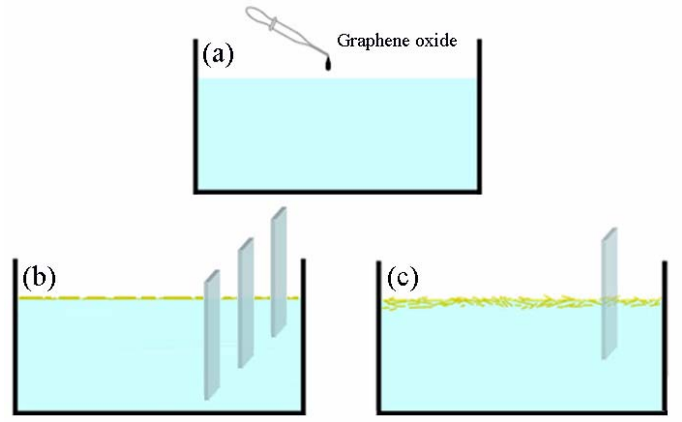

Scheme 3.1 Schematic illustration of dip-coating multilayer GO films via repeating dip-coating monolayer GO films (b) and one-step dip-coating multilayer GO films (c).

However, to be used as transparent electrodes, multilayer graphene films are required to provide a low electrical resistance. Based on the LB assembly, two strategies have been studied. One is to repeat the dip-coating of monolayer GO films to form multilayer films as illustrated in Scheme 3.1 (b). The other one is to directly assemble multilayer GO films on a water surface by controlling the concentration of the GO dispersion dropped on a water surface and then dip-coating on arbitrary substrates (Scheme 3.1c).

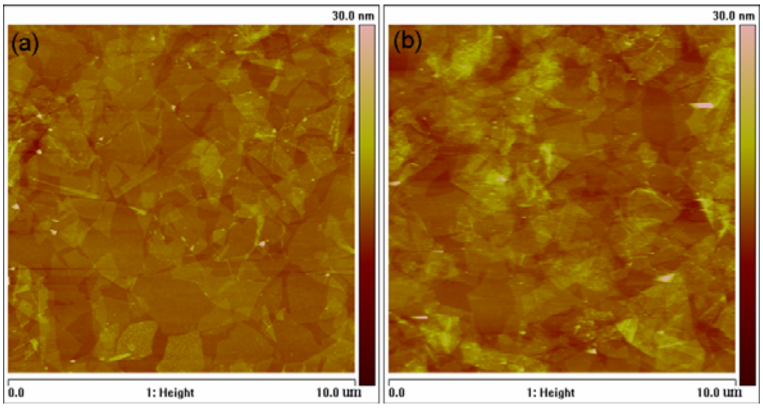

Figure 3.6 AFM images of the LB assembled GO films obtained via twice dip-coating (a) and three times dip-coating (b) at a surface tension of 10 mN.

In principle, a multilayer GO film can be dip-coated on various substrates by repeating the dip-coating of monolayer GO films. It was found that the adhesion between GO films and the glass (or quartz, silicon, PET) substrate was very strong and the former GO layer could not be dissolved when we performed the subsequent dip-coating. Figure 3.6(a) and (b) are the AFM images of GO films after two and three times dip-coating at a surface tension of 10 mN, respectively. As shown in Figure 3.6(a), the second layer GO film is not as homogenous as the first one, which is possibly caused by the bad compatibility of the underlayer GO film due to their negative charge. It is also obvious that the newly deposited layer tends to show a wrinkled morphology. After three times dip-coating, the GO film became much rougher than double layer GO film (Figure 3.6b)

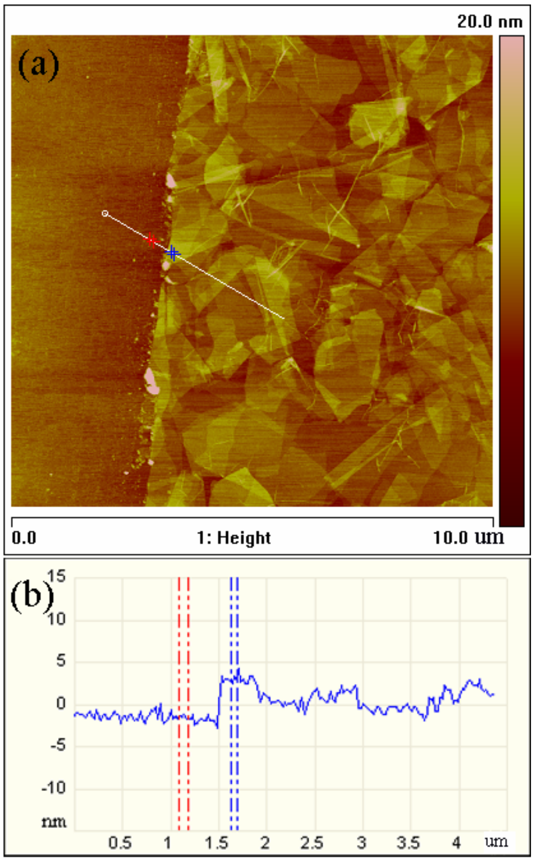

Figure 3.7 One-step preparation of multilayer GO film by the LB technology by controlling the concentration of the GO dispersion.

It is clear that repeating the dip-coating of monolayer GO sheets is not an effective method to prepare homogenous GO films. As aforementioned, to assemble a monolayer GO film, the concentration of GO dispersion (methanol/H_2O) should be less than 0.02 mg/mL. Otherwise, multilayer GO films will be assembled on the water surface. Figure 3.7 is the AFM image and height profile of a GO film obtained by dropping 3 mL 0.1 mg/mL GO dispersion on a water surface followed by dip-coating on silicon substrate at a surface tension of 2 mN. The thickness of the film is about 5 nm, corresponding to ~ 4 layer GO sheets. It is more uniform than the GO films fabricated by the above mentioned repeating the dip-coating cycles (Figure 3.6). It is noteworthy that the multilayer GO sheets on the water surface are not as stable as the monolayer ones. It was found that underlayer GO sheets could be slowly dissolved into the water until only one layer GO was left on the water surface. Therefore, the multilayer films should be dip-coated in less than 2 h after dropping GO solution on the water surface.

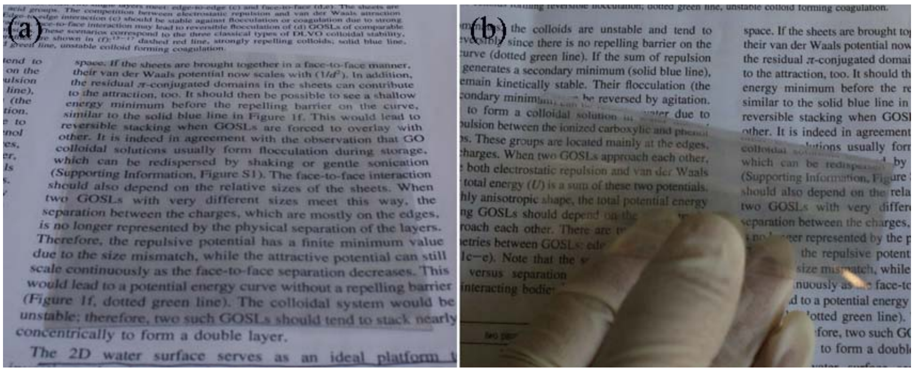

Figure 3.8 OM images of the RGO film prepared by one-step dip coating on PEF substrate and followed by chemical reduction in N_2H_4 vapor.

To deposit a homogenous multilayer GO film on flexible PET substrates, the substrates were firstly treated with a short time (10-30 s) oxygen plasma treatment to produce a hydrophilic surface. Then the LB assembled multilayer GO film was easily transferred on such PET substrate. The reduction of the assembled GO film was carried out in the N_2H_4 vapor at room temperature for 5 h, resulting in a conductivity of ~ 5 S/cm. Figure 3.8 present the OM images of a ~ 5 nm thick flexible RGO film (10 cm ×10 cm). This film has a pronounced stretching property, and the conductivity remains unchanged after bending the PET substrate for 20 times.

3.3 Layer-by-layer assembly

For the films fabricated by the LB assembly, a post chemical reduction or thermal reduction is required to restore the conductivity. One of the disadvantages is the aforementioned chemical reduction is the use of toxic agents. For GO films prepared on polymer substrates, the thermal reduction is unfeasible because of the low decomposing temperature of the substrates. In this section, photoreduction was introduced to reduced GO films. Recently, inorganic metal oxides (e.g. titanium oxide) have been utilized as photocatalyst to produce RGO sheets from GO via a UV-assisted photoreduction.[25-27] Compared with conventional chemical reduction methods, the photoreduction of GO is "green" and easy to perform by a UV-irradiation.[28] Like TiO_2, polyoxometalates (POMs) can also be used as the photocatalysts. PW12 (abbreviation of $H_3PW_{12}O_{40}$) is one of the POMs family, and its reduction mechanism of GO is illustrated in Scheme 3.2.

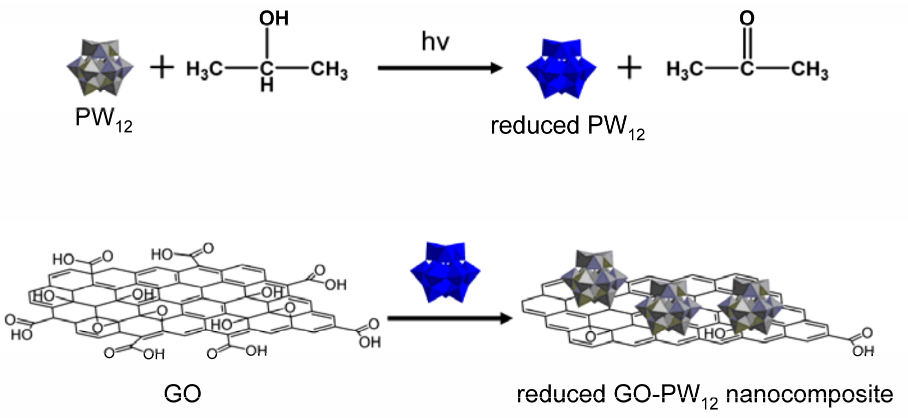

Scheme 3.2 Mechanism of the $H_3PW_{12}O_{40}$ assisted photoreduction of graphene oxide.

When an aqueous solution containing GO, PW$_{12}$ and isopropanol is irradiated by UV light, the PW12 is firstly photoreduced accompanied by the oxidation of isopropanol. Subsequently, GO is reduced by the photoreduced PW12. Although PW12 can adsorb on the RGO sheets as anionic stabilizer after the photoreduction, the stability of the photoreduced GO is not as excellent as that of GO, which makes the preparation of homogenous films problematic from such a precursor. Thus we propose the LBL approach to first deposit the composite film of GO and PW12 and then reduce them under the UV light (Scheme 3.3). This post photoreduction strategy gave more flexibility to control the device fabrication. In our experiments, a cationic polyelectrolyte poly(allylamine hydrochloride) (PAH) was used to combine the GO sheets and PW12 together. The study of the layer-by-layer assembly was performed jointly with Dr. Haolong Li. The target of this part is to fabricate homogenous graphene films reduced by the photoreduction.

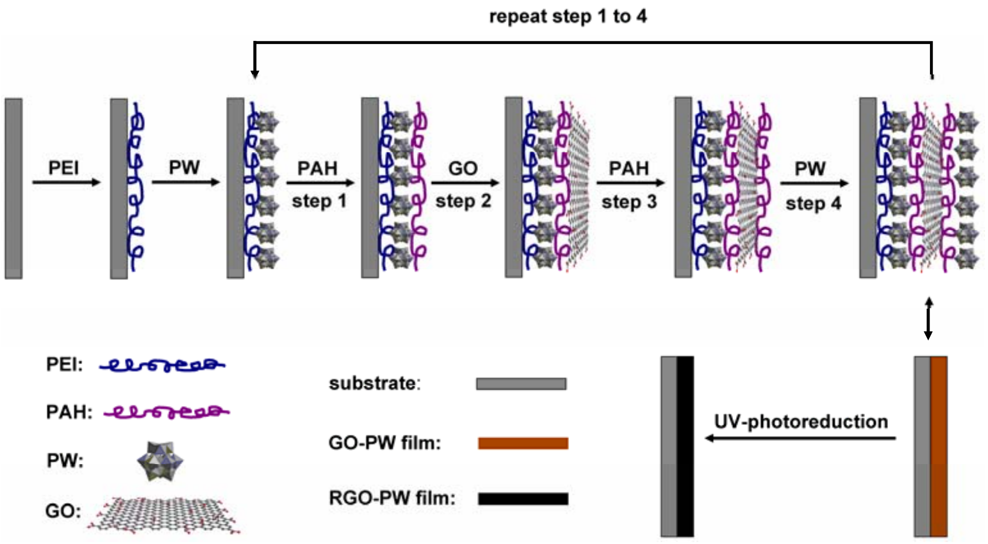

Scheme 3.3 Schematic illustration of the fabrication procedure of RGO-PW12 multilayer films, which involves the LBL assembly of GO nanosheets and PW12 clusters using cationic polyelectrolytes as electrostatic linkers, and a subsequent in-situ photoreduction to convert GO to RGO. (poly(ethyleneimine) = PEI, MW 50 000, poly(allylamine hydrochloride) = PAH, MW 15 000)

The fabrication procedure of GO-PW12 multilayer films is shown in Scheme 3.3. A pre-cleaned substrate was firstly immersed into a 2.5 mg/mL PEI solution for 15 min, rinsed by dipping the substrate twice in deionized water solutions for 1 min, and dried with a gentle flow of nitrogen. Then, the PEI coated substrate was immersed in a 1 mg/mL PW12 solution for 15 min, followed by the same rinsing and drying procedures as above. After that, a PEI/PW12 double layer was adsorbed on the substrate and then used as a precursor film to construct the GO-PW12 multilayer. The precursor film was immersed in a 2 mg/mL PAH solution for 15 min (step 1), followed by an alternating 20 min immersion in a 0.3 mg/mL GO water solution (step 2). The GO coated substrate was immersed in a PAH solution for 15 min (step 3) and then immersed in a 1 mg/mL PW12 solution for 15 min (step 4). Water rinsing and nitrogen drying steps were performed after each adsorption step. After repeating the cycle from step 1 to step 4, a multilayer film with the structure of $(PAH/GOPAH/PW12)_n$ was deposited on the PEI/PW12 precursor film. The cycles were repeated until the desired layer number n was obtained. Photoreduction of GO-PW12 films and fabrication of reduced patterns were carried out via exposing the substrates coated by GO-PW12 films to 100 W high pressure mercury lamp equipped with a WG280 filter.

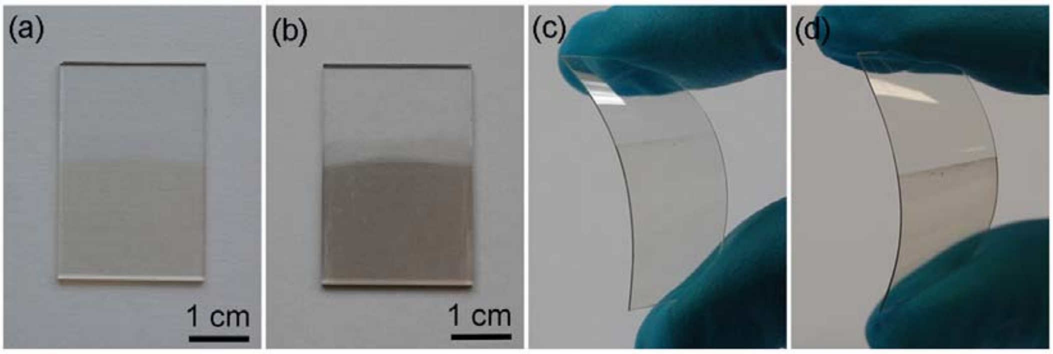

Figure 3.9 Optical images of a $(PAH/GO/PAH/PW12)_6$ multilayer film prepared on a quartz substrate before (a) and after (b) 6 hour UV-photoreduction, and on a flexible PET substrate before (c) and after (d) 6 hour UV-photoreduction. Both

substrates are modified by a PET/PW12 precursor film.

By using the LBL assembly method mentioned above, the GO-PW12 multilayer films can be fabricated on different hydrophilic substrates, such as quartz substrates and oxygen plasma treated flexible PET substrates, as shown in Figure 3.9(a) and 3.9(c). Furthermore, in the film structure of PEI/PW12-(PAH/GO/PAH/PW12)$_n$, PW12 layers exist on the both sides of GO layers, which provide a suitable condition to employ the PW12-assisted photoreduction process to reduce GO layers. To carry out the photoreduction, the as-prepared GO-PW12 multilayer films on different substrates were irradiated by a 100 W high pressure mercury lamp to oxidize the organic polyelectrolytes and to reduce the GO nanosheets via the photocatalytic activity of the PW12 clusters.*[26]* The color of the films gradually turned from light brown to dark grey (Figure 3.9b and 3.9d), which indicates the formation of reduced GO.

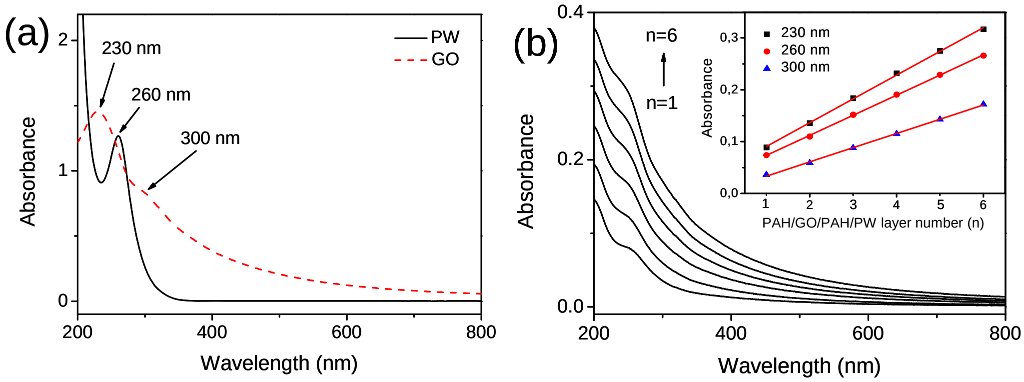

Figure 3.10 (a) UV-vis absorption spectra of an aqueous 0.05 mgmL^{-1} PW12 solution (black line, PW12 concentration is 1.7×10^{-5} M) and an aqueous 0.05 mg/mL GO solution (red line). (b) UV-vis absorption spectra of a LBL assembled (PAH/GO/PAH/PW12)$_n$ multilayer film with layer number n = 1–6 on a PEI/PW12-modified quartz substrate as the precursor film. The curves, from bottom to top, correspond to n = 1, 2, 3, 4, 5, and 6, respectively. Inset shows the plots of the absorbance values at 230, 260, 300 nm as a function of the layer number n.

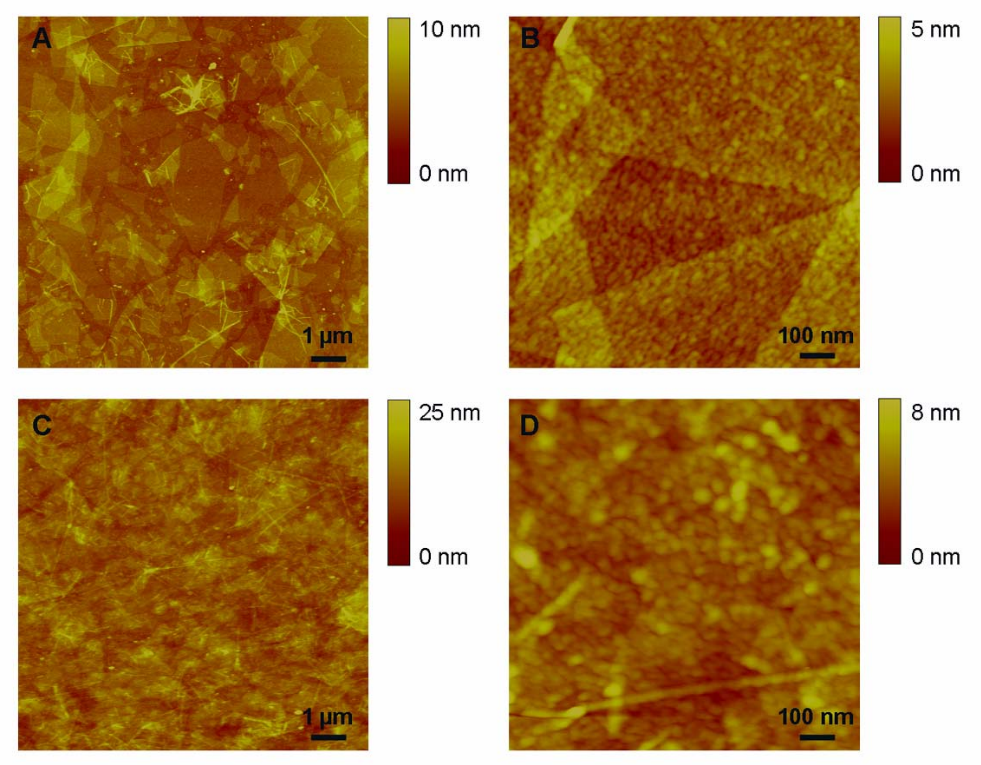

Figure 3.11 AFM images of a $(PAH/GO/PAH/PW12)_1$ film (a,b) a $(PAH/GO/PAH/PW12)_6$ film (c,d)

GO and PW12 both show characteristic absorptions in the UV-vis region, as shown in Figure 3.10(a). Two absorption bands of GO appear at 230 nm and 300 nm, while the well-known ligand-to-metal charge transfer (LMCT) transition band of PW12 appears at 260 nm. Therefore, it is easy to monitor the formation of GO-PW12 multilayer films by UV-vis spectroscopy, according to the increased intensity of the film absorbance at the characteristic absorption bands of GO and PW12. Figure 3.10(b) displays the UV-vis absorption spectra of $(PAH/GO/PAH/PW12)_n$ multilayer films (with n = 1−6) assembled on a PEI/PW12 precursor film on quartz substrates. The absorption of the films gradually increased with the layer number n, which gives evidence of the continuous deposition of GO and PW12 components. When monitoring the detailed absorption variation during a PAH/GO/PAH/PW12 assembly process, we found that the absorbance of films increases after the deposition processes of both GO and PW12, which means that the two parts are indeed assembled into the films. PAH does not absorb above 200 nm, and therefore its presence on the films is not reflected in the absorption spectra. The absorbance values for $(PAH/GO/PAH/PW12)_n$ multilayer films with n = 1−6 at 230, 260, and 300 nm are plotted as function of the layer number n, as shown in the inset of Figure 3.10(b). The absorbance varies linearly with n at all three wavelengths, which reveals a constant increase in the total amount of GO and PW12 adsorbed in the films after each deposition cycle of PAH/GO/PAH/PW12 layer.

The AFM image of a $(PAH/GO/PAH/PW12)_1$ film on silicon substrate shows that the film is covered by a monolayer of GO nanosheets with a high surface coverage density, although some nanosheets overlap at the edge regions, as shown in Figure 3.11(a). The root-mean-square deviation of the surface roughness (R_q) for the whole 10 × 10 μm^2 area of Figure 3.11(a) is only 1.17 nm. In the magnified AFM image of $(PAH/GO/PAH/PW12)_1$ film (Figure 3.11b), small particles with the size of several nanometers are found existing on the surface of GO nanosheets. The particles should be the aggregates of PW12 clusters that were entrapped by PAH chains. A similar phenomenon has also been observed in the LBL assembled multilayer films based on other polyoxometalates and polyelectrolytes.[29] Moreover, the R_q value of the 1 × 1 μm^2 area in Figure 3.11(b) is only 0.59 nm, further confirming the smooth surface of the $(PAH/GO/PAH/PW12)_1$ film. On the other hand, the AFM images of the $(PAH/GO/PAH/PW12)_6$ films show a tight stacking morphology of multilayer GO nanosheets, as revealed in Figure 3.11(c,d). Likewise, the film is smooth and uniform. The R_q values of the 10 × 10 μm^2 area in Figure 3.11(c) and the 1 × 1 μm^2 area in Figure 3.11(d) are 2.46 nm and 0.90 nm, respectively, which is about twice the value R_q of $(PAH/GO/PAH/PW12)_1$ film. Meanwhile, the PW12 aggregates in the film become larger, ~ 20 to 30 nm (Figure 3.11d). The increased roughness is often seen for the first few layers in LBL assembled multilayer film, which is attributed to a substrate effect.[29]

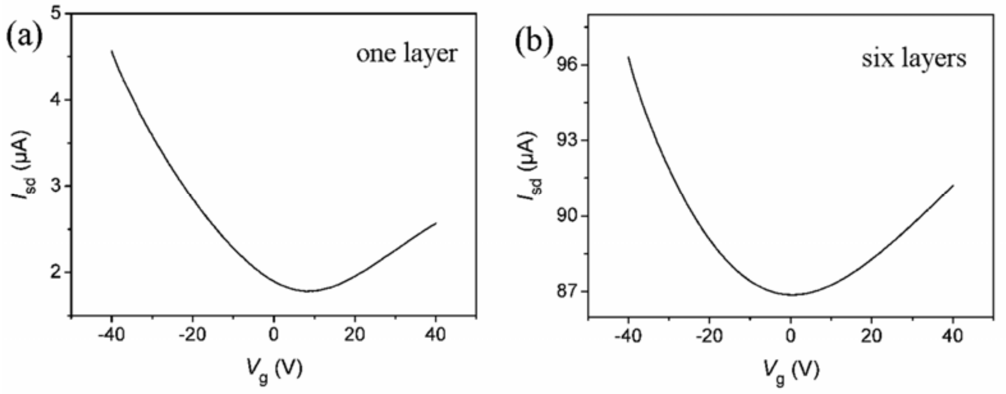

Figure 3.12 I_{sd}-V_g curves of the FET devices fabricated on a $(PAH/GO/PAH/PW12)_1$ film (a) and a $(PAH/GO/PAH/PW12)_6$ film (b). Both samples are prepared on PEI/PW12 precursor film modified silicon substrates with 300 nm thick SiO_2 and have been reduced via 6 hour UV-photoreduction process. V_{sd} is 10 V.

To investigate the transport characteristics of the RGO-PW12 films, FET devices based on the photoreduced graphene film with different thickness were fabricated. Both films were prepared on the silicon substrates with 300 nm thick SiO_2 layer. Au electrodes with the channel length of 20 μm and the channel width of 400 μm were thermally evaporated on the films as source and drain electrodes. The I_{sd}-V_g curves of the FET devices both exhibit an ambipolar field effect (Figure 3.12). The on/off ratio of the $(PAH/GO/PAH/PW12)_1$ film device is > 2 and that of the $(PAH/GO/PAH/PW12)_6$ film device is only 1.1. From the I_{sd}-V_g curves in Figure 3.12, we derived the hole and electron mobility values of 0.03 and 0.01 $cm^2V^{-1}S^{-1}$ for the $(PAH/GO/PAH/PW12)_1$ film device, 0.15 and 0.06 $cm^2V^{-1}S^{-1}$ for the $(PAH/GO/PAH/PW12)_6$ film device, which are comparable to the RGO film based FET devices produced by chemical reduction.[1, 30, 31] The above results suggest that the thicker film device has a higher mobility but a lower on/off ratio. Considering the thickness of RGO-PW12 film can be easily controlled by the LBL assembly process, the transport properties of the RGO-PW12 film based FET devices can be easily tailored.

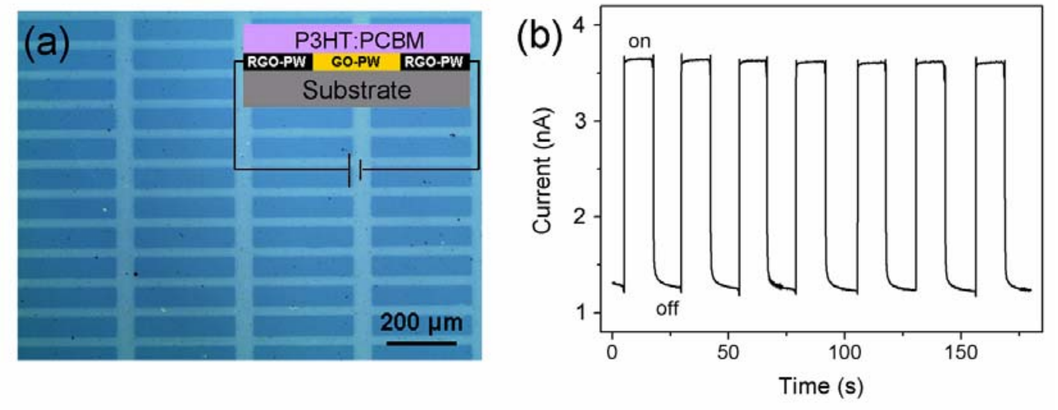

Figure 3.13 (a) Optical microscopy images of reduced patterns on (PAH/GO/PAH/PW12)$_6$ multilayer films on silicon substrates with 300 nm thick SiO$_2$. The patterns are made by 6 hour UV-photoreduction using different photomasks. (b) The photocurrent response of a photodetector based on the conductive patterns on (PAH/GO/PAH/PW12)$_6$ films versus time under chopped irradiation, under a bias voltage of 10 V. The inset in Figure 3.13(a) is the schematic illustration of the photodetector using conductive patterns of RGO-PW12 film as microelectrodes.

The conductivity of photoreduced RGO-PW12 films is greatly increased in comparison with the initial insulating GO-PW12 films. After 6 hour photoreduction, the conductivity values of (PAH/GO/PAH/PW12)$_1$ films and (PAH/GO/PAH/PW12)$_1$ films are ~ 20 S/m and 150 S/m, respectively. These values are comparable to those of the RGO films reduced by chemical methods.[32, 33] To take advantage of the increased conductivity of RGO-PW12 films, we explored applications of the films as electrode materials in optoelectronic devices. A photoreduction lithography method was employed to pattern the conductive RGO-PW12 domains on the insulting GO-PW12 films,[28] in which 300 mesh copper grids were placed on the films to realize a selected-area effect of UV-irradiation. By this method, well-ordered conductive patterns on a micrometer scale were successfully constructed on the films, as shown in Figure 3.13(a). Subsequently, the conductive patterns were used as microelectrodes for a photodetector device, via spin coating a thin film of P3HT/PCBM mixture as the typical photoswitching materials (Figure 3.5a). The detector is composed of two adjacent patterns and P3HT/PCBM film bridged between them. The photoswitching properties of the as-fabricated photodetector based on the conductive patterns on $(PAH/GO/PAH/PW12)_6$ films are investigated. The device shows a well repeatable photocurrent response with the on/off ratio of ~ 3, under the switching stimulus of external light source (Figure 3.13a). However, the P3HT/PCBM film on the non-patterned region did not show any response. Although several methods have been reported for the fabrication of RGO film based microelectrodes, they normally involve two steps: the reduction of GO film and the fabrication of patterns. Therefore, it is obvious that the present photoreduction lithography method combines the two steps into one.

3.4 Filter and transfer

In view of the recovery of the conductivity of the GO films, both the aforementioned chemical reduction and photoreduction are not efficient enough. For instance, the conductivity of the chemically reduced LB assembled GO film is ~ 5 S/cm (Figure 3.8), while that of the photoreduced layer-by-layer assembled six layer GO film is 1.5 S/cm (Figure 3.11). These values are much lower than the RGO film prepared by the thermal reduction (~ 500-1000 S/cm). Thus, it is still a challenge to prepare highly conductive graphene films without high temperature treatment.

It is thought that the use of high quality graphene dispersion to replace GO as the precursor for the graphene film fabrication is the most efficient approach to synthesis highly conductive graphene films. To directly exfoliate high quality graphene sheets from the natural graphite flakes is a very promising due to the feasibility of low-cost large-scale preparation. Expanded graphite has been previously prepared by the chemical intercalation of formic acid or sulphuric acid followed by fast heating, in which the graphite is violently expanded by gaseous species released from the intercalants.[34, 35] However, the majority of the exfoliated graphite flakes remain relatively thick (~ 10 to 100 nm in thickness). Although the exfoliation of the graphene has been improved by employing oleum as the re-intercalation agent and tetrabutylammonium hydroxide as the expanding agent based on the expanded graphite, the yield of monolayer graphene is too low for practical applications.[36] Recently, it has been reported that the electrochemical exfoliation of graphite in sulphuric acid may serve as an efficient approach to synthesize high-quality, cost-effective graphene with scalable production.[37] Because of a low level content of oxygen containing groups, we name it as ECEG (electrochemically exfoliated graphene) for short to be distinguished from pristine graphene.

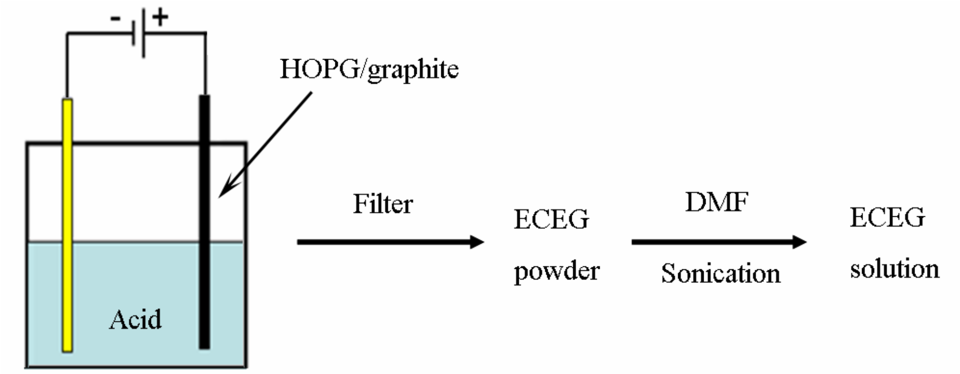

Scheme 3.4 Schematic illustration of the fabrication of ECEG.

Scheme 3.4 illustrates the experimental set-up and the fabrication process, where natural graphite flake or HOPG was employed as an electrode and graphene source for the electrochemical exfoliation. A grounded Pt wire was placed parallel to the graphite flakes with a separation of 3 cm. We found that H_2SO_4 is the most efficient intercalant to exfoliate graphite comparing to HCl, HNO_3 and NH_4OH. In a typical experiment, 1 wt.% H_2SO_4 was used as an electrolyte, the static bias of +1 V was first applied to the graphite for 2 min, followed by applying a bias of +10 V till all of the graphite flakes were dissociated. The initial low bias wetting of the sample could produce gentle intercalation of the SO_4^{2-} ions into the interlayer spacing of graphite (Figure 3.14). Before applying a high bias, the graphite remained as single piece, but with a light exfoliation on the edges. Once a high bias was applied, the graphite was quickly exfoliated and spread into the H_2SO_4 solution. The exfoliated graphite was collected with a Teflon filter and washed with water by vacuum filtration. After drying, the sample was dispersed in DMF by gentle sonication for 30 min at 0 °C. It was found that the role of the sonication treatment is to further exfoliate some thick flakes to thinner ones. After keeping the ECEG dispersion for 1 day, there were still more than 50 % graphene sheets stable in the solution. The top solution was used for the film preparation.

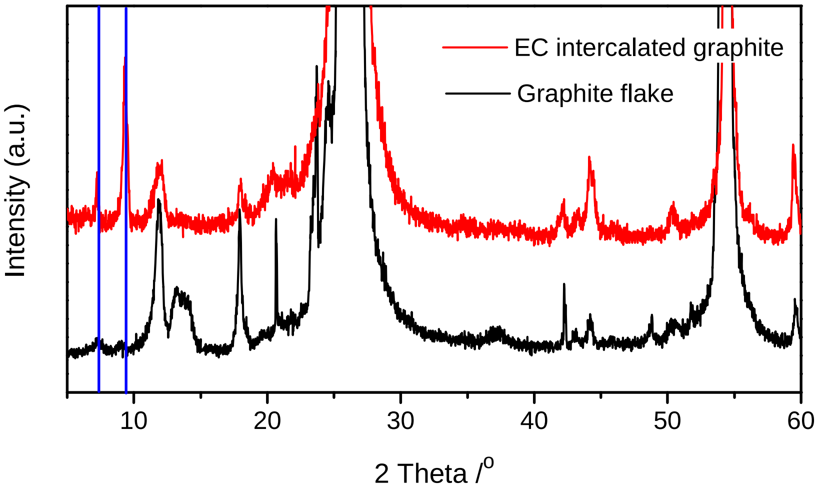

Figure 3.14 X-ray diffractions of natural graphite flakes (black) and electrochemically intercalated graphite at low voltage (+1 V).

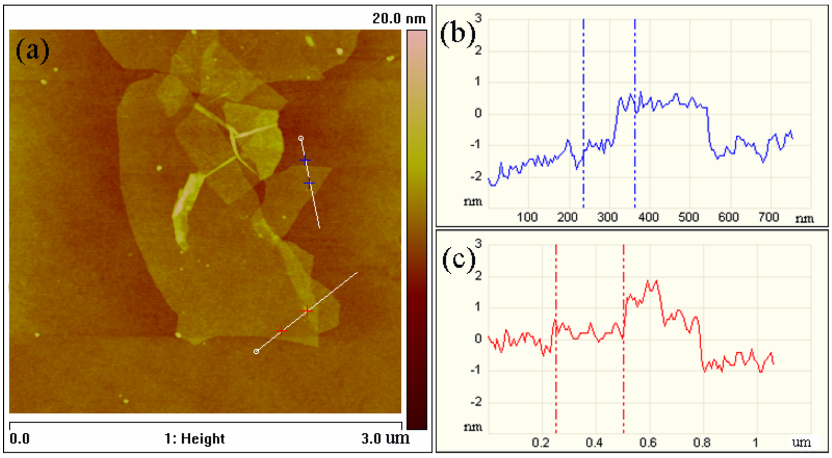

Figure 3.15 (a) AFM image and (b,c) Height profiles of a ECEG on silicon substrate.

The intercalation of H_2SO_4 into the interspacing of graphite layers at the low bias (+1 V) was verified by XRD measurements (Figure 3.14). The main change is observed in the small angle region of 5^o to 10^o. Two peaks at around 7.5^o and 9.5^o appear after intercalation, indicating the occurring of the intercalation.

Figure 3.15(a) is the AFM image of the ECEG sheets on the silicon substrate prepared by dip-coating. The size of the ECEG is ~ 1 μm and the thickness ranges from 1 to 1.5 nm. It is worth noting that the thickness of ECEG shown in AFM highly depends on the underlayer substrate, showing ~ 1.5 nm on silicon substrate (Figure 3.15b) and only 1 nm on another graphene sheet (Figure 3.15c). It was calculated from the AFM images (no shown here) that the content of the graphene sheets with the thickness ≤ 1.5 nm is about 20 %, and others are about 2-5 nm. Therefore, both of the exfoliation and the purification process need to be optimized in order to increase the yield and the thin layer graphene.

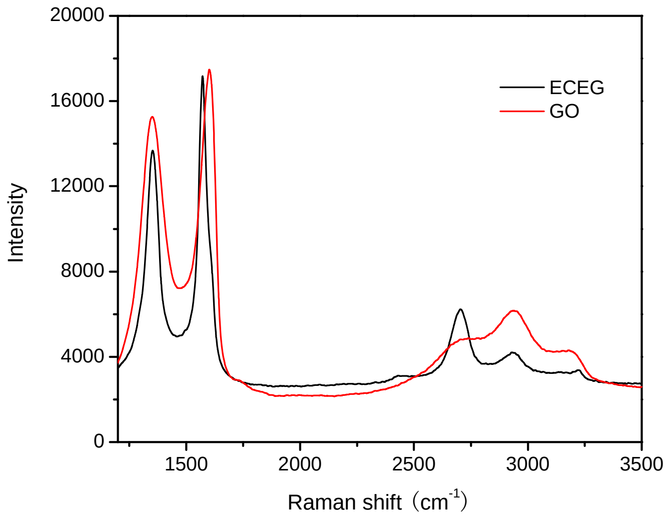

Figure 3.16 Raman spectra for the ECEG and GO films. The ECEG film was fabricated by the filter/transfer method, while the GO film was prepared by spin-coating.

The quality of the ECEG was examined by Raman spectroscopy, which were measured on ~ 5 nm thick films prepared from the as-synthesized ECEG dispersion. The Raman spectra for the ECEG and the traditional GO in the range from 1200 cm^{-1}

to 3500 cm^{-1} are presented in Figure 3.16. It is clearly seen that the intensity of the 2D band (around 2700 cm^{-1}) of ECEG is much stronger than that of the GO sample. The 2D/G ratio is related to the degree of recovery for sp^2 C=C bonds (graphitization) in graphitic structures. Therefore, the quality of the graphene obtained from the electrochemical exfoliation is much higher than GO. Additionally, the quality of the ECEG can also be proved by the shape of the peaks of D and G bands, which are much narrower than those of the GO sample, indicating the low content of the defects. However, the presence of the D band in the ECEG sample is possibly due to the unavoidable oxidation by sulphuric acid when the positive electrical potential is applied on the graphite flakes.

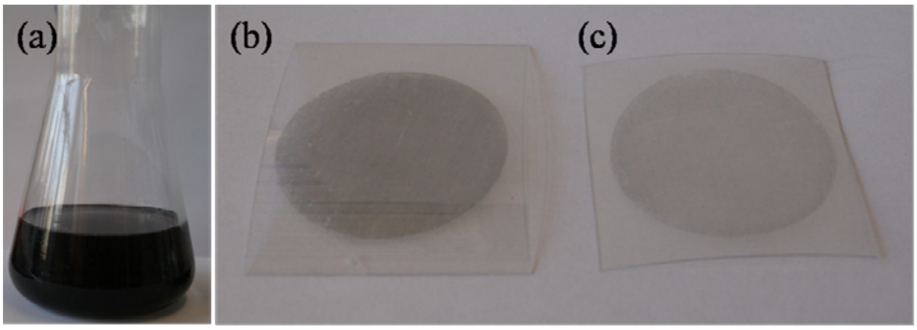

Figure 3.17 OM images of the ECEG dispersion and its film on PET substrate prepared via a dry transfer technology.

We argue that the filtering/transfer is the best method for the fabrication of ECEG films because of its low solubility. For the traditional GO dispersion, mixed cellulose ester membrane (Millipore) is normally used to filter thin GO films to be transferred on other substrates like glass, quartz or plastic substrates. As a wet transfer method, the membrane needs to be washed away with acetone. Thus contamination can not be avoided because of remaining cellulose ester after washing. However, for the ECEG dispersion, a dry transfer processing was developed to transfer graphene film on PET substrate using the Teflon membrane as the filter. The low adhesion between the Teflon membrane and the graphene sheets is extremely low, which is a benefit for the successful transfer of graphene films on other substrates. In a typical experiment, the ECEG dispersion was firstly purified by keeping the ECEG dispersion for one day to remove the big precipitated particles. Then the dispersion was filtered with a Teflon membrane to form a homogenous film. Subsequently, the top surface of Teflon membranes was pressed on a PET substrate, which was pre-wetted with acetone. The ECEG film was allowed to dry and adhere to the substrate at room temperature under a 1 kg weight for at least 1 min. After removing the pressure, the Teflon membrane could be easily exfoliated to leave the ECEG film on the PET substrate. By controlling the volume of the ECEG dispersion, the ECEG films with different transmittance could be obtained as illustrated in Figure 3.17(b) and (c). The sheet resistance of the film as shown in Figure 3.17(b) is 1.2 kOhm/square with the transmittance of 65 % at 500 nm, and that of the film in Figure 3.17(c) is 2.5 kOhm/square with the transmittance of 78 % at 500 nm.

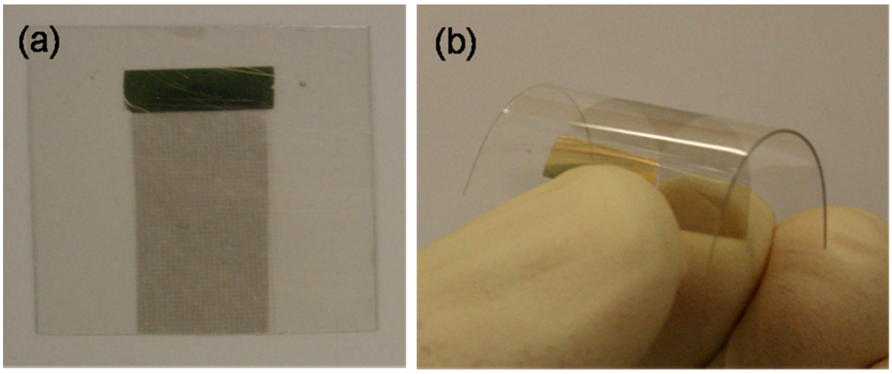

Figure 3.18 OM images of the ECEG films on PET substrate with the 30 nm thick metal grids.

As discussed in chapter 2, the graphene/metal grid hybrid electrodes have exhibited promising performance when used as transparent electrode in organic solar cells. Based on the transferred ECEG film, flexible graphene/metal grid hybrid electrodes could also be fabricated. Firstly, the gold grids were patterned on the PET substrate using photolithography as illustrated in chapter 2. Then the ECEG film was transferred on the top of the metal grids forming the hybrid electrodes. Figure 3.18 features the OM images of graphene/metal grid hybrid electrodes on PET substrate, with a transmittance of ~ 70 % (at 500 nm) and sheet resistance of < 200 Ohm/square. Because graphene film is on the top the metal grid, the metal will not influence the work function of the hybrid electrode. Thus, the metal grid electrodes can also be silver, copper or aluminum.

3.5 Conclusion

In this chapter, LB assembly, LBL assembly, and filtering/transfer technologies have been applied to prepare thin graphene films. Based on the LB assembly, monolayer and multilayer GO films were fabricated by controlling the concentration of the GO precursor. After thermal reduction, the monolayer RGO film (on silicon substrate) showed reproducible FET properties, with a hole mobility of 1.15 $cm^2V^{-1}S^{-1}$. For a 5 nm thick flexible GO film on PET substrate, the reduction was carried out with N_2H_4 vapor at room temperature, resulting in a conductivity of ~ 5 S/cm.

The LBL assembly procedure combined with an in-situ photoreduction was subsequently developed to fabricate the composite films of RGO and PW12 clusters. In this method, the negatively charged GO sheets and PW12 clusters were alternatively deposited on substrates, followed by an irradiation of UV light to convert GO into RGO via a PW12-assisted photoreduction. The prepared films are smooth and uniform, and also show repeatable FET properties. As an advantage of the photoreduction, conductive patterns were directly fabricated on the composite film by using a photoreduction lithography procedure.

The filter/transfer based on the electrochemically exfoliated graphene dispersion has been proved to be an efficient method for fabricating highly conductive graphene films on PET substrate. The sheet resistance of the transferred graphene film is ~ 2.5

kOhm/square with the transmittance of 78 % (500 nm), which is comparable to the thermally reduced GO film. The subsequent combination of metal grid has further decreased the sheet resistance to < 200 Ohm/square.

References

[1] G. Eda, G. Fanchini, M. Chhowalla, *Nat. Nanotechnol.* **2008**, *3*, 270.

[2] K. S. Novoselov, Z. Jiang, Y. Zhang, S. V. Morozov, H. L. Stormer, U. Zeitler, J. C. Maan, G. S. Boebinger, P. Kim, A. K. Geim, *Science* **2007**, *315*, 1379.

[3] T. T. Tang, Y. B. Zhang, C. H. Park, B. S. Geng, C. Girit, Z. Hao, M. C. Martin, A. Zettl, M. F. Crommie, S. G. Louie, Y. R. Shen, F. Wang, *Nat. Nanotechnol.* **2010**, *5*, 32.

[4] K. S. Novoselov, A. K. Geim, S. V. Morozov, D. Jiang, Y. Zhang, S. V. Dubonos, I. V. Grigorieva, A. A. Firsov, *Science* **2004**, *306*, 666.

[5] A. K. Geim, K. S. Novoselov, *Nat. Mater.* **2007**, *6*, 183.

[6] J. S. Wu, W. Pisula, K. Mullen, *Chem. Rev.* **2007**, *107*, 718.

[7] F. Schwierz, *Nat. Nanotechnol.* **2010**, *5*, 487.

[8] F. Bonaccorso, Z. Sun, T. Hasan, A. C. Ferrari, *Nat. Photonics* **2010**, *4*, 611.

[9] S. Gilje, S. Han, M. Wang, K. L. Wang, R. B. Kaner, *Nano Lett.* **2007**, *7*, 3394.

[10] X. Wang, L. J. Zhi, K. Mullen, *Nano Lett.* **2008**, *8*, 323.

[11] H. A. Becerril, J. Mao, Z. Liu, R. M. Stoltenberg, Z. Bao, Y. Chen, *ACS Nano* **2008**, *2*, 463.

[12] B. W. Laursen, K. Norgaard, N. Reitzel, J. B. Simonsen, C. B. Nielsen, J. Als-Nielsen, T. Bjornholm, T. I. Solling, M. M. Nielsen, O. Bunk, K. Kjaer, N. Tchebotareva, M. D. Watson, K. Mullen, J. Piris, *Langmuir* **2004**, *20*, 4139.

[13] A. L. S. Gamboa, E. J. M. Filipe, P. Brogueira, *Nano Lett.* **2002**, *2*, 1083.

[14] M. K. Massey, C. Pearson, D. A. Zeze, B. G. Mendis, M. C. Petty, *Carbon* **2011**, *49*, 2424.

[15] L. Valentini, V. Bavastrello, I. Armentano, F. D'Angelo, G. Pennelli, C. Nicolini, J. M. Kenny, *Chem. Phys. Lett.* **2004**, *392*, 214.

[16] Z. L. Du, Z. J. Zhang, W. L. Zhao, Z. Q. Zhu, J. Zhang, Z. S. Jin, T. J. Li, *Thin Solid Films* **1992**, *210*, 404.

[17] P. Mandal, S. S. Talwar, S. S. Major, R. S. Srinivasa, *J. Chem. Phys.* **2008**, *128*, 114703.

[18] S. Karaborni, *Langmuir* **1993**, *9*, 1334.

[19] X. Huang, M. H. Liu, *Langmuir* **2006**, *22*, 4110.

[20] T. Angelov, D. Radev, G. Ivanov, D. Antonov, A. G. Petrov, *J. Optoelectron. Adv. Mater.* **2007**, *9*, 424.

[21] Y. Z. Guo, N. Minami, S. Kazaoui, J. B. Peng, M. Yoshida, T. Miyashita, *Physica B-Condensed Matter* **2002**, *323*, 235.

[22] V. B. Fainerman, D. Vollhardt, *Langmuir* **1999**, *15*, 1784.

[23] L. J. Cote, F. Kim, J. X. Huang, *J. Am. Chem. Soc.* **2009**, *131*, 1043.

[24] M. Chhowalla, G. Eda, *Nano Lett.* **2009**, *9*, 814.

[25] G. Williams, B. Seger, P. V. Kamat, *ACS Nano* **2008**, *2*, 1487.

[26] K. K. Manga, Y. Zhou, Y. L. Yan, K. P. Loh, *Adv. Funct. Mater.* **2009**, *19*, 3638.

[27] H. Li, S. Pang, X. Feng, K. Müllen, C. Bubeck, *Chem. Commun.* **2010**.

[28] L. J. Cote, R. Cruz-Silva, J. X. Huang, *J. Am. Chem. Soc.* **2009**, *131*, 11027.

[29] S. Q. Liu, D. G. Kurth, B. Bredenkotter, D. Volkmer, *J. Am. Chem. Soc.* **2002**, *124*, 12279.

[30] H. Yamaguchi, G. Eda, C. Mattevi, H. Kim, M. Chhowalla, *ACS Nano* **2010**, *4*, 524.

[31] T. Kobayashi, N. Kimura, J. B. Chi, S. Hirata, D. Hobara, *Small* **2010**, *6*, 1210.

[32] S. Stankovich, D. A. Dikin, R. D. Piner, K. A. Kohlhaas, A. Kleinhammes, Y. Jia, Y. Wu, S. T. Nguyen, R. S. Ruoff, *Carbon* **2007**, *45*, 1558.

[33] D. Li, M. B. Muller, S. Gilje, R. B. Kaner, G. G. Wallace, *Nat. Nanotechnol.* **2008**, *3*, 101.

[34] X. L. Chen, K. M. Song, J. H. Li, J. P. Liu, *Carbon* **1996**, *34*, 1599.

[35] A. Celzard, J. F. Mareche, G. Furdin, *Carbon* **2002**, *40*, 2713.

[36] X. L. Li, G. Y. Zhang, X. D. Bai, X. M. Sun, X. R. Wang, E. Wang, H. J. Dai, *Nat. Nanotechnol.* **2008**, *3*, 538.

[37] C. Y. Su, A. Y. Lu, Y. P. Xu, F. R. Chen, A. N. Khlobystov, L. J. Li, *ACS Nano* **2011**, *5*, 2332.

Chapter 4

Patterned Graphene Electrodes for Organic Field Effect Transistors

Another application of graphene electrodes is in organic field effect transistors. In this chapter, we demonstrate a novel approach based on an oxygen plasma etching for the preparation of patterned graphene electrodes from RGO films on silicon substrate. The p-type P3HT and n-type N,N'-dioctyl-1,7-dibromo-perylene diimide ($C_{40}H_{40}Br_2N_2O_4$) FETs based on the as-fabricated graphene patterns as source and drain electrodes have been investigated, resulting in comparable or even higher performances than devices consisting of gold contacts. The improvement of the performance is attributed to the relatively low contact resistance between graphene electrodes and organic semiconductor materials. Subsequently, to extend the applications of the graphene electrodes in flexible OFETs, graphene patterns on flexible PET substrate have also been fabricated. Remarkable enough, the threshold voltage of p-type pentacene FETs was reduced from -20 V to -8 V by using graphene to replace gold contact as the source/drain electrodes.

4.1 Introduction

OFETs have attracted considerable interest due to their incorporation as fundamental building blocks for plastic electronics such as bendable displays or radio frequency identification tags.[1, 2] Most generally, gold source and drain electrodes are widely used as hole-injecting metals due to its good chemical stability and suitable work function.[3] Several alternative materials have been introduced as potential substitutes for the expensive and increasingly rare gold as charge injecting metal in OFETs. For instance, carbon nanotubes[4-6] and carbon nanotube/polymer nanocomposites[7, 8] have been produced and tested as S/D electrodes in OFETs with a significant reduction of the contact resistance. Although the performance of carbon nanotubes contacted OFETs has been improved in comparison to transistors made with gold electrodes, the higher cost and inconvenient processing of the former devices remain serious disadvantages. On the other hand, these obstacles are circumvented by conductive polymers, such as PEDOT:PSS, which have been successfully applied as solution-processed electrodes in OFETs.[9, 10] This material, however, suffers from low conductivity. Furthermore, pristine PEDOT:PSS degrades in moisture, which prohibits its practical application in OFETs driven under ambient conditions.[11]

The advantages of graphene electrode are low electrical resistivity, high chemical stability, and mechanical strength and the low contact resistance with the organic semiconductors, which call for the incorporation of graphene as electrodes in organic electronic devices. One of the most important characteristic of graphene is its work function, which is similar to that of gold and enables possible Ohmic hole injection into most organic semiconductors. OFETs are generally constructed in a bottom contact configuration, i.e. the organic semiconductor film is deposited on top of the transistor substrate consisting of the gate, insulator, and S/D contacts.[12] The electrodes are exposed to organic solvents or oxygen and moisture for solution-processed devices. Thus, inferior transistor performance through possible degradation of the contacts' electrical properties can be prevented by the chemical stability of graphene.

Motivated by these considerations, we report a novel approach for the preparation of regular graphene patterns. Plasma etching, as a conventional technology in semiconductor industry, is practical for making graphene patterns on a large scale. It was found that aluminum as the sacrificial material is superior to photoresists to define an accurate structure due to its high stability in the oxygen plasma. The OFETs based on the graphene patterns as the source and drain electrodes show comparable or even higher performance compared to the gold contact devices.

4.2 Fabrication of graphene patterns

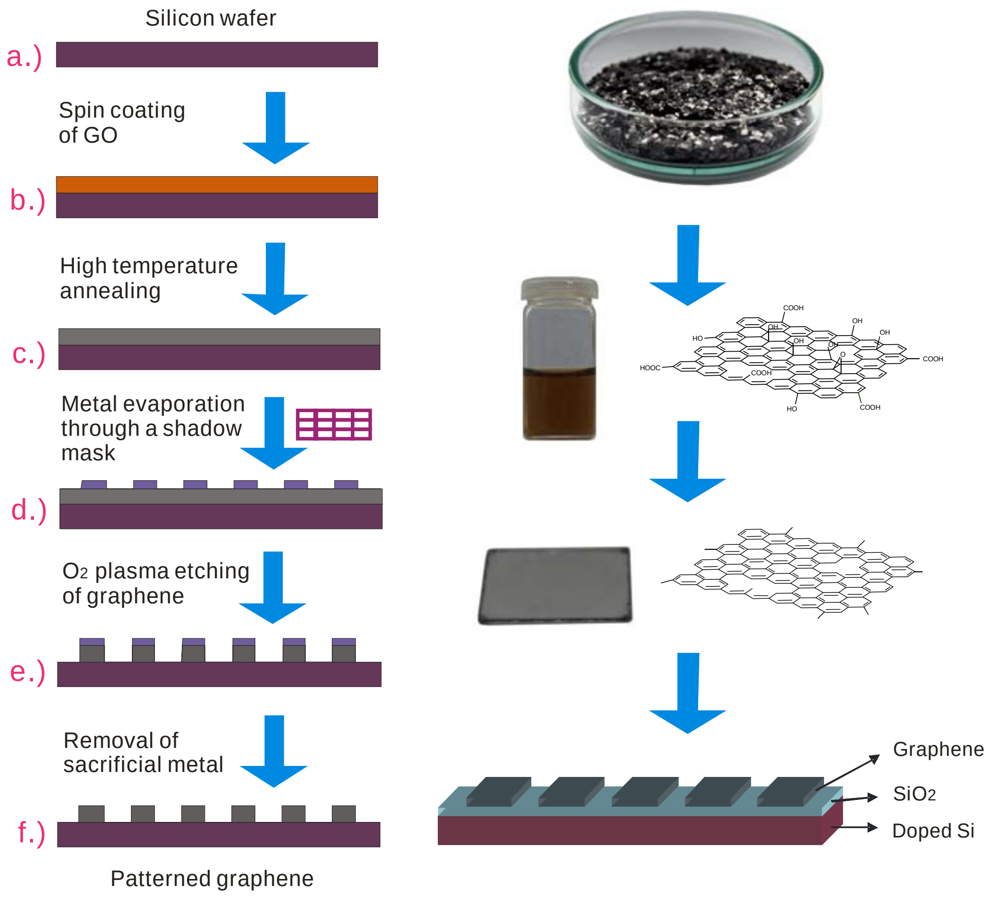

Figure 4.1 Schematic illustration of the fabrication approach towards patterned graphene electrodes.

There are many methods to prepare graphene, such as mechanical exfoliation of HOPG,[13] thermal decomposition of SiC, or epitaxial growth on metal substrates.[14] However, exfoliation and thermal decomposition of SiC provide no control over homogeneous large area film formation. For epitaxial growth, the major challenge is to transfer the graphene films to device substrates. Liquid-phase exfoliation of graphite is also not practical for fabricating thick films due to the low concentration and high boiling point of the solvent.[15] The graphite oxidation and reduction process employed in this work is hence particularly appealing for creating large scale and homogeneous graphene layers at low cost compared to the other aforementioned methods.

To pattern graphene electrodes on silicon substrates, a conductive graphene film was firstly prepared. In a typical experiment, GO dispersion prepared from natural graphite by the Hummers' method was centrifuged at 10000 rpm to obtain a concentrated GO colloid (~ 6 mg/mL) and then sonicated for 3 h to make it homogenous. To increase the hydrophilicity of the silicon substrate, the silicon (with 150 nm thick SiO_2 layer) was firstly treated with an oxygen plasma (Plasma System 200) for 10 min at the power of 300 W. Subsequently, the ~ 60 nm thick GO film was obtained by spin-coating from GO colloid. Then the GO film was thermally reduced at 1000 ^{o}C for 30 min with a heating rate of 2 ^{o}C/min from 150 ^{o}C to 1000 ^{o}C, resulting in a conductivity of ~ 500 S/cm (Figure 4.1 a-c).

To define the structure of the graphene electrodes, 60 nm thick aluminum patterns were thermally evaporated on the top of graphene film through 300 mesh copper grids (Plano) as shown in Figure 4.1(d). The substrate was then exposed to an oxygen plasma for 5 min with 20 sccm oxygen flow at a power of 300 W (Figure 4.1e). After oxygen plasma etching, the aluminum patterns can be easily removed by immersing the substrate in a 5 % HNO_3 solution for 60 min (Figure 4.1f).

To study the effect of the thickness and the conductivity of the graphene electrodes on the OFET performance, 20 and 60 nm thick graphene films were prepared at different pyrolysis temperatures (1000 ^{o}C, 600 ^{o}C and 300 ^{o}C respectively). All of the graphene films, pyrolyzed at 1000 ^{o}C, were not destroyed during this wet chemical etching process. However, this point did not hold for graphene films pyrolyzed at lower temperatures. For instance, the graphene films pyrolyzed at 300 ^oC were completely removed when we etched away the aluminum with HNO_3 solution. However, for the sample prepared at 600 ^oC, partial destruction was observed for high thickness film, and we found that only a 20 nm-thick patterned graphene film was left after the wet chemical etching. The removal of graphene films from the silicon substrates is attributed to the lower adhesion force between the substrate and graphene layer. Accordingly, the high temperature treatment not only offers the good conductivity for graphene film, but also improves the adhesion between the silicon substrate and graphene layers.

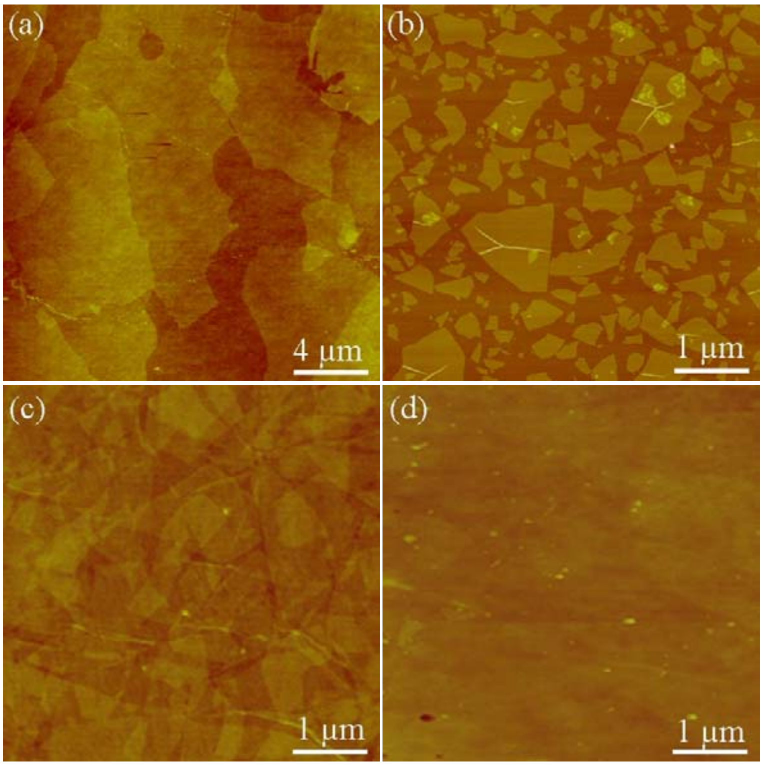

Figure 4.2 (a, b) AFM images of GO on mica substrates. (a) as-prepared large GO sheets, (b) small GO sheets obtained by a ultrasonic treatment for 3 h. (c) AFM images of a 60 nm thick GO film spin coated on silicon substrate from a 5 mg/mL of GO dispersion at 1000 rpm. (d) a 20 nm thick graphene film after pyrolysis at 1000 ^oC for 30 min of the 60 nm thick GO film (c).

The average size of the as-prepared GO sheets before sonication is about 20 μm as shown in Figure 4.2(a). As mentioned in chapter 1, it is difficult to make homogeneous thick RGO films (tens nanometers) from such large GO precursors because the produced gas during the thermal reduction will easily exfoliate the graphene film from the substrate. Small-sized GO flakes (0.2-1 μm, Figure 4.2b) were synthesized by a sonication of the large-sized GO precursor for 3 h. The GO film fabricated by spin-coating from the small GO sheets is shown in Figure 4.2(c). It was found that all the GO sheets remained flat and arranged parallel to the substrate. The reduction was achieved by a thermal pyrolysis at elevated temperatures. After pyrolysis at 1000 ^{o}C for 30 min, the thickness of the graphene film decreased to ~ 23 nm, about one-third of the thickness of the starting GO layer. This is attributed to the shrinking of the interlayer space, corresponding to the removal of the functional groups in GO in the form of CO, CO_2 etc.[16] Evidently, the surface of graphene layers becomes smoother than the original GO film, indicating better graphitization after thermal treatment (Figure 4.2c). After 1000 ^{o}C thermal reduction, the adhesion between the RGO film and the silicon substrate is very strong and can not be exfoliated in the subsequent patterning process.

To compensate for the thickness reduction after pyrolysis, much thicker GO films are needed to obtain the desired graphene films. Thus the thickness of the patterned graphene film can be easily controlled by adjusting the concentration of the GO precursor, the spin-coating speed, and the number of spin-coating cycles. For a 60 nm thick RGO film as an example, a ~ 150 nm thick GO film is required. Thus, we must spin coat three times to obtain enough thickness. Normally, the former GO layer need to be thermally annealed to make it stable before spin-coating the subsequent GO layers. Otherwise, the former GO film will be destroyed because the pre-coated GO film can be dissolved in the new GO solution. In our experiment, 60 ^{o}C annealing treatment was used. Additionally, to avoid the exfoliation of the RGO film from the silicon substrate, a slow heating rate of 2 ^{o}C/min was performed.

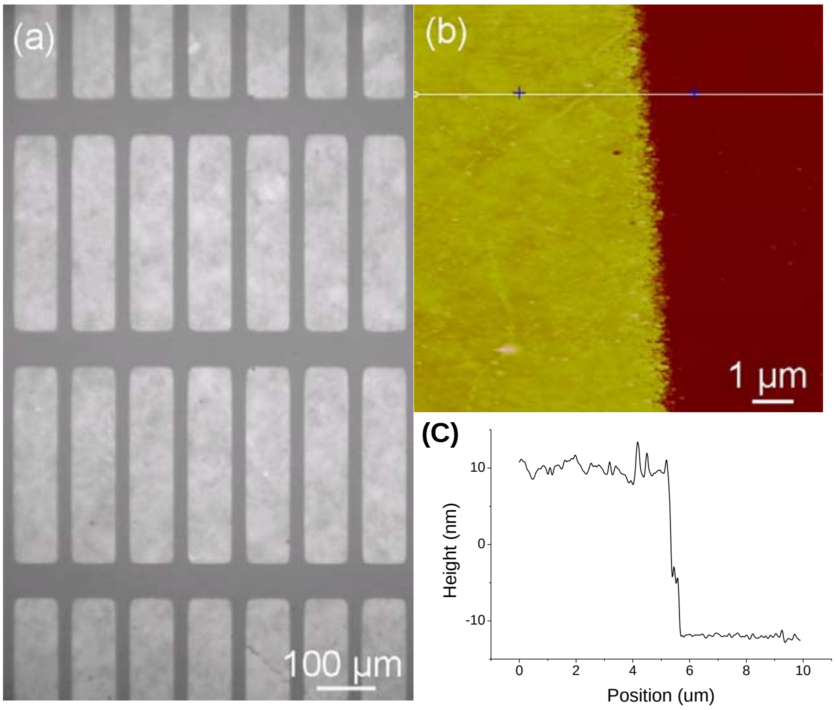

Figure 4.3 (a) OM image of patterned graphene electrodes with channel length of 25 μm and width of 290 μm. (b) AFM image of an edge of the patterned graphene electrode. (c) Height profile along the line in (b), showing micro-channel etched down to the underlying SiO_2/Si substrate.

The resulting graphene patterns are illustrated as white squares in the OM image (Figure 4.3a). The size of the graphene electrodes is exactly consistent with the mask containing channel lengths of 25 μm and widths of 290 μm. The sharp and regular contact edges can be clearly seen from the AFM image in Figure 4.3(b). The area exposed to the oxygen plasma was completely etched, while the patterns protected by aluminum survived in the plasma etching treatment. The height profile (Figure 4.3c) along the line in Figure 4.3(b) indicates complete etching of the graphene contacts down to the underlying substrate within the transistor channel.

Up to now, several patterning techniques have been reported to fabricate graphene electrodes for organic electronic devices. Using the stamping to make graphite nanoplatelet composite patterns has been studied, but it is difficult to obtain sharp edges, which restricts its use for electrode materials.[17] Conventional photolithography and active ion etching are widely used in micro-fabrication to selectively remove parts of a thin film followed by a liquid ("wet") or plasma ("dry") chemical etching.[18, 19] Oxygen plasma etching described in this work is most suitable for making patterned graphene electrodes in conjunction with aluminum as the sacrificial material, which is more stable than photoresists during plasma treatment.

4.3 p-type OFETs based on graphene electrodes

Before studying the OFET performance based on the graphene S/D electrodes, a short description of the construction of bottom-gate bottom-contact (Figure 4.4a) and top-gate bottom-contact (Figure 4.4b) is presented as follows.

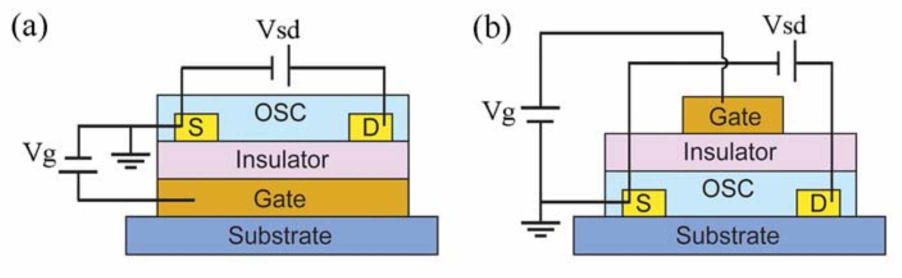

Figure 4.4 Structure of bottom contact, bottom gate OFET (a) and bottom contact, top gate OFET (b). OSC stands for the organic semiconductor film.

FETs are fundamental building blocks for modern electronics, serving as fast switches in displays or computer microprocessors. The main task of transistors is to modulate the current. By doing this, the electric current can be switched on and off, and that is exactly what a transistor should do: acting as switches in order for example to perform binary logic for computations in microelectronics or to switch individual pixels in a display. Take the bottom-gate bottom contact FET as an example (Figure 4.4a), the FET consists of a gate electrode covered by a dielectric layer. On top of this insulator, the semiconductor film is deposited and contacted by S/D electrodes with a certain width (W) and separation distance. This distance is called the channel length (L) since this is where the charge carriers are flowing between these two electrodes.

The potential applied to these two contacts V_{sd} and the potential across the source and gate electrodes V_g can control the current flowing through the semiconductor from the source to the drain. The effect of the gate potential V_g is to accumulate charge carriers at the semiconductor-insulator interface, forming a channel, the so-called accumulation layer filled with charge carriers connecting the source and drain electrodes. Depending on whether a positive or negative voltage is applied, either electrons or holes will be accumulated within the semiconductor layer at the dielectric surface.

Actually, besides the semiconductor, the performances of FETs, including the mobility, on/of ratio and threshold voltage, are also affected by the construction of devices, such as the selection of the insulating materials and the S/D electrodes. Gold is typically used as hole-injecting metals in organic electronic devices.

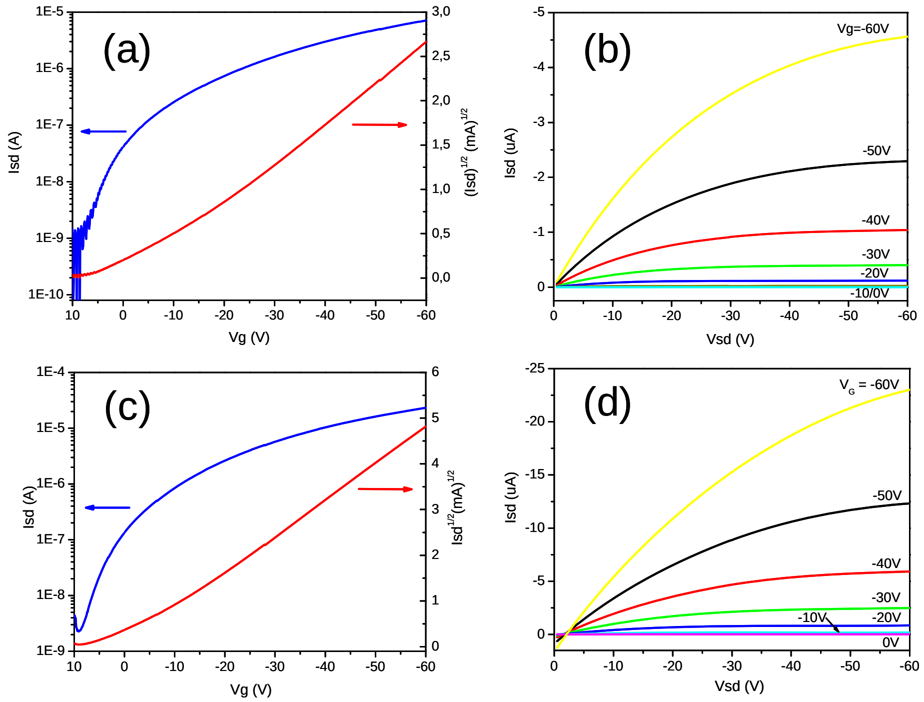

Figure 4.5 (a) Transfer characteristics at a source-drain bias of V_{sd} = -60V and (b) Output characteristics of P3HT OFETs employing patterned 60 nm thick gold source and drain electrodes. (c) Transfer characteristics and (d) Output characteristics with patterned 60 nm thick graphene source and drain electrodes annealed at 1000 °C.

To investigate the suitability of the patterned graphene electrodes for p-type P3HT OFETs, bottom contact-bottom gate OFETs were fabricated on patterned gold and graphene electrodes. For gold contacting devices, 60 nm thick gold electrodes were firstly evaporated through a 300 mesh copper grids. Then the patterned substrates were treated with oxygen plasma to clean the surface and make it hydrophilic for the subsequent surface modification with 1,1,1,3,3,3-hexamethyldisilazane (HMDS). Firstly, the plasma treated silicon substrate with patterned gold electrodes was put in a small Petri dish and then transferred into a glass container with a sealable cap that does not permit out flow of gas. Then about 0.5 mL of HMDS was dropped in the glass container, which was sealed and placed in an oven at 120 ^{o}C for 3 hours. In the last step, the container will be filled with HMDS vapor in which the HMDS molecules adsorb on the SiO_2 surface, in this way forming methyl end capped interfaces. Finally, the samples were taken out from the container and cleaned by sonication in acetone for 5 minutes followed by rinsing in isopropanol and drying with a nitrogen flow.

For the silicon substrate with patterned graphene electrodes, the surface of the silicon substrate was already hydrophilic, which was ready for the HMDS modification. Thus the modification process is similar to the above mentioned strategy but without pre-oxygen plasma treatment.

The OFETs based on the gold and graphene S/D electrodes were fabricated and measured in a nitrogen filled glove box. A 5 mg/mL of P3HT (4002-E, Rieke Metals, Inc.) chloroform solution was spin coated at 2000 rpm on HMDS treated substrate with 150 nm thermally grown SiO_2 insulator layer and containing graphene or gold source and drain contacts. Highly n^{++} doped silicon below the SiO_2 layer served as the gate. The conductivities of the graphene films were measured by a standard four point-probe system with a Keithley 2700 Multimeter (probe spacing: 0.635 mm, $R_s = 4.5324 \times V/I$). The FET measurements were taken with a Keithley SCS 4200 semiconductor characterization system. Before measuring the electronic performance of the OFETs, all of the devices were annealed at 120 ^{o}C for 10 min in the glove box. The mobility of the OFETs was calculated from the equation: $\mu_{sat} = m^2 2L/WCi$ (m: the slop of the linear fit at square root of the transfer curve; L: channel length; W: channel width; Ci: the capacitance per unit area of he dielectric layer).

The transfer characteristics for various gate biases V_g and output characteristics (V_{sd} = -60 V) of P3HT OFETs employing patterned 60 nm thick gold source and drain electrodes are shown in Figure 4.5(a) and (b), respectively. The output and transfer curves reveal a characteristic p-type performance. The P3HT provided consistent OFET operation following the conventional transistor models in both the linear and saturated regimes. The output curves display clear saturation, with the extracted mobility from the saturated regimes being up to μ_{sat} = 0.017 $cm^2 V^{-1}s^{-1}$ with a typical on/off ratio of 10^4. The threshold voltage obtained from the transfer curve is about +5 V. However, the P3HT devices based on graphene as the S/D electrodes exhibited improved performance (Figure 4.5c, d). The hole mobility is ~ 0.04 $cm^2 V^{-1}s^{-1}$ with the on/off ratio of 10^4 as averaged over five devices. Typical output and transfer characteristics of the OFETs are illustrated in Figure 4.5(c) and (d) respectively. As evident from the output curves illustrated in Figure 4.5(b), there is an absence of nonlinear current increase I_{sd} at low source drain biases V_{sd}. This lack of nonlinear behavior points to the presence of an Ohmic contact between the graphene electrodes and the P3HT layer.[20, 21] A minimization of the contact resistance was also achieved in carbon nanotube electrodes applied in OFETs.[4] However, graphene sheets mediated from soluble GO undoubtedly constitute a more cost-effective material than carbon nanotubes. The improvement of the graphene based P3HT OFETs was also reflected on the decrease of the threshold voltage. The threshold voltage was decreased from -3 V to 0 V when using graphene to replace gold. Thus, the source and drain electrodes consisting of graphene sheets did not pose significant contact resistances that might limit charge carrier mobility. Both the higher mobility and the lower threshold voltage have indicated that the graphene contact is better than the gold contact in the P3HT OFET devices. This improved device performance containing patterned graphene contacts in comparison to those made out of gold renders graphene an attractive low-cost alternative electrode in organic electronics.

The 60 nm thick S/D graphene electrodes show a conductivity of ~ 500 S/cm after pyrolysis at 1000 °C. Compared to gold or carbon nanotubes, this value for graphene electrodes is rather lower. It is still possible, however, to reach transistor action comparable to gold contact OFETs. The interesting point is then to investigate whether OFETs will still function with even low conductivities. In this respect, a lower annealing temperature of 600 °C was applied, generating a conductivity of 250 S/cm. A hole mobility of 3×10^{-3} cm^2 $V^{-1}s^{-1}$ was measured for a 20 nm thick patterned graphene contact device, showing performance one order of magnitude lower than for the highly conductivitve graphene electrodes.

4.4 n-type OFETs based on graphene electrodes

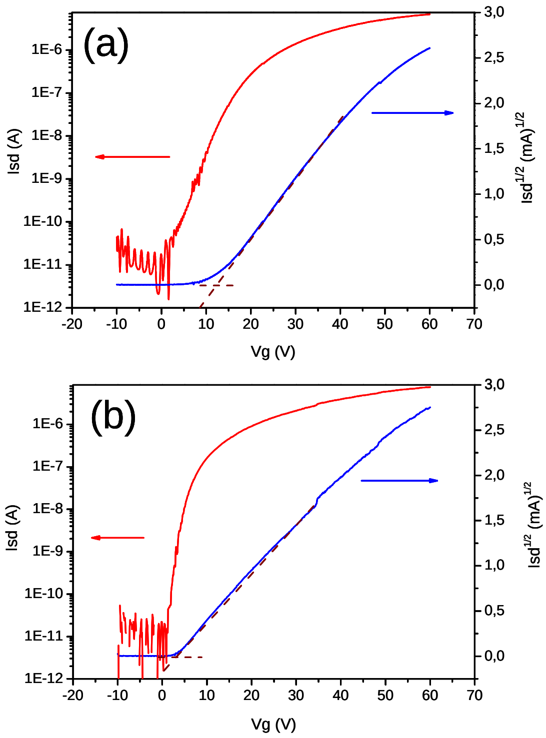

Figure 4.6 Transfer characteristics at a source-drain bias of V_{sd} = + 60V of PDI-2Br OFETs employing patterned 60 nm thick gold source and drain electrodes (a) and graphene electrodes (b).

Current electronic technologies like processors in computers are all based on complementary metal oxide semiconductor (CMOS) units that allow the operation of binary logic. CMOS requires both hole and electron transporting transistors. As a promising electrode material for organic electronics, the study of the contact resistance between graphene and n-type semiconductor is also very important for its future applications. In this part, n-type N,N'-dioctyl-1,7-dibromo-perylene diimide ($C_{40}H_{40}Br_2N_2O_4$) was used as active material to explore the contact property between the graphene and n-type semiconductor. Firstly, the silicon substrates with patterned graphene or gold electrodes were modified with a HMDS layer. The active layer, n-type $C_{40}H_{40}Br_2N_2O_4$, was spin coated from the chloroform solution with a concentration of 2 mg/mL at 2000 rpm for 60 s. Before measuring the OFETs, the devices were annealed at 120 ^{o}C for 10 min under nitrogen. As shown in Figure 4.6, the transfer curves reveal a characteristic n-type behavior. The I_{sd} of the graphene contact OFET increases faster than gold contact, indicating the presence of an Ohmic contact between graphene electrodes and the n-type semiconductor $C_{40}H_{40}Br_2N_2O_4$ layer. It means the electrons are much easier to inject from graphene than from gold to $C_{40}H_{40}Br_2N_2O_4$. The electron mobility of the graphene contact $C_{40}H_{40}Br_2N_2O_4$ OFET in the saturation region is 2.4×10^{-3} cm^2 V^{-1}s^{-1}, which is similar to that of the gold contact device (2.9×10^{-3} cm^2 V^{-1}s^{-1}). However, in the linear region (low working V_g), the electron mobility of the graphene contact device is more than once higher than that of the gold contact devices, with a obvious decrease of the threshold voltage from +12 V to +4 V. The improvement of the graphene based OFETs under the low gate voltage enables the $C_{40}H_{40}Br_2N_2O_4$ OFET works well at low energy consumption.

4.5 Comparison of the contact resistances

To fabricate flexible organic electronics, several alternative materials, such as carbon nanotubes and PEDOT:PSS have been reported as potential substitutes for the gold as charge injecting materials in OFETs.[6, 8, 22-24] The improvement of the graphene based OFETs performance is also attributed to the low contact resistance between the alternative electrodes and the semiconductor. To compare the contact resistance of different electrodes with the semiconductor materials, the transfer line

(Figure 4.7) and scanning Kelvin probe microscopy (SKPM) (Figure 4.8) methods are normally used. [12, 25] In our experiments, graphene-gold asymmetrical electrodes (Figure 4.9) were employed to directly compare the contact resistance of the graphene/P3HT and gold/P3HT.

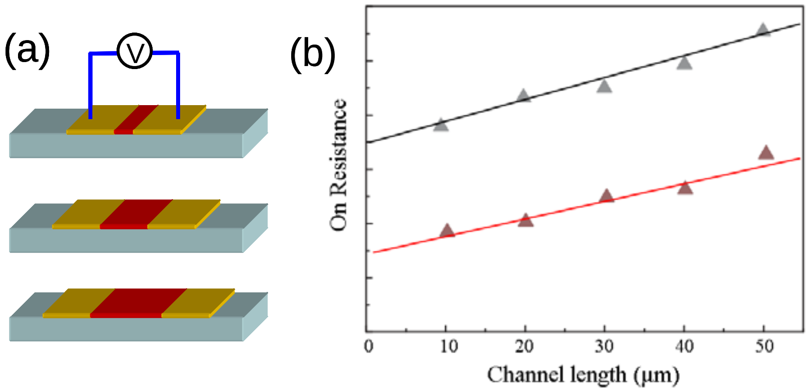

Figure 4.7 Transfer line method to calculate the contact resistance between the electrode and semiconductor material. The contact resistance is the value of resistance when channel length is 0.

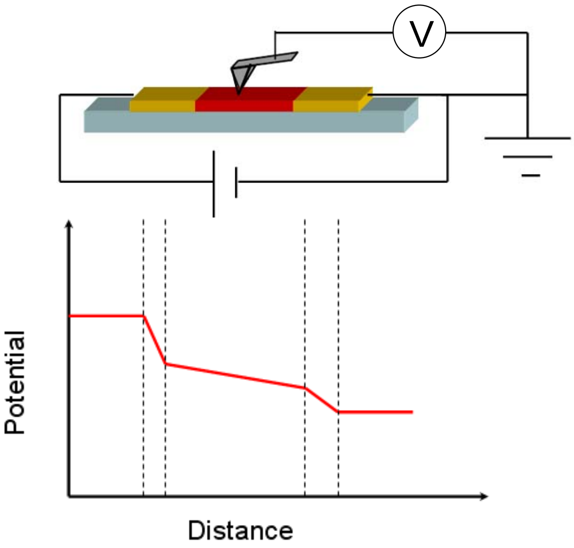

Figure 4.8 Schematic diagram for measuring the surface potential of FET device by using a scanning Kelvin probe microscopy (SKPM).

The transfer line method[12] is based on calculating series resistances between source and drain electrodes with different channel lengths as shown in Figure 4.7(a). The measurement of the resistance is using a two probe method. It is supposed that the resistance of a semiconductor layer is linearly dependence upon the length of the gap, while the resistance at the interface is a constant. Therefore, the resistance in the interface can be easily calculated by the transfer line method when the gap length is zero. This method has been widely utilized to compare the contacting resistance in the OFETs of different electrodes. For instance, single wall carbon nanotubes and PEDOT:PSS show lower resistance than the gold contacts.[4, 10]

In addition to the transfer line method, the contact resistance between electrode and semiconductor material can also be directly measured by SKPM as demonstrated in Figure 4.8.[25] Upon biasing the device, the surface potential map can be obtained by SKPM, providing a reliable way to measure the resistance at the interface of electrode/semiconductor.

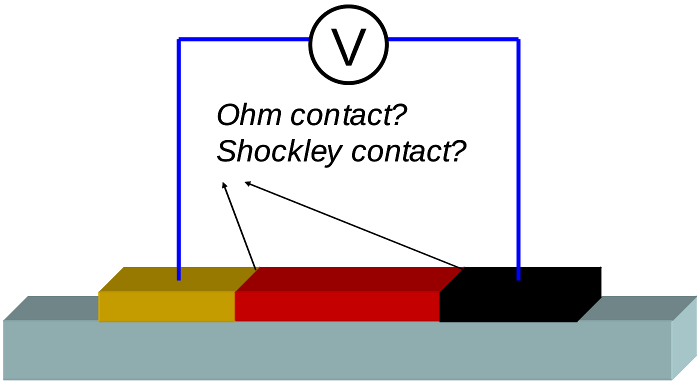

Figure 4.9 Asymmetrical gold-graphene electrodes for comparing the contact resistance between the electrodes and the P3HT.

In our experiments, graphene-gold asymmetrical electrodes were proposed to directly compare the contact resistance of the graphene/P3HT and gold/P3HT (Figure 4.9). In the normal FET devices, the two electrodes (source and drain) are the same, forming a symmetrical structure—metal/semiconductor/metal. Thus, the I-V curve also shows the same character in both forward and reverse directions. However, if one electrode is substituted by another metal with a different work function (Figure 4.9), the symmetrical property is broken and then a diode device can be formed. According to the theory in semiconductor physics, the contact properties of the two different interfaces can be revealed in the I-V curve of the diode, where one direction is the on-state (forward conducting state) and the reverse direction is the off-state (reverse blocking state).[26] Take p-type semiconductor P3HT as an example (the red color in Figure 4.9), in the conducting direction, holes are relatively easier to be injected into the P3HT layer from the electrode, indicating the low contact resistance between the electrode and the semiconductor material. On the contrary, in the reverse direction, holes need to overcome a high barrier to be injected to P3HT, suggesting the relatively high contact resistance. Thereby, this method can be used to directly compare the contacting properties of organic material with different electrode materials.

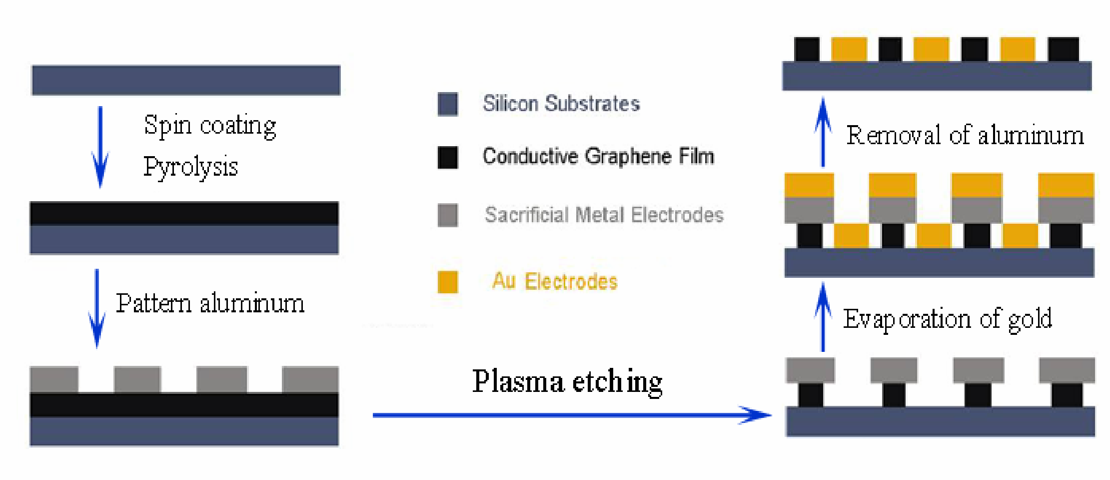

Scheme 4.1 Schematic illustration of the fabrication procedure of the asymmetrical graphene-gold electrodes on silicon substrate.

The patterned graphene-gold electrodes were fabricated similarly to the aforementioned patterning strategy (Figure 4.1). The difference consists in the oxygen plasma etching time and the subsequent evaporation process. For the pure graphene patterns as shown in Figure 4.1, the oxygen plasma is only needed to etch away the graphene where not covered by the aluminum patterns. However, for the asymmetrical graphene-gold electrodes, long-time oxygen plasma etching is required to produce an undercut along the edges of the aluminum patterns as shown in Scheme 4.1. Once a desired undercut is formed, gold layer was evaporated on the substrate. After washing away the sacrificial aluminum layer, a narrow gap (several hundreds nanometers) was produced between the graphene and gold electrodes. The length of the gap can be easily tuned by controlling the oxygen plasma etching time. More detailed fabrication processes of such kind of asymmetrical electrodes will be presented in chapter 5.

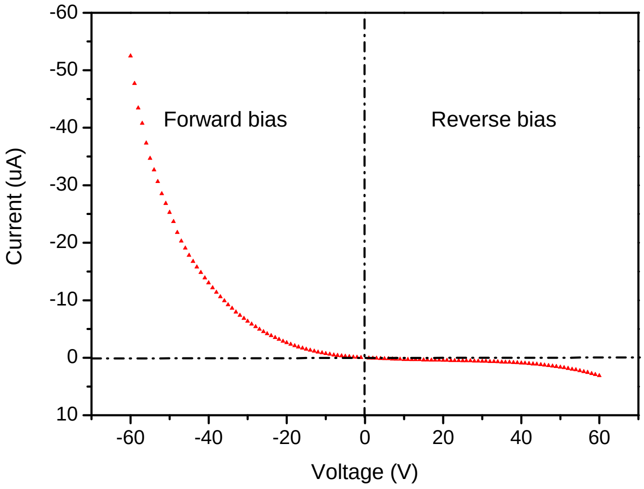

Figure 4.10 I-V curve of graphene-P3HT-gold diode. (Voltage sweeping from -60V to 60 V.)

The graphene/P3HT/gold structure was fabricated by spin-coating a 5 ml/mL P3HT solution on the top of the as-fabricated graphene-gold asymmetrical patterns and then annealed at 120 ^{o}C for 10 min. The I-V property of this diode device was measured by a Keithley SCS 4200 semiconductor characterization system with a voltage sweep from -60 V to 60 V (Figure 4.10). An obvious diode property was observed due to the asymmetrical electrode structure. As P3HT is a typical p-type semiconductor, the main charge carriers are holes. Thus, when a forward bias is applied on the device, the holes are easily transported from the graphene to the P3HT and then to the gold electrode. On the contrary, when a reverse bias is applied on the device, the transport of the hole from the gold to the P3HT and then to the graphene meets a relatively high resistance. This asymmetrical I-V curve of the graphene-P3HT-gold diode can therefore be used to evaluate the contact property between the electrodes and P3HT.

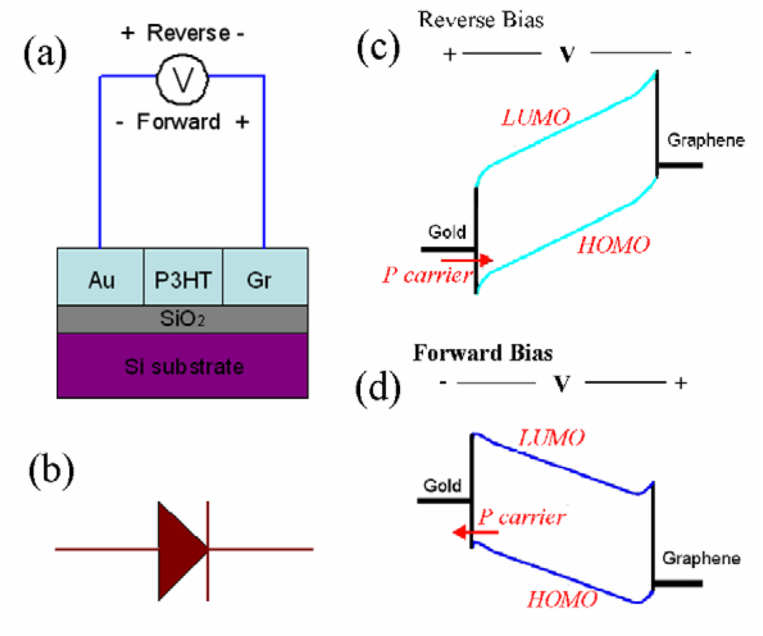

Figure 4.11 Band diagrams for the case of the P3HT under forward and reverse bias.

The definition of “Forward” and “Reverse” is illustrated in Figure 4.11(a). The holes transport from graphene to P3HT and to gold is the “Forward” direction and vice versa. As shown in Figure 4.10, the diode is only conductive in one direction — forward bias — hole from graphene to P3HT and to gold (Figure 4.11b). This behavior can be explained by the band diagrams in Figure 4.11(c) and (d), respectively. In the forward bias state, holes should go through two interfaces: graphene/P3HT and P3HT/gold. And in the reverse bias state, holes go through gold/P3HT and P3HT/graphene. Because the resistance is mainly produced when holes transfer from the electrodes to semiconductor — from gold to P3HT or from graphene to P3HT, it can be concluded that the resistance of gold/P3HT is much higher than that of graphene/P3HT.

4.6 Graphene patterns on PET substrate

Besides the low contact resistance with organic semiconductor materials, flexibility is another important feature for graphene electrodes. To further extend the applications of the graphene electrodes in organic electronics, flexible PET substrates were employed to replace silicon wafer. Since organic polymer substrates can not survive at the elevated temperature, the traditional high temperature thermal reduction is not suitable to convert GO to conductive RGO film. Thus, to fabricate graphene patterns on flexible substrates, a low temperature process is required. However, if only a thermal reduction process is performed to reduce GO to RGO, temperatures as high as ~ 400 °C are needed to provide a conductivity of 10 S/cm. For flexible substrates, such as PET, 400 °C is too high because the substrates will be decomposed at this temperature. On the other hand, the chemical reduction at room temperature only can offer a conductivity of ~ 1 S/cm for graphene film,[27-29] which is also too low to serve as S/D electrodes in OFETs.

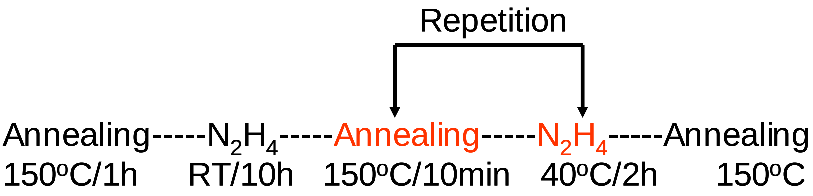

Scheme 4.2 Schematic illustration of the reduction of GO film on PET substrates

Therefore, in order to prepare more conductive graphene films on PET substrates, an optimized reduction process was developed by combining the thermal and chemical reduction together as illustrated in scheme 4.2. For the detailed experiment, the PET substrate was firstly treated under an oxygen plasma for 15 sec to make the surface hydrophilic. Then 50 nm-thick GO film was spin coated from 5 mg/mL GO dispersion and then annealed at 150 °C for 1 h to enhance the adhesion between the GO and the PET substrate. Subsequently, the annealed GO film was subjected to a chemical reduction in a sealed N_2H_4 vapor for 10 h at room temperature. It needs to be mentioned that chemical reduction can decrease the adhesion between the GO film and the substrate due to the formation of the gas that can exfoliate the GO film from the substrates. After that, the film is required to be thermally annealed again to recover the adhesion. However, the temperature increasing rate must be kept as low as possible in order to avoid the formation of large amounts of gas produced during this process. It was found that repeating reduction/annealing cycles enabled an access to high conductivity.[30] For instance, a conductivity of 10 S/cm was obtained via repeating the chemical reduction and annealing treatments for 3 times. Such a value is high enough to be used as the source and drain electrodes in OFETs. The flexibility of the graphene film on the PET substrate was checked by comparing the resistance before and after 100 times bending test. Remarkable enough, the nearly unchanged resistance indicates that graphene films indeed have great potential for flexible electronics. The patterning process of graphene electrodes on PET substrate is similar to that mentioned in Figure 4.2. Interestingly, the graphene patterns on PET substrate are more stable than those on the silicon substrate.

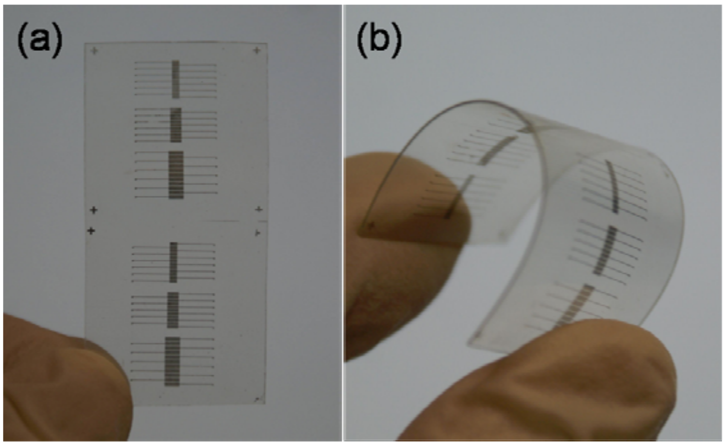

Figure 4.12 OM images of the patterned graphene electrodes on PET substrates.

Figure 4.12 shows a PET substrate with patterned graphene electrodes with a thickness of ~ 60 nm and channel lengths of 50 nm, 100 nm and 200 nm, respectively. The sheet resistance of this flexible graphene film is ~ 20 kOhm/square, which is much lower than that of the semiconductor materials. Taking P3HT as an example (Figure 4.5), the sheet resistance at $V_g = 0$ is about 1×10^7 kOhm/square, and at $V_g = -60$ is about 1×10^5 kOhm/square. Thus the sheet resistance of the graphene electrode is about 0.02 % of that for the P3HT at $V_g = -60$. In this respect, the low temperature reduced GO film should be conductive enough to serve as S/D electrodes in OFETs.

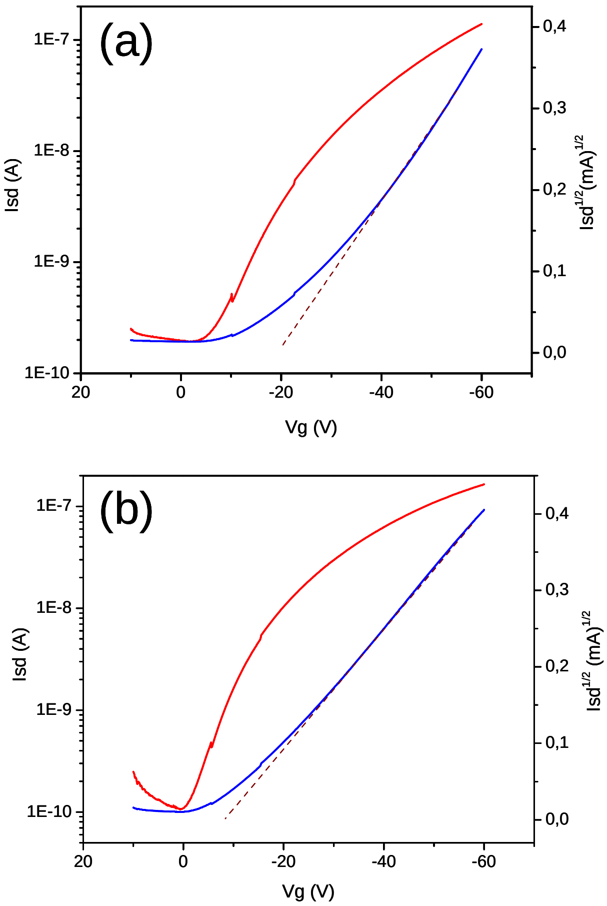

Figure 4.13 The transfer characteristics of pentacene based transistors with gold (a) and graphene (b) as source and drain electrodes, respectively.

To test the PET-supported graphene S/D electrodes in flexible OFETs, P3HT was firstly employed as the semiconductor. Due to the large roughness of the PET substrate, the fabrication of a homogenous semiconductor layer by spin-coating is difficult, resulting in a large current leakage (not shown here). Compared with the spin-coating method, evaporation is more suitable for controlling the thickness of the film. For this purpose, p-type pentacene was employed as the semiconductor to fabricate the bottom contact-top gate OFETs. In a typical experiment, the substrate was firstly rinsed with acetone and isopropanol, and then dried under a gentle nitrogen flow. Afterwards, 60 nm thick pentacene layer was thermally evaporated at the rate of 0.2 Å/s with a substrate temperature of 30 ^{o}C. For the dielectric layer, 5 mg/mL polystyrene solution was spin coated on top of the active layer at a speed of 4000 rpm for 60 seconds. Finally, another 60 nm thick gold film was evaporated on top of the dielectric layer through a gate mask. The OFET measurements were carried out in a nitrogen filled glove box. Transfer characteristics of pentacene OFETs employing patterned 50 nm thick gold and graphene S/D electrodes at a source-drain bias of V_{sd} = -60 V are compared in Figure 4.13. The I_{sd} of the graphene contact OFET increased faster than that with the gold as the S/D electrodes, indicating the presence of an Ohmic contact between the graphene electrodes and the pentacene layer. It can be concluded that holes are much easier to be injected into pentacene from graphene than from gold contact, leading to the lower threshold voltage with the graphene contact device (–8 V) than that with gold contact device (-20 V).

4.7 Conclusion

To conclude, the oxygen plasma etching is an appropriate approach to fabricate patterned graphene electrodes, which have been successfully adopted for silicon and PET substrates. The following OFET studies have proved that the contacting properties of graphene electrodes to the organic semiconductors are comparable or even better than gold because of the low contacting resistance. It means that the holes or electrons can be easier to be injected into the semiconductor layers from the graphene electrodes than from the gold contacts. As a result, the mobility of p-type P3HT based on graphene contacts is once higher than that with gold contacts, while the threshold voltages in both the p-type pentacene and n-type $C_{40}H_{40}Br_2N_2O_4$ semiconductors are reduced with respect to the gold contacts. These findings strengthen graphene as a potential substitute for gold in carrier injecting contacts. The low cost of graphene, suitable work function, high chemical stability and flexibility make it an ideal electrode for organic electronics.

References

[1] H. Sirringhaus, N. Tessler, R. H. Friend, *Science* **1998**, *280*, 1741.

[2] A. R. Brown, A. Pomp, C. M. Hart, D. M. Deleeuw, *Science* **1995**, *270*, 972.

[3] H. Ishii, K. Sugiyama, E. Ito, K. Seki, *Adv. Mater.* **1999**, *11*, 605.

[4] Y. Y. Zhang, Y. M. Shi, F. M. Chen, S. G. Mhaisalkar, L. J. Li, B. S. Ong, Y. L. Wu, *Appl. Phys. Lett.* **2007**, *91*.

[5] Q. Cao, S. H. Hur, Z. T. Zhu, Y. G. Sun, C. J. Wang, M. A. Meitl, M. Shim, J. A. Rogers, *Adv. Mater.* **2006**, *18*, 304.

[6] P. F. Qi, A. Javey, M. Rolandi, Q. Wang, E. Yenilmez, H. J. Dai, *J. Am. Chem. Soc.* **2004**, *126*, 11774.

[7] J. Sung, P. S. Jo, H. Shin, J. Huh, B. G. Min, D. H. Kim, C. Park, *Adv. Mater.* **2008**, *20*, 1505.

[8] M. Lefenfeld, G. Blanchet, J. A. Rogers, *Adv. Mater.* **2003**, *15*, 1188.

[9] X. H. Zhang, S. M. Lee, B. Domercq, B. Kippelen, *Appl. Phys. Lett.* **2008**, *92*.

[10] F. L. Xue, Y. Su, K. Varahramyan, *IEEE Trans. Electron Devices* **2005**, *52*, 1982.

[11] M. Jorgensen, K. Norrman, F. C. Krebs, *Sol. Energy Mater.* **2008**, *92*, 686.

[12] C. A. Di, D. C. Wei, G. Yu, Y. Q. Liu, Y. L. Guo, D. B. Zhu, *Adv. Mater.* **2008**, *20*, 3289.

[13] K. S. Novoselov, A. K. Geim, S. V. Morozov, D. Jiang, M. I. Katsnelson, I. V. Grigorieva, S. V. Dubonos, A. A. Firsov, *Nature* **2005**, *438*, 197.

[14] P. W. Sutter, J. I. Flege, E. A. Sutter, *Nat. Mater.* **2008**, *7*, 406.

[15] Y. Hernandez, V. Nicolosi, M. Lotya, F. M. Blighe, Z. Sun, S. De, I. T. McGovern, B. Holland, M. Byrne, Y. K. Gun'Ko, J. J. Boland, P. Niraj, G. Duesberg, S. Krishnamurthy, R. Goodhue, J. Hutchison, V. Scardaci, A. C. Ferrari, J. N. Coleman, *Nat. Nanotechnol.* **2008**, *3*, 563.

[16] S. Stankovich, D. A. Dikin, R. D. Piner, K. A. Kohlhaas, A. Kleinhammes, Y. Jia, Y. Wu, S. T. Nguyen, R. S. Ruoff, *Carbon* **2007**, *45*, 1558.

[17] T. R. Hendricks, J. Lu, L. T. Drzal, I. Lee, *Adv. Mater.* **2008**, *20*, 2008.

[18] R. Ji, W. Lee, R. Scholz, U. Gosele, K. Nielsch, *Adv. Mater.* **2006**, *18*, 2593.

[19] S. J. Kang, C. Kocabas, H. S. Kim, Q. Cao, M. A. Meitl, D. Y. Khang, J. A. Rogers, *Nano Lett.* **2007**, *7*, 3343.

[20] R. A. Street, A. Salleo, *Appl. Phys. Lett.* **2002**, *81*, 2887.

[21] L. Burgi, T. J. Richards, R. H. Friend, H. Sirringhaus, *J. Appl. Phys.* **2003**, *94*, 6129.

[22] C. M. Aguirre, C. Ternon, M. Paillet, P. Desjardins, R. Martel, *Nano Lett.* **2009**, *9*, 1457.

[23] K. Hong, S. Y. Yang, C. Yang, S. H. Kim, D. Choi, C. E. Park, *Org. Electron.* **2008**, *9*, 864.

[24] H. Yan, T. Kagata, Y. Mori, Y. Harashina, Y. Hara, H. Okuzaki, *Chem. Lett.* **2008**, *37*, 44.

[25] Y. J. Yu, Y. Zhao, S. Ryu, L. E. Brus, K. S. Kim, P. Kim, *Nano Lett.* **2009**, *9*, 3430.

[26] H. M. Manohara, E. W. Wong, E. Schlecht, B. D. Hunt, P. H. Siegel, *Nano Lett.* **2005**, *5*, 1469.

[27] H. J. Shin, K. K. Kim, A. Benayad, S. M. Yoon, H. K. Park, I. S. Jung, M. H. Jin, H. K. Jeong, J. M. Kim, J. Y. Choi, Y. H. Lee, *Adv. Funct. Mater.* **2009**, *19*, 1987.

[28] C. Gomez-Navarro, R. T. Weitz, A. M. Bittner, M. Scolari, A. Mews, M. Burghard, K. Kern, *Nano Lett.* **2007**, *7*, 3499.

[29] H. Lee, I. K. Moon, J. Lee, R. S. Ruoff, *Nat. Commun.* **2010**, *1*.

[30] D. A. Dikin, I. Jung, R. D. Piner, R. S. Ruoff, *Nano Lett.* **2008**, *8*, 4283.

Chapter 5

Coplanar Asymmetrical Graphene-Titanium Electrodes for Polymer Photodetectors

As a development of the oxygen plasma etching technology, coplanar asymmetrical graphene-titanium electrode patterns were fabricated and applied as electrodes in polymer photodetectors. The channel length between graphene and titanium can be easily adjusted by controlling the oxygen plasma etching time. It was found that the polymer photodetectors based on graphene/titanium asymmetrical electrodes exhibited an improved photosensitivity because of the presence of the "build-in" potential. The P3HT photodetectors based on the as-fabricated asymmetrical electrodes show an on/off ratio of 10^3 at a low bias, which is several hundred times higher than that based on the symmetrical gold electrodes. Therefore, the easy processing, high photosensitivity, high on/off ratio and low energy consumption of the polymer photodetectors based on the asymmetrical electrodes have revealed the promising potential of the coplanar symmetrical electrodes in the field of photoelectric devices.

5.1 Introduction

Photodetectors, converting light signals into a voltage or current, have been widely used in imaging, spectroscopy, fibre-optic communications and time-gated distance measurements.[1-3] Recently, organic polymer photodetectors have become increasingly attractive for detecting applications because they can be integrated into conventional silicon based electronics on flexible, large-area substrates, and can be processed from the solution phase using established techniques such as spin casting, spray coating and layer-by-layer deposition.[1, 3-6]

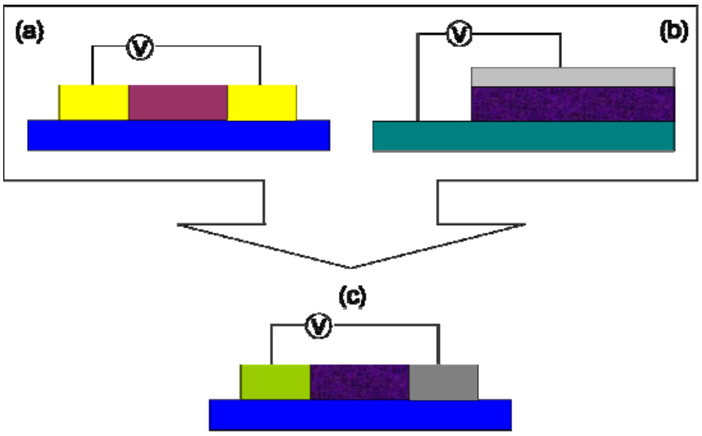

Figure 5.1 Structural models of (a) coplanar photoconductor with two symmetrical electrodes, (b) sandwich photodiode with two asymmetrical electrodes (one is transparent), (c) coplanar photodiode with two asymmetrical electrodes.

There are two different types of polymer photodetectors, namely photoconductors and photodiodes as presented in the Figure 5.1(a) and (b).[3, 7] Typically, polymer photoconductors (Figure 5.1a) employ two identical coplanar electrodes coated with a semiconducting polymer layer.[3, 8, 9] The advantages of this device structure consist in easy processing, low fabrication cost and effective light absorption given that the photoactive material is directly exposed to the light. Under illumination, the conductance of the semiconductor layer increases due to a prolonged persistence time.[3] The difference of the conductance under light versus dark indicates the light intensity. Nevertheless, the disadvantages of the photoconductors mainly include the slow response speed and high operation voltage.[10, 11] The second type of polymer photodetectors is the photodiode, which is normally fabricated in a sandwich structure as illustrated in Figure 5.1(b) with two different electrodes where at least one is transparent.[3, 12-14] Although the persistence, determined by the electron-hole pair recombination time, can be efficiently delayed in the sandwich structure because of the formation of a built-in potential, the processing is relatively complicated and light consumption is unavoidable due to the absorption by the transparent electrode.[3, 14-16]

Another requirement for the photodetectors is the low energy consumption, which means that the photodetector needs to be conducted at a low working potential. In this case, the effect of the contact resistance between the electrodes and photoactive materials is becoming remarkable. Graphene was selected as the hole transport electrode because of its high carrier injection efficiency to organic materials, such as P3HT and pentacene, which has been demonstrated in organic field effect transistors (OFETs).[17-19] For the electron transport electrode, titanium was employed according to its good chemical stability and proper energy level of the conduction band. Therefore, the coplanar asymmetrical graphene-titanium electrodes (Figure 5.1c) were proposed to fulfill the requirements of low light consumption, high photosensitivity and low energy consumption. Additionally, the fabrication of the coplanar asymmetrical graphene-titanium electrodes (AGTE) only involves evaporation and oxygen plasma etching technologies, being practical for producing on arbitrary substrates. Based on such a patterning technology, many other asymmetrical electrodes with the channel length less than 1 micrometer can also be easily fabricated. This qualifies for the fundamental and application study of the coplanar asymmetrical electrodes in the field of photoelectric devices.

5.2 Fabrication of graphene-titanium electrodes

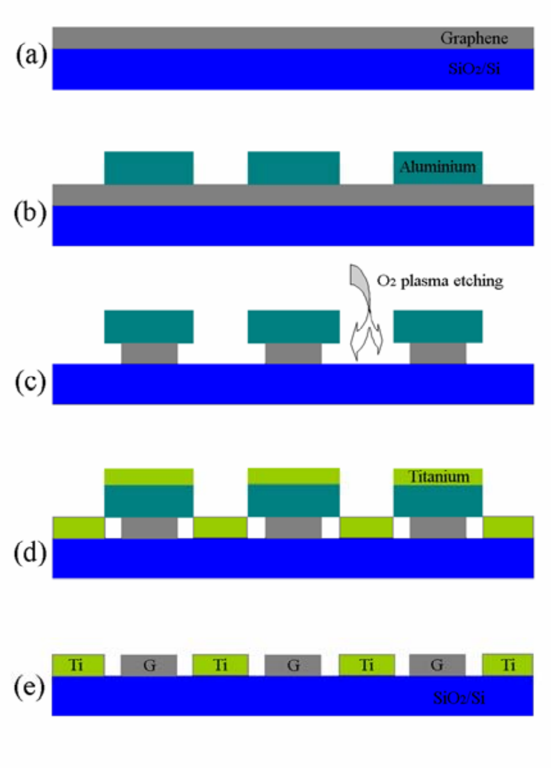

Scheme 5.1 Schematic illustration of the fabrication process of the AGTE. (a) graphene film was pyrolyzed from GO. (b) Patterned aluminum was evaporated to serve as the sacrificial mask. (c) Long-time oxygen plasma etching of the graphene film. (d) Deposition of titanium electrodes directly on the etched film. (e) Patterned AGTE was obtained after washing away the sacrificial aluminum.

The fabrication process of coplanar asymmetrical electrodes with narrow gaps is illustrated in Scheme 5.1. First, a GO dispersion was spin-coated on a SiO_2/Si substrate from GO solution and then thermally annealed at 1000 ^{o}C for 30 min to render the RGO film electrically conductive (Scheme 5.1a). The sheet resistance of the RGO film is about 500 Ohm/square, which was measured by a standard four point-probe system with a Keithley 2700 Multimeter (probe spacing: 0.635 mm, R_s = 4.5324 × V/I). To define the graphene patterns, aluminum patterns were thermally evaporated through a homemade mask (Figure 5.2a) under vacuum on the graphene film (Scheme 5.1b). Subsequently, the silicon/graphene/aluminum substrate was exposed to an oxygen plasma to remove the graphene regions not covered by the aluminum. The oxygen plasma etching was carried out under the rf power of 300 W with an oxygen flow of 20 sccm. It was found that 2 min of oxygen plasma etching is enough to eliminate the exposed RGO film. Longer etching time can produce an undercut along the edges of the aluminum patterns (Scheme 5.1c). After 3 min of oxygen plasma etching, a 40 nm thick titanium layer was evaporated through another homemade mask (Figure 5.1b) on the top of the aluminum patterns (Scheme 5.1d). Finally, the asymmetrical electrodes with graphene-titianium (Gr-Ti) patterns, alternately arranged on the silicon substrate, were obtained after removal of the pre-deposited sacrificial aluminum by immersing the substrate in a 5 % HNO_3 solution.

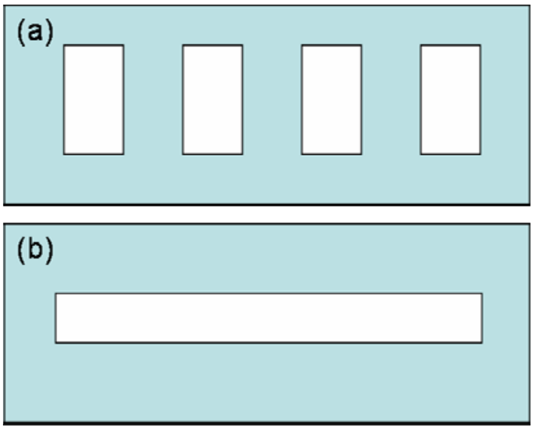

Figure 5.2 Home made masks for pattern the asymmetrical Graphene-Titanium electrodes. Mask (a) is for the evaporation of aluminium and (b) is for the evaporation of titanium.

Two homemade masks for the fabrication of the coplanar AGTEs are shown in Figure 5.2. The top mask (Figure 5.2a, four 1 mm × 2 mm rectangular holes) is used to define the graphene electrodes via depositing sacrificial aluminum patterns. After the oxygen plasma etching, the bottom mask (Figure 5.2b, one 1 mm × 7 mm rectangular hole) is employed to deposit titanium layer. Six Gr-Ti electrodes can be fabricated based on our masks after removing the sacrificial aluminum.

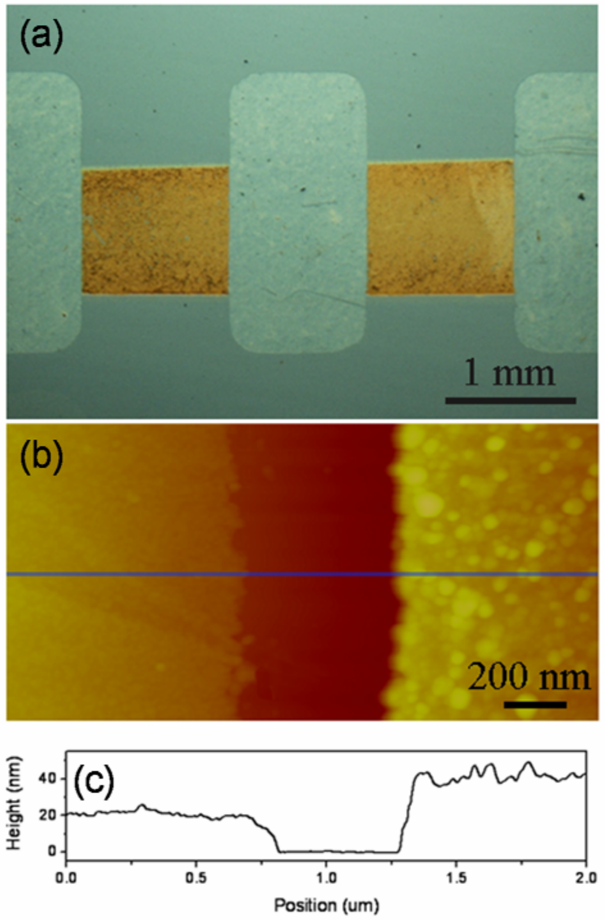

Figure 5.3 (a) OM image of AGTE with white rectangles are graphene and yellow squares are titanium, respectively. (b) AFM image of the edge of the graphene-titanium electrodes, with a channel length of ~ 500 nm. (c) Height profile along the line in (b), showing a narrow channel etched down to the underlying SiO_2/Si substrate.

The patterned coplanar AGTE were characterized by means of OM and AFM images as shown in Figure 5.3. Apparently, the graphene electrodes (white, ~ 1 mm × 2 mm rectangles) and titanium electrodes (yellow, ~ 1 mm × 1 mm squares) are alternately patterned on the silicon substrate (Figure 5.3a). The sharp and regular contact edges can be clearly seen from the AFM image (Figure 5.3b). Therefore, the areas exposed to the oxygen plasma are completely etched away, while those areas protected by aluminum survive during the processing. The formation of the gaps between graphene and titanium patterns is due to the undercut of the graphene under the aluminum patterns. A channel length of ~ 500 nm between graphene and titanium electrodes was produced after 3 min of oxygen plasma etching. The corresponding height profile (Figure 5.3c) along the line in Figure 5.3(b) indicates the complete etching of the graphene film down to the underlying silicon substrate.

It is noteworthy that, by this method, many other asymmetrical electrodes can also be fabricated, such as graphene-gold and graphene-silver. For the application of photodetectors, the electron collecting electrode should possess a much lower work function. Although silver and aluminum are conventionally used in organic photovoltaic devices for the collection of electrons, the formation of the thin oxide layers such as Ag_2O and Al_2O_3 on the electrodes surface during the wet chemical process will result in a loss of the function in collecting electrons.[18-20] However, titanium, with the work function of -4.3 eV, is suitable for the collection of electrons from the P3HT layer.[21]

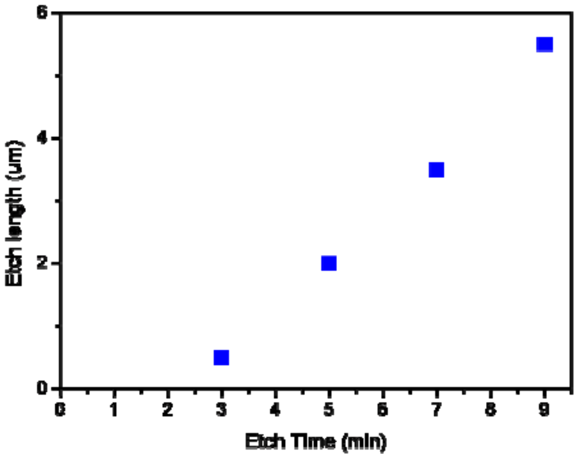

Figure 5.4 The rate of the oxygen etching of the reduced graphene oxide film.

In the fabrication process, once the exposed graphene film is etched away by the oxygen plasma, the undercut will occur with a constant speed. It was calculated that the lateral etching rate of graphene film under the aluminum patterns is of ~ 10 nm/s with 20 sccm O_2 flow, 300 W rf power. The length of the as-fabricated Gr-Ti channel (the distance from graphene to titanium electrode) as the function of etching time is shown in Figure 5.4. Thus, the channel length can be easily adjusted by controlling the plasma etching time. Together with the easy fabrication and the feasibility of large scale processing, such a fabrication strategy is supposed to be promising to pattern nanometer-sized gaps for nano-devices.*[22]*

5.3 Asymmetrical electrodes for photodetectors.

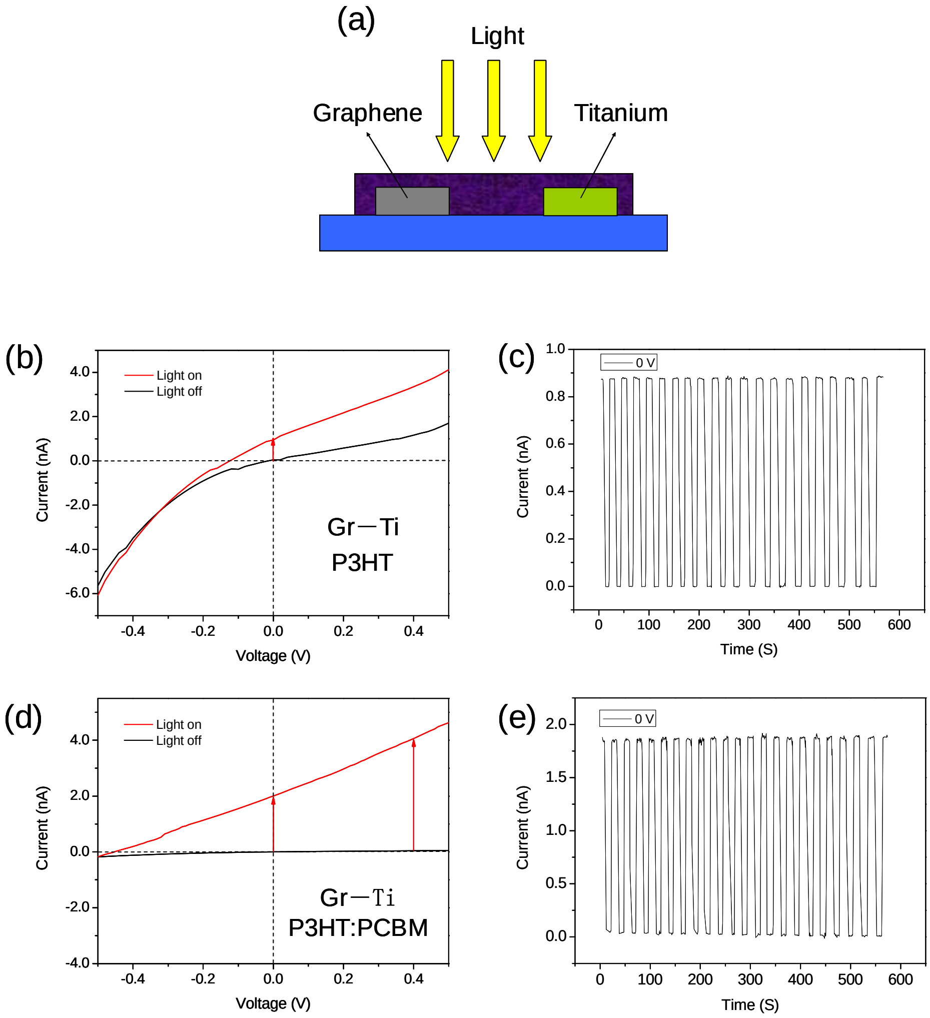

Figure 5.5 (a) The model of the asymmetrical graphene-titanium electrodes based phtodetector. (b) I–V characteristics of the AGTE based photodetector with P3HT as the photo sensitive material. (c) The on/off characteristics of a P3HT photodetector at 0 V. (d) I–V characteristics of the AGTE based photodetector with a blend of P3HT:PCBM as the photo sensitive material. (e) The on/off characteristics of the P3HT:PCBM photodetector at 0 V.

To examine the feasibility of the as-fabricated coplanar AGTEs in polymer photodetectors, P3HT and a blend of P3HT with PCBM were used as photosensitive materials. In a typical experiment, the substrate with the asymmetrical Gr-Ti electrodes was firstly treated with HMDS vapor by performing the same method as mentioned in chapter 4. Subsequently, the substrate was moved to a nitrogen filled glove box for the device fabrication and measurement. The chloroform solution of P3HT (5 mg/mL, 4002-E, Rieke Metals, Inc.) or a blend of P3HT (5 mg/mL) and PCBM (4 mg/mL, Aldrich 684430) was spin-coated at 2000 rpm for 40 s on the top of the HMDS modified AGTE and then annealed at 120 ^{o}C for 10 min. The photodetectors were measured in a glove box with a Keithley SCS 4200 semiconductor characterization system. The light equipped on a Nikon SMZ1000 microscope was directly used as the light source to switch the photodetector between the on and off. The light intensity for switching was ~ 20 mW/cm^2.

Typical I-V characteristics of P3HT photodetectors based on the AGTE are shown in Figure 5.5(b). The I-V curve in the dark shows an obvious diode property, which is due to the adoption of the asymmetrical electrodes. Under illumination, the I-V curve moves far away from the origin (0,0). Like a microphotovoltaic cell, the AGTE based photodetector shows an open circuit voltage (V_{oc}) of 0.12 V and a short circuit current (I_{sc}) of 0.98 nA (Figure 5.5b). Therefore, the large difference of the currents in dark and under illumination around the origin (0,0) allows the device to be performed at very low bias voltage, resulting in a low energy consumption. Figure 5.5(c) reveals the on/off characteristics at 0 V bias. The current of the device is rather low in the dark, however, it jumps sharply by more than 3 orders of magnitude upon irradiation (20 mW/cm^2), indicating a high photosensitivity. Switching the shielded light alternately on and off causes the current of the devices to exhibit two distinctively steady states: the “low” current state in the dark and the “high” current state in the light as shown in Figure 5.5(c).

In order to further improve the photosensitivity of the polymer photodetector, PCBM was introduced as electron acceptor material, which could promote the dissociation efficiency of the hole-electron pairs (excitons) at the interface of the P3HT:PCBM.*[23-26]* The performance of the P3HT:PCBM photodetector based on the as-fabricated AGTE is presented in Figure 5.5(d) and (e). The I–V characteristic under illumination (Figure 5.5d) also displays a typical photodiode character with the V_{oc} of 0.25 V and I_{sc} of 2.0 nA. Apparently, both the V_{oc} and the I_{sc} are higher than those of the P3HT photodetectors due to a more efficient dissociation of the excitons into free electrons and holes, resulting in a high photosensitivity when the light is switched on and off (Figure 5.5e).

5.4 Symmetrical electrodes for photodetectors.

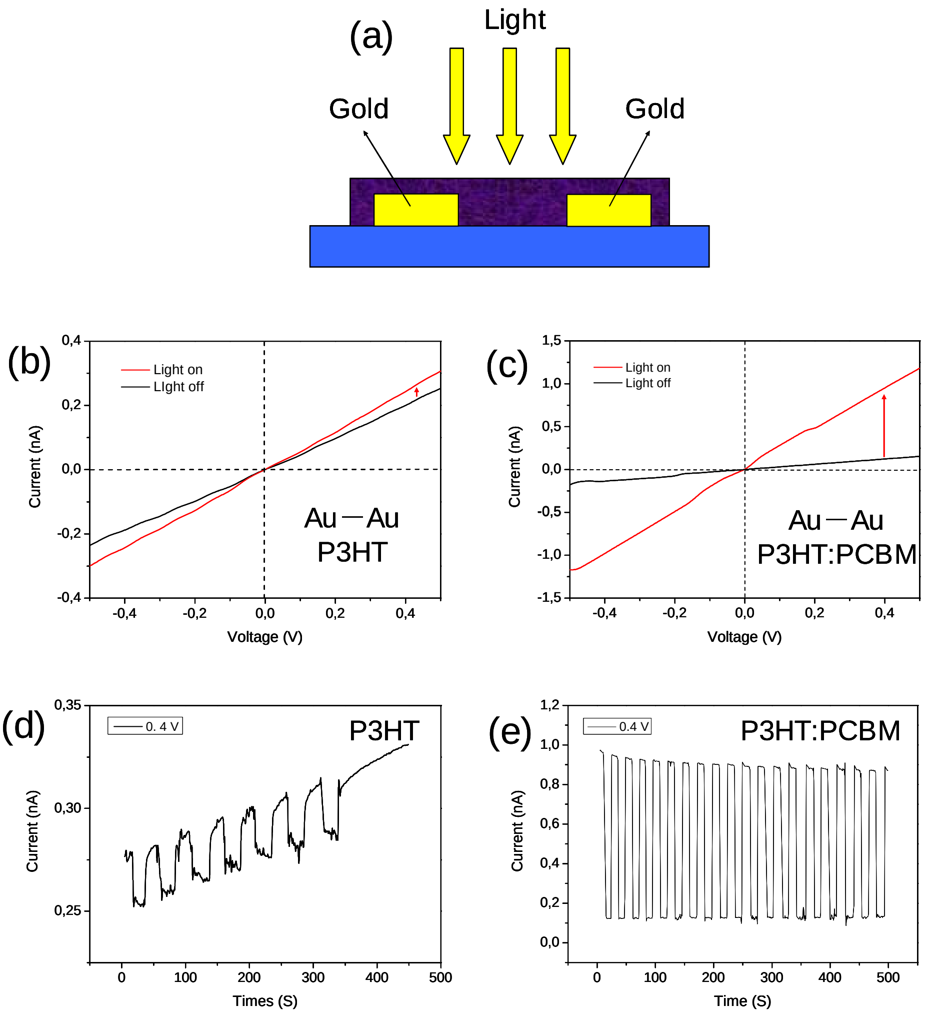

Figure 5.6 (a) The model of the symmetrical electrode based phtodetector. (b)

I–V characteristics of the symmetrical gold electrodes based photodetector with P3HT as the photo sensitive material. (c) I–V characteristics of the P3HT:PCBM photodetector with symmetrical gold electrodes. (d) The on/off characteristics of the P3HT photodetector at 0.4 V. (e) The on/off characteristics of the P3HT:PCBM photodetector at 0.4 V.

To gain an in-depth understanding of the influence of asymmetrical electrodes on the performance of photodetectors, two reference devices based on symmetrical gold contacts with a channel length of 5 μm were investigated (Figure 5.6a). As indicated in Figure 5.6(b) and (c), the diode properties were not observed. In this way, a high applied bias voltage is required to achieve efficient exciton dissociation. However, the applied bias voltage can also exert an influence on the background current. For instance, the I-V curves of P3HT photodetector performed at 0.4 V bias show a small variations between the conditions in the dark and under the light (Figure 5.6b). The photocurrent and the dark current are of the same order and the on/off ratio is less than 2. Additionally, the current of the photodetector increases and decreases more slowly than the P3HT photodetector based on the AGTEs when the light is turned on and off (Figure 5.5c, 5.6d). This can be attributed to the inefficient dissociation of exciton to free hole and electron in P3HT under illumination.[10, 23] After introducing the electron acceptor, PCBM, both the on/off ratio and the photo-response speed are improved as demonstrated in Figure 5.6(e). The on/off ratio of the P3HT:PCBM photodetector at 0.4 V is ~ 10, more than 5 times higher than that of the pure P3HT photodetector (Figure 5.6d). However, the on/off characteristic is not reversible, with a decreasing on-current along with repeating on/off operation (Figure 5.6e). The reason of the degradation of the on-current is still not clear.

5.5 Photodetectors in sandwich structure

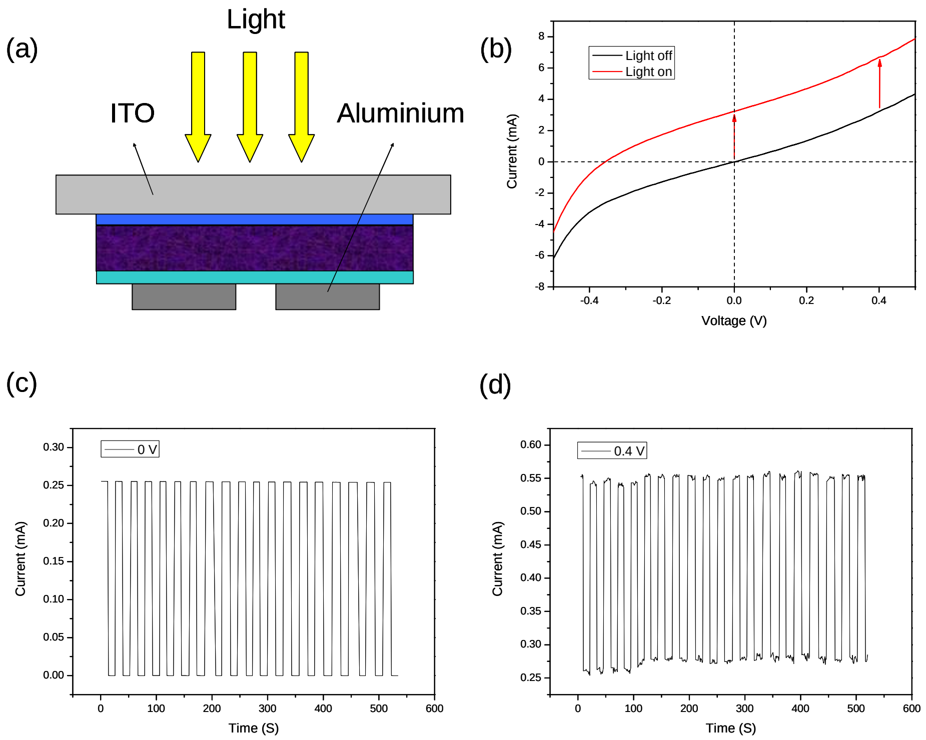

Figure 5.7 (a) Model of the sandwich structure of ITO-Al based P3HT:PCBM photodetector. (b) I–V characteristics of the AGTE based photodetector with P3HT:PCBM as the photosensitive material. (c,d) The on/off characteristics of the P3HT:PCBM photodetector with the applied bias voltage of 0V and 0.4 V, respectively.

Up to now, the highly sensitive polymer photodetectors are normally fabricated in the sandwich structure with a combination of PCBM as the photosensitive materials (Figure 5.7a). In a typical experiment, the transparent electrode ITO was firstly cleaned by an oxygen plasma and then a 50 nm thick conducting PEDOT:PSS layer was spin coated. Then the substrate was dried at 150 ^{o}C for 15 min in air and moved into a glove box. The dichlorobenzene solution comprising P3HT (10 mg/mL) and PCBM (8 mg/mL) was spin coated at 700 rpm on top of the PEDOT:PSS layer. After a slow drying process of the active layer, ~ 30 nm thick ZnO nanoparticles were spin coated on the active materials from the n-butanol solution. Finally, a 100 nm thick aluminum layer was evaporated through a mask onto the surface to form the cathode.

Post annealing was carried out in the glove box at 140 °C for 10 min. The I-V curves in the dark and under light were measured as presented in Figure 5.7(b). The photodetector exhibits similar performance to the P3HT and P3HT:PCBM photodetectors based on the as-fabricated AGTE, which further proves the essential role of the asymmetrical electrodes. The on/off behaviour of the P3HT:PCBM photodetector at 0 V and 0.4 V as revealed in Figure 5.7(c) and (d), respectively, shows a similar performance to our photodetectors based on the coplanar asymmetrical electrodes.

Table 5.1. Comparison of the on/off ratio of the P3HT and P3HT:PCBM blend photodiodes based on the coplanar asymmetrical and symmetrical electrodes.

Electrodes	Materials	On/off		Photoresponse speed
		0 V	0.4 V	
Asymmetrical electrodes	P3HT	> 1000	~ 3	fast
	P3HT:PCBM	> 1000	~ 50	fast
Symmetrical electrodes	P3HT	—	~1.2*	slow
	P3HT:PCBM	—	~(10-10000)**	fast

** The value is calculated from Figure 5.6(b) with the gap length of 5 um. Similar results also obtained based on the 100 nm gap length symmetrical gold electrodes and graphene electrodes.*[10, 23] *** The value is calculated from Figure 5.6(c) with the gap length of 5 um. The on/off ratio highly depends on the width of the gap. High on/off ratio (~10000) can be obtained when the gap length is in the range of 75 — 100 nm,*[23] *and on/off ratio decreased sharply to ~ 8 when the width increased to 5 um.*

The performances of the P3HT and P3HT:PCBM photodetectors based on coplanar symmetrical graphene-titanium electrodes and coplanar symmetrical gold electrodes are summarized in Table 5.1. The advantages of the AGTE based photodetectors are high photosensitivity, high on/off ratio and low energy consumption. Together with the easy processing, the feasibility of large scale fabrication and improved light absorption behavior. It is proposed that the coplanar asymmetrical electrodes will be very promising in the photoelectric devices.

5.6 Working principle

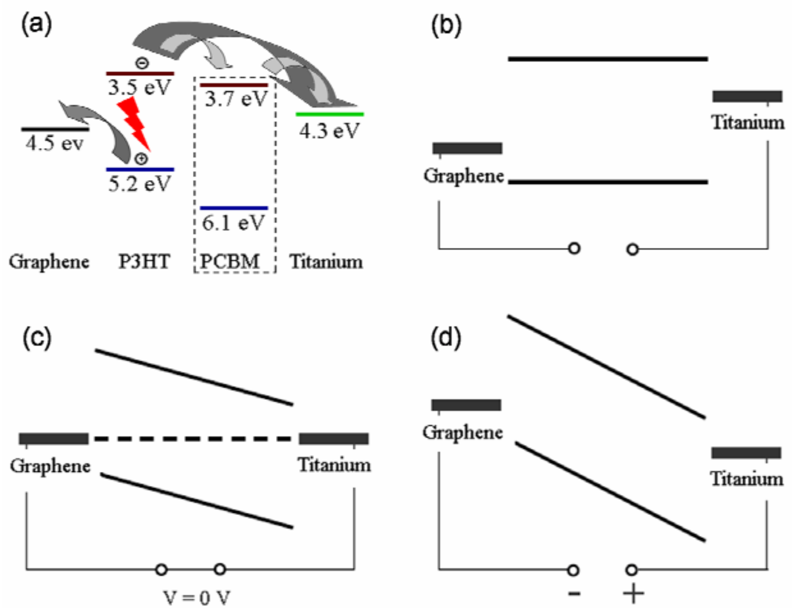

Figure 5.8 (a) A schematic representation of charge transfer and transport as an energy level diagram. (b-d) Simplified principles of device function for organic semiconducting layers between two metallic electrodes: (b) open circuit (flat band) condition, (c) short circuit condition, and (d) reverse bias. Band bending effects at the ohmic contacts are neglected.

We attribute the improvement of the polymer photodetector based on coplanar AGTE to the "build-in" potential, which is governed by the difference of work functions between two electrodes.*[15, 18, 27, 28]* An internal electrical field in the organic semiconductor can effectively dissociate the excitons into holes and electrons and then quickly repel them to the opposite electrodes. A schematic representation of charge transfer and transport as an energy level diagram is presented in Figure 5.8(a). The work function of graphene electrode was presumed to be 4.5 eV. To simple the charge transfer pathway, the energy band diagrams are schematized to one LUMO and one HOMO as shown in Figure 5.8(b), which refers to the point of I_{sc}=0 under illumination with the electrons and holes randomly diffused in the polymer layer (Figure 5.8a, c). When the external circuit is shorted, the energy levels of the graphene and titanium electrodes are rectified to the same value and an internal "build-in" electric field is produced in the photoactive layer (Figure 5.8c). Once the holes and electrons are generated under the illumination, the holes and electrons in the polymer layer can be expected to drift to the opposite electrodes by this "build-in" potential, producing a light-on current of 1.0 nA (P3HT, Figure 5.5a) and 2.3 nA (P3HT:PCBM, Figure 5.5c), respectively. When a reverse bias is applied on the photodiode, the internal "build-in" electric field is increased (Figure 5.8d), leading to an enhanced light-on current to 3.5 nA for P3HT and 7.0 nA for the P3HT:PCBM bend at the bias voltage of 0.4 V (Figure 5.5a, c).

5.7 Conclusion

In summary, we have demonstrated a novel technology for the fabrication of coplanar asymmetrical electrodes with narrow channels. The polymer photodetectors based on the patterned Gr-Ti electroders result in an improved photosensitivity because of the presence of a "build-in" potential originating from the different electrodes, which can efficiently dissociate the excitons into holes and electrons and then quickly repel them to the opposite electrodes. The "build-in" potential makes the asymmetrical electrodes based photodetectors exhibit very high photosensitivity at a low bias voltage, which is much superior to symmetrical electrode based photodetectors, where only the external bias gives the drive force to repel the carriers to the electrodes. The easy processing, high photosensitivity, high on/off ratio and low energy consumption have revealed a promising potential of the coplanar asymmetrical electrodes in the field of photoelectric devices.

References

[1] X. Gong, M. H. Tong, Y. J. Xia, W. Z. Cai, J. S. Moon, Y. Cao, G. Yu, C. L. Shieh, B. Nilsson, A. J. Heeger, *Science* **2009**, *325*, 1665.

[2] G. Konstantatos, I. Howard, A. Fischer, S. Hoogland, J. Clifford, E. Klem, L. Levina, E. H. Sargent, *Nature* **2006**, *442*, 180.

[3] G. Konstantatos, E. H. Sargent, *Nat. Nanotechnol.* **2010**, *5*, 391.

[4] G. A. O'Brien, A. J. Quinn, D. A. Tanner, G. Redmond, *Adv. Mater.* **2006**, *18*, 2379.

[5] B. Pradhan, K. Setyowati, H. Y. Liu, D. H. Waldeck, J. Chen, *Nano Lett.* **2008**, *8*, 1142.

[6] S. Liu, J. M. Li, Q. Shen, Y. Cao, X. F. Guo, G. M. Zhang, C. Q. Teng, J. Zhang, Z. F. Liu, M. L. Steigerwald, D. S. Xu, C. Nuckolls, *Angew. Chem. Int. Ed.* **2009**, *48*, 4759.

[7] S. Wan, J. Guo, J. Kim, H. Ihee, D. L. Jiang, *Angew. Chem. Int. Ed.* **2009**, *48*, 5439.

[8] V. Sukhovatkin, S. Hinds, L. Brzozowski, E. H. Sargent, *Science* **2009**, *324*, 1542.

[9] H. Y. Chen, M. K. F. Lo, G. W. Yang, H. G. Monbouquette, Y. Yang, *Nat. Nanotechnol.* **2008**, *3*, 543.

[10] Y. Cao, S. Liu, Q. Shen, K. Yan, P. J. Li, J. Xu, D. P. Yu, M. L. Steigerwald, C. Nuckolls, Z. F. Liu, X. F. Guo, *Adv. Funct. Mater.* **2009**, *19*, 2743.

[11] R. J. Waltman, J. Pacansky, C. W. Bates, *Chem. Mater.* **1993**, *5*, 1799.

[12] P. Peumans, V. Bulovic, S. R. Forrest, *Appl. Phys. Lett.* **2000**, *76*, 3855.

[13] T. Rauch, M. Boberl, S. F. Tedde, J. Furst, M. V. Kovalenko, G. N. Hesser, U. Lemmer, W. Heiss, O. Hayden, *Nat. Photonics* **2009**, *3*, 332.

[14] N. C. Greenham, X. G. Peng, A. P. Alivisatos, *Phys. Rev. B* **1996**, *54*, 17628.

[15] Y. H. Chang, C. M. Liu, Y. C. Tseng, C. Chen, C. C. Chen, H. E. Cheng,

Nanotechnology **2010**, *21*, 225602.

[16] S. W. Clark, J. M. Harbold, F. W. Wise, *J. Phys. Chem. C* **2007**, *111*, 7302.

[17] S. P. Pang, H. N. Tsao, X. L. Feng, K. Mullen, *Adv. Mater.* **2009**, *21*, 3488.

[18] M. Y. Liu, C. H. Chang, C. H. Chang, K. H. Tsai, J. S. Huang, C. Y. Chou, I. J. Wang, P. S. Wang, C. Y. Lee, C. H. Chao, C. L. Yeh, C. I. Wu, C. F. Lin, *Thin Solid Films* **2010**, *518*, 4964.

[19] U. J. Kim, H. Bin Son, E. H. Lee, J. M. Kim, S. C. Min, W. Park, *Appl. Phys. Lett.* **2010**, *97*, 032117.

[20] Y. H. Zhou, H. Cheun, W. J. Potscavage, C. Fuentes-Hernandez, S. J. Kim, B. Kippelen, *J. Mater. Chem.* **2010**, *20*, 6189.

[21] S. Cho, K. Lee, A. J. Heeger, *Adv. Mater.* **2009**, *21*, 1941.

[22] T. Li, W. P. Hu, D. B. Zhu, *Adv. Mater.* **2010**, *22*, 286.

[23] H. F. Zhu, T. Li, Y. J. Zhang, H. L. Dong, J. S. D. Song, H. P. Zhao, Z. M. Wei, W. Xu, W. P. Hu, Z. S. Bo, *Adv. Mater.* **2010**, *22*, 1645.

[24] I. W. Hwang, D. Moses, A. J. Heeger, *J. Phys. Chem. C* **2008**, *112*, 4350.

[25] M. S. Arnold, J. D. Zimmerman, C. K. Renshaw, X. Xu, R. R. Lunt, C. M. Austin, S. R. Forrest, *Nano Lett.* **2009**, *9*, 3354.

[26] G. Yu, J. Wang, J. McElvain, A. J. Heeger, *Adv. Mater.* **1998**, *10*, 1431.

[27] B. Zimmermann, M. Glatthaar, M. Niggemann, M. Riede, A. Hinsch, *Thin Solid Films* **2005**, *493*, 170.

[28] T. Mueller, F. N. A. Xia, P. Avouris, *Nat. Photonics* **2010**, *4*, 297.

Chapter 6

Extrinsic Corrugation Assisted Mechanical Exfoliation of Monolayer Graphene

It is the fact that graphene electrodes have exhibited promising advantages organic electronics. In this chapter, toward the requirements of low-cost and easy processing, an extrinsic corrugation assisted mechanical exfoliation process was described to directly fabricate ultra-large and patterned monolayer graphene on silicon substrates. It has been proved that a heat treatment of the graphite flake on the silicon substrate can make the underlayer graphene adapt to and take the shape of the rippled SiO_2 surface, resulting in the high yield of monolayer graphene after a reversely mechanical exfoliation. This exfoliation method, without any contamination, not only offers an ideal alternative for the scalable deposition of monolayer graphene on silicon substrates, but also provides a promising basic route for the construction of graphene based integrated circuits.

6.1 Introduction

Since the reports of the first isolation and observation of the exceptional electronic, mechanical and chemical properties, single layer graphene has attracted intense interest from both academic and industrial communities.[1-3] While the mechanical exfoliation method led to many exciting discoveries, several promising approaches have been reported for the preparation of monolayer graphene including solution exfoliation of graphite, [4, 5] epitaxial growth from SiC,[6, 7] reduction of graphene oxide,*[8-10]* and chemical vapor deposition (CVD) on metal surfaces.*[11-13]* Although the CVD growth method seems to be the most promising technique for the production of large-scale few-layer graphene films,*[13, 14]* this surface mediated process requires very high temperatures, not to mention the tedious additional steps involving transfer and etching.

Ultra-large monolayer graphene*[15-17]* and patterned graphene structures*[18-22]* constitute two important aspects for the graphene fabrication technology. A simple way to directly "print" high-quality graphene monolayers on insulating substrates from a graphite stamp would be particularly appealing for electronic applications. Covalent immobilization*[23, 24]* and electrostatic forces*[18, 25]* have been devised toward modification of mechanical exfoliation, with the aim to improve the yield of monolayer graphene or to achieve patterned graphene structures. Despite the success in deposition of graphene patterns over a large area, these procedures suffer from the low yield of monolayer production (< 10 %).*[18, 19, 26]* In this work, we will describe an extrinsic corrugation assisted mechanical exfoliation (ECAME) for the deposition monolayer graphene on silicon substrates. This strategy involves a thermal treatment of deposited graphite sheets on a silicon wafer in association with a tape peeling process. Our work discloses that underlayer graphene sheets can corrugate following the rough SiO_2 surface when the thick graphite flake is thermally annealed. Such a surface mediated extrinsic corrugation process thus can serve as the key driving force for deposition of monolayer graphene.

6.2 Deposition of graphene from graphite

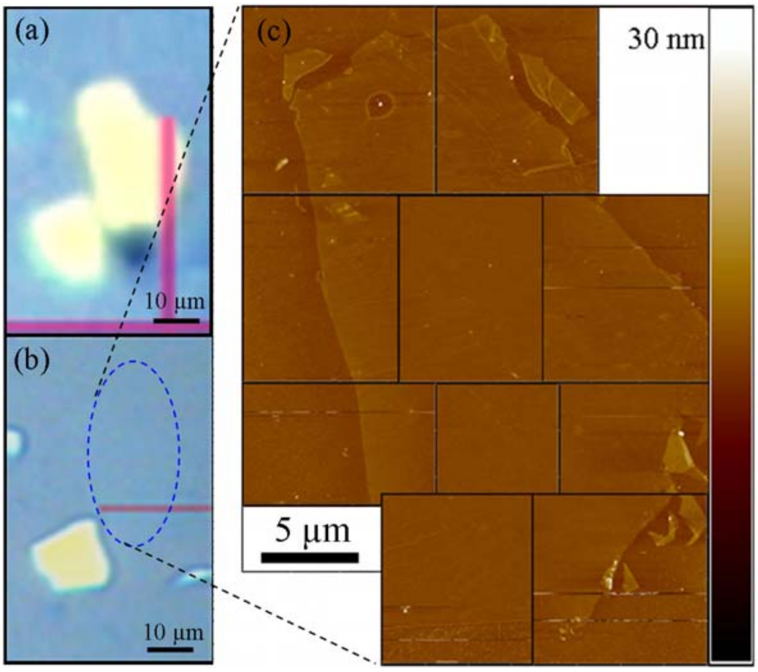

Figure 6.1 (a) The OM image of ~ 100 nm thick graphite flakes on silicon substrate after thermal annealing at 350 ^{o}C for 2 h. (b) The OM image of the same position after the reverse exfoliation using a wafer processing tape. (c) AFM images of the underlayer graphene left on the silicon substrate are recorded.

To test the feasibility of the ECAME process, a silicon substrate was firstly treated in an oxygen plasma and then graphite flakes with the lateral size of about tens of micrometers and thickness ranging from ~ 10 to ~ 100 nm were firstly transferred on it. In order to make the graphite flakes contact closely to the substrate, ethanol solution was used to rinse the substrate before the transferring. It was found that the graphite sheets could be closely attached to the silicon substrate after the evaporation of the solvent. Additionally, the graphite sheets should be thin enough (< 100 nm) because thin graphite flakes are more flexible and apt to keep a closely attaching to the substrate during the heat treatment. After the substrate/graphite flakes were thermally annealed at 350 ^{o}C for 2 h (Figure 6.1a), a peeling-off test (or namely reversely mechanically exfoliation) of the graphite flakes was carried out using a wafer processing tape. It was found that very thin graphene layers were left (Figure 6.1b), which were identified by AFM measurements as monolayer graphene (Figure 6.1c, Figure 6.2). Remarkably, the outline of the graphene completely coincides with that of the original graphite flake. For 20 successive experiments, the graphite flakes are found to be exfoliated only between the few bottom layers in close vicinity to the silicon substrate after the thermal treatment. In this respect, three repetitive exfoliations are sufficient to eliminate top layers of graphite flakes, leaving very thin graphene layers (1-3 layers) on the substrate. Furthermore, the graphene sheets produced by the ECAME process are much more stable than the ones obtained by conventional mechanical exfoliation and can not be removed by solvent washing or sonication, suggesting a strong interaction between graphene and substrate.

6.3 Extrinsic corrugation from silicon substrate

Theoretically, the successful deposition of graphene on a silicon substrate requires a comparatively large adhesion energy between graphene and SiO_2 (W_{G-S}) to overcome the adhesion energy between graphene layers (W_{G-G}) themselves,[19] in this way enabling single or few-layer graphene to be deposited after a reversely mechanical exfoliation. W_{G-S} is estimated to be much larger than W_{G-G}, thus transferring the monolayer or few layer graphene on silicon substrate is energetically most favorable via a stamping technique.[19] However, it is the fact that the adhesion energy between graphene and SiO_2 is strongly affected by the following two parameters: 1) The surface property of the substrate. It is calculated that graphene exhibits stronger adsorption on the O−terminated than on the Si−terminated surface. Thus the O−terminated surface can be more suitable for graphene deposition;[27] 2) The effective contacting area of graphene on the substrate. The SiO_2 surface, exhibiting a long range corrugation, is rougher than that of the graphite flake.[28-30] The adhesion energy of graphene-SiO_2 without the thermal treatment is estimated to be 6 meV/Å^2, which is much lower than the interlayer van der Waals interaction in graphite of 20 meV/Å^2.[28] Adapting corrugation of graphene on substrate surfaces is therefore expected to promote the adhesion between the graphene and the SiO_2. The yield of the monolayer graphene highly depends on the annealing temperature. For 350 °C treated samples, only the thin graphite flakes (< 100 nm) can be possibly exfoliated by the ECAME process. In contrast, high temperature (700 °C) treatment can be useful for the thick ones (~1 μm).

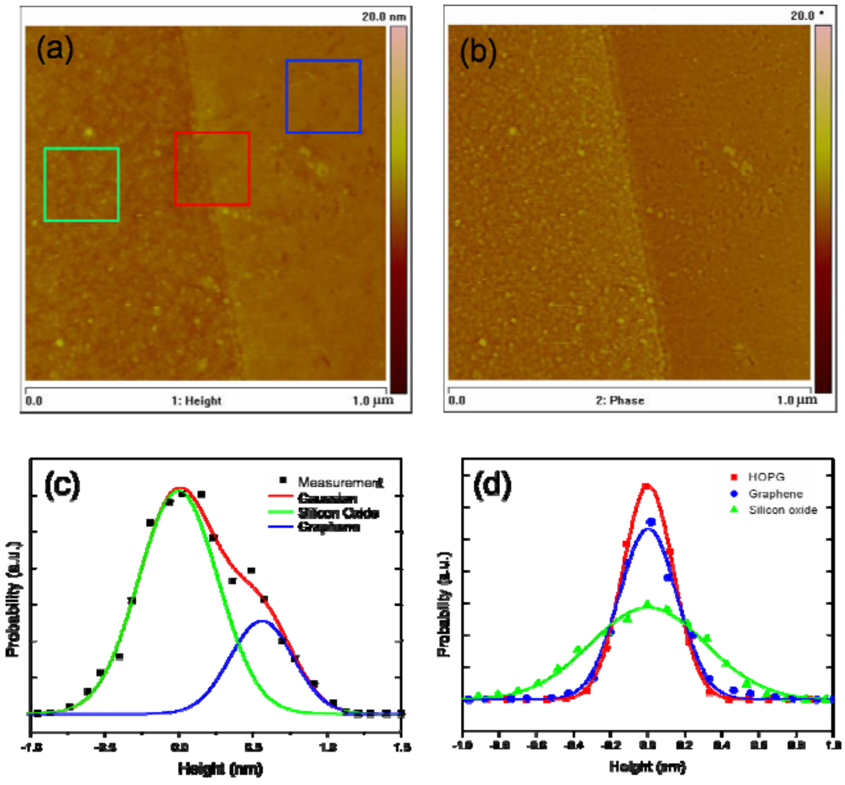

Figure 6.2 (a) AFM height image of single layer graphene on a silicon substrate (left: silicon oxide, right: graphene). (b) Corresponding phase image. (c) Height histogram acquired across the graphene–substrate boundary (red square). The data is fitted by two Gaussian distributions (solid green and blue lines, red line is sum), revealing the thickness of graphene to be around 0.60 nm. (d) The height histograms acquired on one graphite flake, monolayer graphene/SiO_2 and bare SiO_2, respectively (red square, blue rhombus, and green triangle). The histograms are well-described by Gaussian distributions.

In order to prove the extrinsic corrugation of the underlayer graphene after the thermal treatment, the roughness of a graphite flake, graphene on SiO_2 and the bare SiO_2 were evaluated by the AFM characterizations. Figure 6.2(a) shows a 1 μm × 1 μm AFM image of the edge of the graphene sheet (Figure 1.1c). A histogram acquired across the boundary (Figure 6.2c) reveals a mean film thickness of ~ 0.60 nm, which is in the range of reported values for monolayer graphene.*[28]* Figure 6.2(d) demonstrates the histogram of the height over one graphite flake, monolayer graphene/SiO_2 and bare SiO_2, respectively. The R_a (the arithmetic average of the roughness profile) of graphene on SiO_2 is about 0.13 nm, larger than that of the graphite surface (R_a = 0.10 nm,) and smaller than that of the SiO_2 surface (R_a = 0.24 nm). Thus, it can be concluded that the graphene monolayer deposited by the ECAME process is apt to follow the structure of the underlayer SiO_2, but there are still some areas suspending on the substrate.

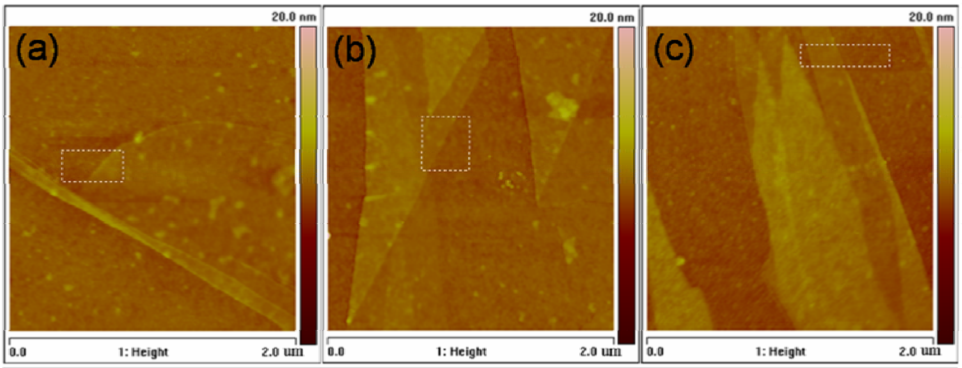

350 °C	500 °C	700 °C
Graphene/SiO_2 (nm)		
0.191/0.229	0.215/0.245	0.227/0.250
83%	87%	90%

Figure 6.3 AFM images and their corresponding roughness of graphene on a silicon substrate after thermal annealing at (a) 350 °C, (b) 500 °C, (c) 700 °C.

In fact, the corrugations widely exist on the deposited graphene monolayer, especially for the thermally annealed samples. To prove the evolutions of the morphology of the silicon supported graphene sheets after thermal treatment, the roughness of the graphene sheets annealed at different temperatures were examined by the AFM as illustrated in Figure 6.3. The monolayer graphene sheets were transferred on the silicon substrates by a mechanical exfoliation method. The subsequently thermal treatment of the samples was carried out in a horizontal tube oven filled with argon under a normal pressure. Apparently, the roughness of the graphene sheets is enhanced with the increase of the annealing temperature, indicating that the high temperature treatment is beneficial for the improvement of the contact between the graphene and the silicon substrate.

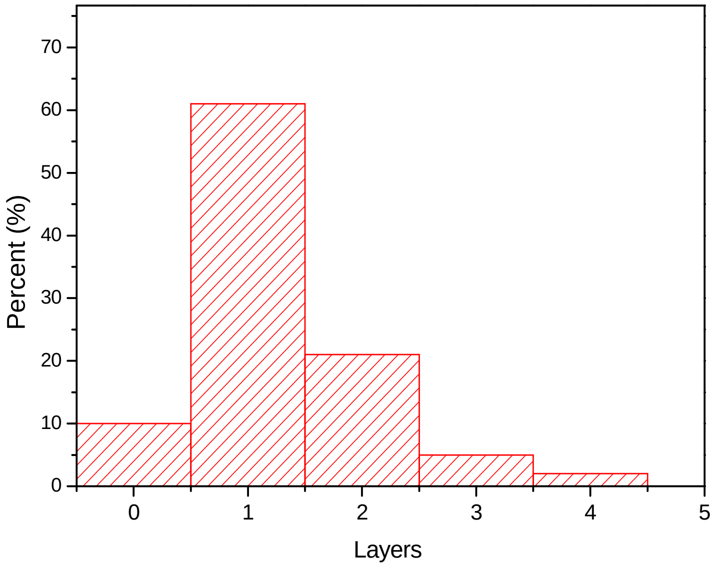

Figure 6.4 A calculated distribution of exfoliated graphene layers with different thickness.

Figure 6.4 demonstrates the thickness distribution of graphene layers calculated from the AFM measurement of 20 exfoliated graphene sheets. Remarkably, ~ 90 % of the area is covered by 1−3 layers of graphene. The other 10 % blank area is probably due to the contacting problem caused by contaminations on the silicon substrate (circular blank area in the top-left corner in Figure 1.1c) and the terrace structure of the graphite flakes (Figure 6.6). The high yield of monolayer graphenes (60 %) indicates that the exfoliation mainly occurs between the underlayer graphene and the top n-1 layers of a graphite flake.

6.4 Deposition of large graphene sheets on silicon

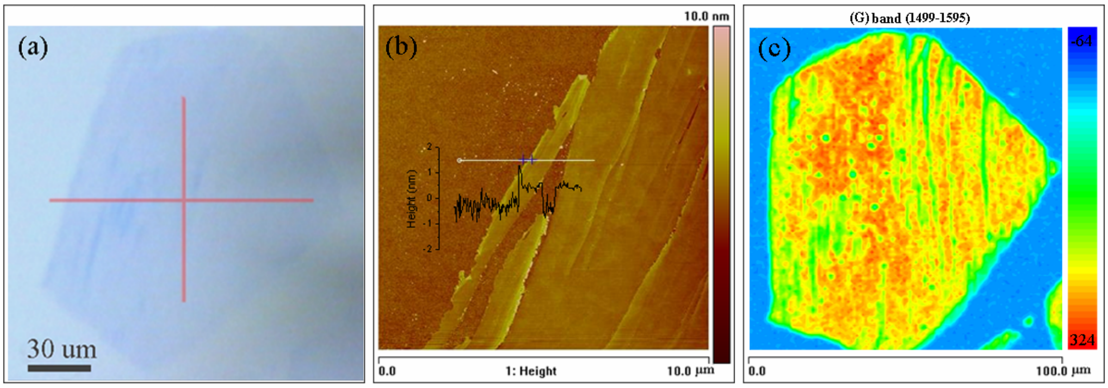

Figure 6.6 (a) OM of a big graphene sheet on silicon substrate with 300 nm thick SiO_2. (b) Corresponding AFM images and (c) Raman map (G band) of the graphene sheet in (a). The thickness of graphene sheets in (b) is ~ 0.70 nm.

Encouraged by the success in graphene deposition, we further developed the ECAME process to fabricate ultra-large graphene sheets on the silicon substrate. In this regard, a large graphite flake was subjected to a same thermal treatment on the silicon wafer. Although a thermal annealing at 350 ^{o}C enables one to fabricate graphene from thin graphite flakes (~ 100 nm), we find that a high temperature treatment for a thick graphite flake is required in order to gain sufficient adhesion energy to overcome the energy costs of the corrugation of the underlayer graphene. For instance, a thermal treatment at 700 ^{o}C is adopted for a ~ 1 μm thick and 100 μm × 100 μm large graphite flake. Figure 6.6(a) presents the OM image of the ultra-large graphene sheet (10,000 μm^2) obtained by the ECAME process. The corresponding AFM image (Figure 6.6b) on its edge indicates that the graphene is of monolayer nature (~ 0.70 nm in thickness), with strip-like structures. The G peak Raman map from 1499 cm^{-1} to 1595cm^{-1} (Figure 6.6c) shows the full coverage of the graphene is the area with light green color as shown in Figure 6.6(a).

For the exfoliation of ultra-large graphite flake, the first challenge is how to keep the large graphite flake closely contact to the substrate during the thermal annealing. Without doubt, an external pressure can help to improve the contacting property. Interestingly, in our fabrication, we have found that the low surface tension solvents, such as acetone, ethanol and ethanol, can be applied to promote the contact between graphite and substrate. After dropping ethanol solvent on the silicon substrate, big graphite flaks were then transferred on the silicon substrates immediately. After the evaporating of the solvent, the big graphite flake can be closely contacted to the silicon substrate.

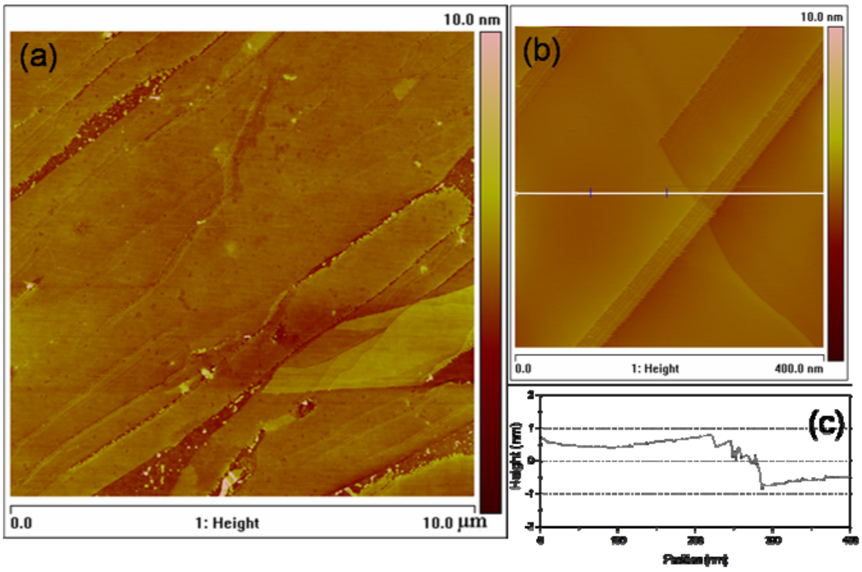

Figure 6.6 (a) AFM image of the OM of a big graphene sheet on silicon substrate with 300 nm thick SiO_2. (b) STM images of the HOPG surface. (c) Height profile a long the line in (b).

For the ultra-large exfoliated graphene sheets, strip-like morphologies were always observed in the AFM images (Figure 6.5b and Figure 6.6a). It was found that the strip structure is a copy of the surface morphology of the surface of HOPG or graphite flake (Figure 6.6b). It is the fact that both HOPG and natural graphite flakes are polycrystalline graphites, with many small single graphite crystals inside. Thus terrace structures will be formed at the boundary (Figure 6.6c). The height of the terraces is from nanometers to hundreds of nanometers, which explains why graphite surface can not fully attached to the silicon substrates..

6.5 Deposition of graphene patterns on silicon

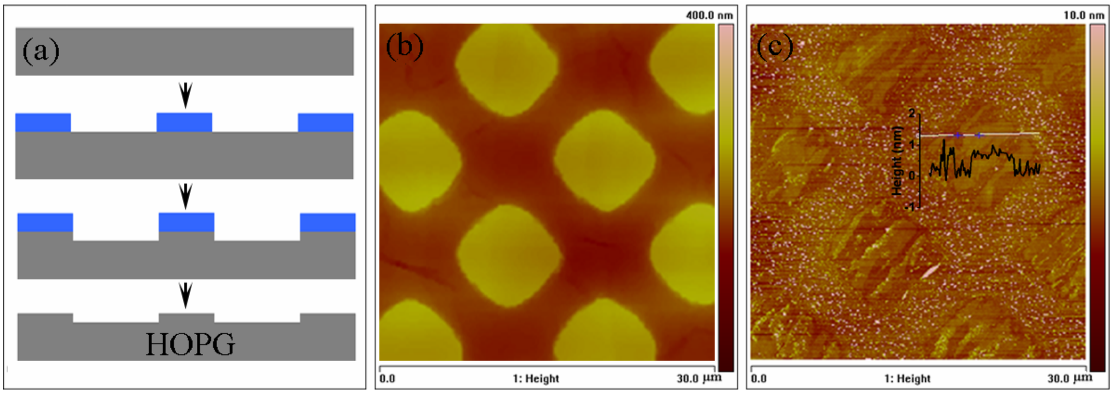

Figure 6.7 (a) The process for preparing the graphite stamp via oxygen etching. (b) AFM image of the graphite stamp. (c) AFM image of the patterned graphene monolayer from the graphite stamp. The thickness of graphene sheets in (c) is ~ 0.70 nm.

To broaden the scope of graphene fabrication by emphasizing the facile processing/handling, repeatability and cost-effectiveness, the ECAME approach can be further employed to pattern graphene layers on a silicon substrate, which holds promise for direct electronic applications. As a typical example, a graphite stamp was firstly created on the HOPG surface as illustrated in Figure 6.7(a). A 2000 mesh copper grid was used as the mask to deposit 30 nm thick aluminum patterns as a protecting layer. After 10 min oxygen plasma etching and removal of the sacrificial layer by immersing in a dilute HNO_3 solution, ~ 100 nm thick, ~ 8 μm × 8 μm square-shaped graphite pillars were formed (Figure 6.7b). Afterwards, the patterned HOPG stamp was pressed on a pre-cleaned silicon substrate and treated at 700 °C for 2 h. Finally, after the vertical removal of the HOPG stamp, patterned graphene monolayer squares (Figure 6.7c) with an average lateral size of ~ 8 μm and a thickness of ~ 0.70 nm were successfully generated on the silicon substrate. Thereby, such patterned graphene structures allow one to directly investigate its electronic properties in devices.

6.6 Quality of the deposited graphene layer

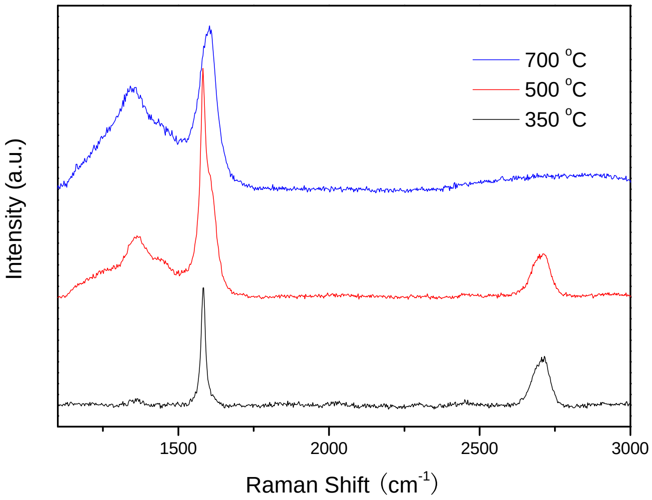

Figure 6.8 Raman spectra of the graphene sheets fabricated by the ECAME process with different annealing temperatures.

The Raman spectra of the as-prepared graphene sheets were measured by a Renishaw spectrometer under the laser excitation of 532 nm at room temperature. The D, G and 2D peaks are located at 1350 cm^{-1}, 1580 cm^{-1}, and 2688 cm^{-1}, respectively. In graphene, the G and 2D peaks are due to the doubly degenerate zone center E_{2g} mode and the second order of zone-boundary phonons. For the low temperature treated sample (350 ^{o}C), the weak intensity of the D peak highlights the lower amount of defects within the graphene sheets obtained with our fabrication method.[13, 31] However, the intensity of the D band is increasing with the increase of the annealed temperature. The appearance of the D band in the high temperature processed sample is possibly attributed to the destruction of the graphene structure. We propose that the presence of oxygen on the silicon wafer surface can produce the oxidation of graphene or bonding between graphene and the substrate.

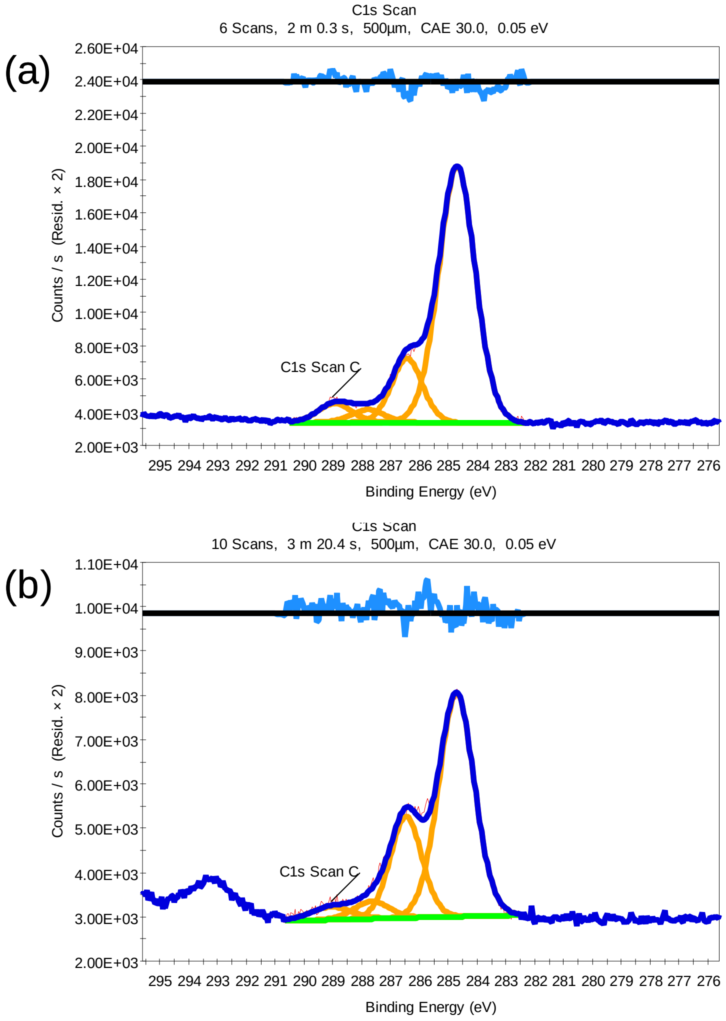

Figure 6.9 XPS spectra of the graphene sheets fabricated by the ECAME process with different annealing temperatures. (a), 350 °C; (b) 700 °C.

Figure 6.9 shows the C 1s XPS spectra of graphene sheets fabricated by the ECAME process at 350 °C and 700 °C respectively. Four types of carbon with different chemical states are observed, which appear at 284.5 eV (graphite, C–C/C=C), 286.6 eV (C–O), 287.8 eV (C=O), and 289.0 eV (O–C=O). Even at 350 °C annealing for 2 hours, a very low C–O peak intensity is still found in the exfoliated graphene sheets. With the increase of the annealing temperature, the content of the C–O bond is increased as shown in Figure 6.9(b). The strong intensity of the C–O bond is attributed to the oxidation of the graphene structure by the oxygen from the silicon substrate. It is interesting that the intensity of the C-O band of ECAME fabricated at 700 °C is stronger than that of thermally reduced GO. Therefore, the relatively strong C-O peak is possibly due to the bonding to the oxygen on the silicon surface rather than the oxidation of the graphene like chemically synthesized GO.

6.7 Exfoliation mechanism

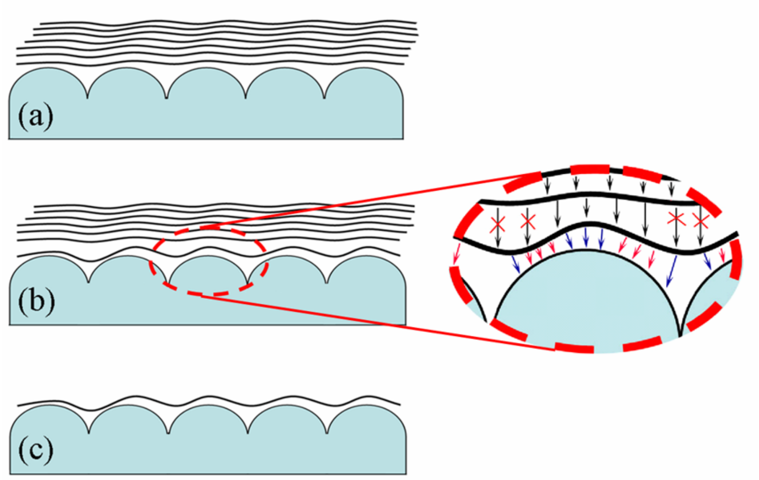

Figure 6.5 Schematic illustration of extrinsic corrugation assisted exfoliation of monolayer graphene on SiO_2 substrate: (a) A graphite flake is deposited on the silicon substrate; (b) The graphene-SiO_2 adhesion energy is enhanced by the thermal treatment; (c) Monolayer graphene is left on the silicon substrate after removal of the top graphite flake with scotch tape.

On the basis of the above results, a model as illustrated in Figure 6.5 is proposed to explain the successful exfoliation of monolayer graphene by the ECAME process. A graphite flake is firstly pressed on a pre-cleaned silicon wafer with a 300 nm thick SiO_2 layer, which has a long range corrugation with a correlation length of about 25 nm (Figure 6.5a).[27] Upon thermal treatment, the morphology of underlayer graphene sheet tends to adapt to and take the shape of the rippled SiO_2 surface (Figure 3b), resulting in improved adhesion between bottom graphene layer and silicon substrate. In this way, the extrinsic corrugation of graphene is established on the surface, leading to the decrease of van der Waals interactions with the top graphene layers. Thereby, the resulting boundary between underlayer graphene and top layers can serve as an exfoliating site, giving birth to the deposition of mostly monolayer graphene on the substrate through the ECAME process (Figure 6.5c).

6.8 FET properties of the exfoliated graphene

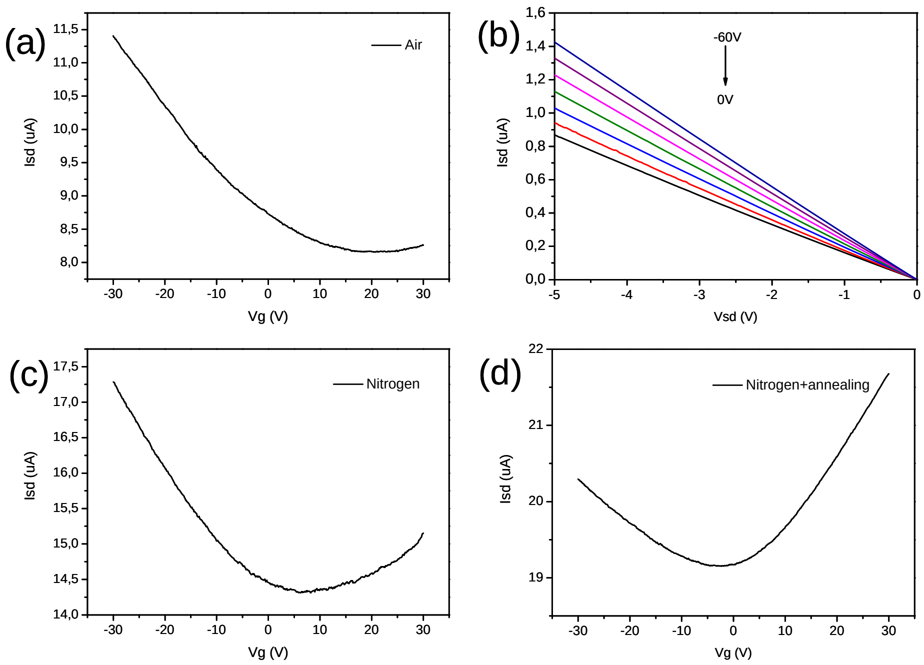

Figure 6.10 (a, c, d) Gate voltage dependence of the I_{sd} measured at V_{ds} = 5 V. (b) I_{ds} (source-drain current) vs V_{sd} (source-drain voltage) curves under different gate voltages (V_g). (a and b are measured in air, c is measure in nitrogen filled glove box, and d is measured in the glove box after annealing the device at 300 ^{o}C for 30 min in nitrogen. The channel length between source and drain is 25 μm.

Typical transport properties of the ultra-large graphene sheet on a silicon substrate are shown in Figure 6.10. The FETs were fabricated in a top-contact configuration with 80 nm thick Au serving as the source and drain electrodes. The transfer and output curves of the graphene sheet prepared by the ECAME process are shown in Figure 6.10(a) and (b), respectively. The graphene film exhibits obvious p-type behavior with the Dirac point around $V_g = +20$ V because of the doping from O_2 and H_2O in air. After transfer of the FETs into a nitrogen filled glove box, the Dirac point shifts to +5 V and shows a typical ambipolar performance as presented in Figure 6.10(c). To further remove the absorbed O_2 and H_2O from the graphene surface, thermal annealing was carried out at 300 ^{o}C for 30 min in the glove box and then the FET performance was measured at room temperature. The transfer curve (Figure 6.10d) displays a perfect ambipolar behavior with the Dirac point around $V_g = 0$ V.

6.9 Conclusion

In summary, we have presented an efficient approach to fabricate ultra-large and patterned monolayer graphene on silicon substrates via an ECAME process. It is proposed that the underlayer graphene is apt to follow the morphology of the silicon substrate when a thick graphite flake is pressed on the silicon wafer and annealed at an elevated temperature. After a reversely mechanical exfoliation, monolayer graphene was successfully deposited on the silicon substrate. In this regard, patterned graphene with varied structures was also fabricated on the silicon substrate from a pre-patterned graphite stamp. AFM and Raman spectroscopy results indicate that most of these transfer-printed sheets and patterns have a thickness of 0.6-0.7 nm. This exfoliation method, without any contaminations, not only offers an ideal alternative for the scalable deposition of monolayer graphene on silicon substrates but also provides a promising route for the construction of graphene based integrated circuits.

References

[1] K. S. Novoselov, A. K. Geim, S. V. Morozov, D. Jiang, Y. Zhang, S. V. Dubonos, I. V. Grigorieva, A. A. Firsov, *Science* **2004**, *306*, 666.

[2] K. S. Novoselov, Z. Jiang, Y. Zhang, S. V. Morozov, H. L. Stormer, U. Zeitler, J. C. Maan, G. S. Boebinger, P. Kim, A. K. Geim, *Science* **2007**, *315*, 1379.

[3] S. Stankovich, D. A. Dikin, G. H. B. Dommett, K. M. Kohlhaas, E. J. Zimney, E. A. Stach, R. D. Piner, S. T. Nguyen, R. S. Ruoff, *Nature* **2006**, *442*, 282.

[4] Y. Hernandez, V. Nicolosi, M. Lotya, F. M. Blighe, Z. Y. Sun, S. De, I. T. McGovern, B. Holland, M. Byrne, Y. K. Gun'ko, J. J. Boland, P. Niraj, G. Duesberg, S. Krishnamurthy, R. Goodhue, J. Hutchison, V. Scardaci, A. C. Ferrari, J. N. Coleman, *Nat. Nanotechnol.* **2008**, *3*, 563.

[5] J. M. Englert, J. Rohrl, C. D. Schmidt, R. Graupner, M. Hundhausen, F. Hauke, A. Hirsch, *Adv. Mater.* **2009**, *21*, 4265.

[6] Z. H. Ni, W. Chen, X. F. Fan, J. L. Kuo, T. Yu, A. T. S. Wee, Z. X. Shen, *Physical Review B* **2008**, *77*.

[7] F. Varchon, R. Feng, J. Hass, X. Li, B. N. Nguyen, C. Naud, P. Mallet, J. Y. Veuillen, C. Berger, E. H. Conrad, L. Magaud, *Phys. Rev. Lett.* **2007**, *99*.

[8] Q. Su, S. P. Pang, V. Alijani, C. Li, X. L. Feng, K. Mullen, *Adv. Mater.* **2009**, *21*, 3191.

[9] C. Gomez-Navarro, J. C. Meyer, R. S. Sundaram, A. Chuvilin, S. Kurasch, M. Burghard, K. Kern, U. Kaiser, *Nano Lett.* **2010**, *10*, 1144.

[10] J. M. Mativetsky, E. Treossi, E. Orgiu, M. Melucci, G. P. Veronese, P. Samorı, V. Palermo, *J. Am. Chem. Soc.* **2010**, *(published on line)*.

[11] A. N. Obraztsov, E. A. Obraztsova, A. V. Tyurnina, A. A. Zolotukhin, *Carbon* **2007**, *45*, 2017.

[12]K. S. Kim, Y. Zhao, H. Jang, S. Y. Lee, J. M. Kim, K. S. Kim, J. H. Ahn, P. Kim, J. Y. Choi, B. H. Hong, *Nature* **2009**, *457*, 706.

[13]X. S. Li, W. W. Cai, J. H. An, S. Kim, J. Nah, D. X. Yang, R. Piner, A. Velamakanni, I. Jung, E. Tutuc, S. K. Banerjee, L. Colombo, R. S. Ruoff, *Science* **2009**, *324*, 1312.

[14]Y. Y. Liang, J. Frisch, L. J. Zhi, H. Norouzi-Arasi, X. L. Feng, J. P. Rabe, N. Koch, K. Mullen, *Nanotechnology* **2009**, *20*.

[15]V. C. Tung, M. J. Allen, Y. Yang, R. B. Kaner, *Nat. Nanotechnol.* **2009**, *4*, 25.

[16]Z. T. Luo, Y. Lu, L. A. Somers, A. T. C. Johnson, *J. Am. Chem. Soc.* **2009**, *131*, 898.

[17]X. F. Zhou, Z. P. Liu, *Chem. Commun.* **2010**, *46*, 2611.

[18]X. Liang, A. S. P. Chang, Y. Zhang, B. D. Harteneck, H. Choo, D. L. Olynick, S. Cabrini, *Nano Lett.* **2009**, *9*, 467.

[19]D. S. Li, W. Windl, N. P. Padture, *Adv. Mater.* **2009**, *21*, 1243.

[20]C. A. Di, D. C. Wei, G. Yu, Y. Q. Liu, Y. L. Guo, D. B. Zhu, *Adv. Mater.* **2008**, *20*, 3289.

[21]S. P. Pang, H. N. Tsao, X. L. Feng, K. Mullen, *Adv. Mater.* **2009**, *21*, 3488.

[22]M. P. Levendorf, C. S. Ruiz-Vargas, S. Garg, J. Park, *Nano Lett.* **2009**, *9*, 4479.

[23]V. Huc, N. Bendiab, N. Rosman, T. Ebbesen, C. Delacour, V. Bouchiat, *Nanotechnology* **2008**, *19*.

[24]L. H. Liu, M. D. Yan, *Nano Lett.* **2009**, *9*, 3375.

[25]A. N. Sidorov, M. M. Yazdanpanah, R. Jalilian, P. J. Ouseph, R. W. Cohn, G. U. Sumanasekera, *Nanotechnology* **2007**, *18*.

[26]Y. B. Zhang, J. P. Small, W. V. Pontius, P. Kim, *Appl. Phys. Lett.* **2005**, *86*.

[27]M. Z. Hossain, *Appl. Phys. Lett.* **2009**, *95*.

[28]M. Ishigami, J. H. Chen, W. G. Cullen, M. S. Fuhrer, E. D. Williams, *Nano Lett.* **2007**, *7*, 1643.

[29]V. Geringer, M. Liebmann, T. Echtermeyer, S. Runte, M. Schmidt, R. Ruckamp, M. C. Lemme, M. Morgenstern, *Phys. Rev. Lett.* **2009**, *102*.

[30]J. C. Meyer, A. K. Geim, M. I. Katsnelson, K. S. Novoselov, T. J. Booth, S. Roth,

Nature **2007**, *446*, 60.

[31] L. Song, L. J. Ci, W. Gao, P. M. Ajayan, *ACS Nano* **2009**, *3*, 1353.

Chapter 7

Conclusion and Outlook

In conclusion, to study the suitability of graphene electrodes in organic electronics, graphene films and patterns were firstly fabricated from GO precursors. Because the requirements of the sheet resistance, transmittance, work function and compatibility with organic semiconductor are varied in different applications, three different types of organic electronics, such as solar cell, FET and photodetector have been employed to evaluate the advantages graphene electrodes compared to commercial ones. As a result, in organic solar cells, there are still some obstacles which we still need to overcome, while in OFETs and photodetectors, graphene electrodes have already shown their enormous potential.

As the transparent electrode in solar cells, very low sheet resistance is required to reduce the energy loss during operation and finally to attain a high power conversion efficiency. For this purpose, the researches for graphene based solar cells have been carried out in two directions: one is to improve the conductivity of the graphene electrodes and the other one is to modify the device construction. As a result, the conductivity of the graphene electrodes has reached nearly 1300 S/cm via a two-step reduction and use of large graphene oxide sheets as precursors. The sheet resistance of a 7 nm thick RGO film is ~ 1.1 kOhm/squsre with the transmittance of

55 % at 500 nm. An efficiency of ~ 0.4 % has been achieved when using such a film as the transparent electrode in graphene/P3HT:PCBM/Al solar cells. After introducing buffer layers PEDOT:PSS and ZnO to the P3HT:PCBM solar cells, an efficiency of ~ 1.0 % has been obtained. However, such efficiency is still much lower than the ITO based solar cells. To further reduce the sheet resistance, a new concept of graphene/metal grid hybrid electrodes has been proposed, which enables one to obtain a low resistance similar to that of ITO electrode. Such hybrid transparent electrodes, with graphene as the short-range conductor and metal grids as the long-range conductor, result in an efficiency of 2.5 %, which is comparable to that of ITO based solar cells. To extend the application of graphene electrodes in flexible electronics, three film fabrication methods, including Langmuir-Blodgett assembly, layer-by-layer deposition and filtering have been subsequently investigated. Based on high-quality electrochemically exfoliated graphene precursors, flexible graphene/metal grid hybrid electrodes have also been successfully fabricated, which provide a sheet resistance of < 200 Ohm/square with a transmittance of 70 % (500 nm), which are very promising for applications in future flexible organic electronics.

The contact property between the electrodes and semiconductors is one of the most important parameters for organic devices. To study the compatibility of graphene electrode with organic semiconductors, graphene electrodes based OFETs and photodetectors have been investigated. As source/drain electrodes in OFETs, graphene patterns have been successfully fabricated by an oxygen plasma etching with the protection of a defined aluminum layer. The sheet resistance of a 60 nm thick RGO film is ~ 200 Ohm/square, which is low enough for serving as source/drain electrodes in OFETs. The patterned graphene source/drain electrodes have been applied in both p-type and n-type OFETs, exhibiting promising performance. Typically, solution processed p-type P3HT FET employing graphene source and drain electrodes afford a hole mobility of 0.04 $cm^2\ V^{-1}s^{-1}$, which is once higher than that of the gold contact devices. For the p-type pentacene and n-type semiconductor $C_{40}H_{40}Br_2N_2O_4$, the threshold voltage has been reduced from -20 V to -8 V and from +12 V to +4V, respectively. The improved performance is possibly due to the relatively low contact resistance between the graphene electrodes and the organic materials.

Another application of patterned graphene electrodes is in photodetectors. To construct highly photosensitive organic photodetectors, coplanar asymmetrical electrodes have been designed and fabricated with graphene as the hole injecting electrode and titanium as the electron injecting electrode. The gap between graphene and titanium can be easily tuned via controlling the oxygen plasma etching time. The P3HT photodetector based on such asymmetrical electrodes has resulted in an improved performance compared with the devices based on the symmetrical gold contacts, including improved photosensitivity, high on/off ratio and low energy consumption. Therefore, together with the feasibility of large scale fabrication of the asymmertical electrodes, this work has opened up another pathway towards the highly photosensitive organic optoelectronics.

Finally, to simplify the deposition process of graphene sheets or patterns on silicon substrates, an extrinsic corrugation assisted mechanical exfoliation method has been developed to directly deposit monolayer graphene from a graphite sheet. It was found that a heat treatment of the graphite flakes on the silicon substrates can make the underlayer graphene adapt to and take the shape of the rippled SiO_2 surface. When a reverse mechanical exfoliation is performed, the exfoliation prefer to occur between the underlayer graphene and the top n-1 layers graphite flake, resulting in the high yield of monolayer graphene left on the substrate. In this case, patterned graphene structures are also deposited on silicon substrate from a pre-patterned HOPG stamp. This exfoliation method, without any contamination, offers an ideal alternative approach for the scalable deposition of monolayer graphene patterns for graphene based electronics.

All of the above topics have been centered on the fabrication of highly conductive graphene films or patterns and their applications in organic electronics. The findings in this thesis would contribute to a deeper insight into the graphene based devices.

Nevertheless, there remains a long way for graphene to go into practical applications. For the graphene/metal grid hybrid electrodes, one of the promising approaches is to establish high-conductive cost-efficient graphene films from graphene inks by solution processing associated with the deposition of random silver nanowires to compose hybrid electrodes. In this case, high temperature reduction and photolithography can be avoided. This strategy is feasible because high quality graphene ink prepared from the electrochemical exfoliation already shows promise in replacing the thermally reduced GO which is limited by high temperature process. One possible obstacle of this work would be how to perfectly mix graphene ink and silver nanowires together to make homogenous films. Thus, film preparation methods such as Langmuir-Blodgett, layer-by-layer, filtering or other methods need to be investigated in the future.

For graphene electrode based organic electronics, the work function of graphene films or patterned graphene electrodes can be modified by surface treatment, which may further improve their performance. It has been revealed that the oxygen containing groups[1] and electron-withdraw dopants (such as HNO_3, $AuCl_3$) can increase the work function of graphene,[2, 3] which is beneficial to collect holes from organic semiconductor materials. On the contrary, ammonia or polyvinyl alcohol can produce n-doped graphene with an enhanced function of collecting electrons.[4, 5] Thus, the electronic properties of the graphene films can be tailored according to the requirement of the different devices. As anode material in P3HT:PCBM heterojunction solar cell, the work function of graphene (~ 4.5 eV) should be further increased to enhance the ability of collecting holes and blocking electrons. Additionally, graphene film can also serve as the cathode via decreasing its work function. Taking OFETs as an example, the performance of the graphene electrodes based devices can be further improved by tuning the work function of graphene electrode to close to the HOMO of p-type semiconductors or LUMO of n-type semiconductors.

Last but not least, low cost synthesis and fabrication methods are also very important in view of the commercial applications. Both the optimization of the traditional methods and the discovery of the new methods for preparing cost-efficient homogenous graphene films or patterns are still urgently required.

References

[1] S. S. Li, K. H. Tu, C. C. Lin, C. W. Chen, M. Chhowalla, *ACS Nano* **2010**, *4*, 3169.

[2] K. S. Kim, Y. Zhao, H. Jang, S. Y. Lee, J. M. Kim, K. S. Kim, J. H. Ahn, P. Kim, J. Y. Choi, B. H. Hong, *Nature* **2009**, *457*, 706.

[3] Y. M. Shi, K. K. Kim, A. Reina, M. Hofmann, L. J. Li, J. Kong, *ACS Nano* **2010**, *4*, 2689.

[4] J. Lu, J. X. Yang, J. Z. Wang, A. L. Lim, S. Wang, K. P. Loh, *ACS Nano* **2009**, *3*, 2367.

[5] P. Blake, P. D. Brimicombe, R. R. Nair, T. J. Booth, D. Jiang, F. Schedin, L. A. Ponomarenko, S. V. Morozov, H. F. Gleeson, E. W. Hill, A. K. Geim, K. S. Novoselov, *Nano Lett.* **2008**, *8*, 1704.

Publication List

[1] Pang, S.P., Hernandez, Y., Feng, X.L., & Müllen, K., Graphene as Transparent Electrode Material for Organic Electronics, Adv Mater. 2011, 23: 2779

[2] Pang, S.P., Englert, J. M., Tsao, H. N., Hernandez, Y., Hirsch, A., Feng, X. and Müllen, K. Extrinsic Corrugation-Assisted Mechanical Exfoliation of Monolayer Graphene. Adv Mater. 2010, 22: 5374.

[3] Pang, S.P., Tsao, H.N., Feng, X.L., & Müllen, K., Patterned Graphene Electrodes from Solution-Processed Graphite Oxide Films for Organic Field-Effect Transistors. Adv Mater. 2009, 21: 3488.

[4] Su, Q., Pang,S.P., Alijani, V., Li, C., Feng, X. L. & Müllen K., Composites of Graphene with Large Aromatic Molecules. Adv. Mater. 2009, 21: 3191.

[5] Li, H., Pang, S., Feng, X., Müllen, K., & Bubeck, C., Polyoxometalate assisted photoreduction of graphene oxide and its nanocomposite formation. Chem. Commun. 2010, 46: 6243.

[6] Li, H., Pang, S., Wu, S., Feng, X., Müllen, K., & Bubeck, C., Layer-by-Layer Assembly and UV Photoreduction of Graphene–Polyoxometalate Composite Films for Electronics. J. Am. Chem. Soc. 2011, 133: 9423

[7] Yang, S.B., Cui, G.L., Pang, S.P., Cao, Q., Kolb, U., Feng, X.L., Maier, J., & Müllen K., Fabrication of Cobalt and Cobalt Oxide/Graphene Composites: Towards High-Performance Anode Materials for Lithium Ion Batteries. Chemsuschem 2010, 3: 236.